

7N-02  
194170  
R 87

# TECHNICAL NOTE

D-15

EXPERIMENTAL INVESTIGATION AT TRANSONIC SPEEDS OF PRESSURE  
DISTRIBUTIONS OVER WEDGE AND CIRCULAR-ARC AIRFOIL  
SECTIONS AND EVALUATION OF PERFORATED-WALL  
INTERFERENCE

By Earl D. Knechtel

Ames Research Center  
Moffett Field, Calif.

NATIONAL AERONAUTICS AND SPACE ADMINISTRATION  
WASHINGTON

August 1959

(NASA-TN-D-15) EXPERIMENTAL INVESTIGATION  
AT TRANSONIC SPEEDS OF PRESSURE  
DISTRIBUTIONS OVER WEDGE AND CIRCULAR-ARC  
AIRFOIL SECTIONS AND EVALUATION OF  
PERFORATED-WALL (NASA. Ames Research

N89-70659

Unclas

00/02 0194170

NATIONAL AERONAUTICS AND SPACE ADMINISTRATION

TECHNICAL NOTE D-15

EXPERIMENTAL INVESTIGATION AT TRANSONIC SPEEDS OF PRESSURE

DISTRIBUTIONS OVER WEDGE AND CIRCULAR-ARC AIRFOIL

SECTIONS AND EVALUATION OF PERFORATED-WALL

INTERFERENCE

By Earl D. Knechtel

SUMMARY

An investigation has been conducted in a two-dimensional perforated wind tunnel to determine the transonic pressure distributions over several symmetrical airfoils having simple wedge and circular-arc sections. The results were employed to show comparisons with theory and to evaluate wall-interference effects. The airfoils included three single wedges of  $9^\circ$  included angle and of various sizes with straight afterbodies, a single wedge without afterbody, a symmetrical double wedge of  $9^\circ$  included angle, and a circular-arc airfoil 6 percent thick. Mach number was varied between 0.7 and the maximum as limited by tunnel power (1.09 for the smallest model) and Reynolds number per foot was approximately constant at 3.9 million.

For the three sizes of single wedges with straight afterbodies, experimental pressure distribution and drag at zero lift indicated small systematic effects of model size.

Additional indications of wall interference were obtained by comparisons of experimental zero-lift pressure distributions and drag results with the corresponding results given by available theories for the single-wedge, double-wedge, and circular-arc airfoils. The slight but systematic differences between the experimental and theoretical pressure distributions indicated the existence of an open-jet type of wall interference throughout the Mach number range from 0.7 to 1.09. This result is in qualitative agreement with recent porous-wall-interference theories. For example, models having a thickness-to-tunnel-height ratio of about 1 percent appeared to experience sonic conditions at an indicated Mach number of approximately 1.03. There were also indications of a wall-induced positive pressure gradient along the model chord near sonic speed.

Good agreement with sonic theory was obtained for a circular-arc airfoil under choked flow conditions with solid test-section walls, when the data were computed for sonic speed. This tends to verify theoretical results showing that choked flow closely resembles sonic free-air flow.

Experimental pressure distributions and pressure drag at zero angle of attack indicated only slight effects attributable to the presence of a straight afterbody behind a single wedge at Mach numbers above 0.82. At lower Mach numbers the presence of the afterbody generally caused increased pressures on the wedge, particularly at points immediately ahead of the shoulder. The increased pressures caused the pressure foredrag to become approximately zero, whereas the pressure foredrag of the wedge alone had been significantly negative at Mach numbers below 0.82.

At angle of attack, viscous effects were evident in the form of negative aerodynamic loadings over the rear portions of the double-wedge and circular-arc airfoils at subsonic speeds. Distributed roughness near the leading edge of the circular-arc model greatly reduced the extent of negative loadings, more than doubled the initial lift-curve slope at Mach numbers up to 0.93, and eliminated most of the extreme forward center-of-pressure travel which had occurred near 0.92 Mach number for the circular-arc model without roughness. The pressure-drag comparisons between experiment and theory for the circular-arc airfoil indicated a progressive drag reduction with increasing boundary-layer thickness at supercritical speeds. This effect was attributable to the propagation forward through the boundary layer of the high pressure behind the shock.

## INTRODUCTION

The difficulties inherent in the study of transonic aerodynamics, both theoretical and experimental, are well known. In recent years, however, the development of the ventilated test section for wind tunnels has made experimental investigations in the transonic range increasingly straightforward and reliable, while significant advances have also been made in solving approximately the basically nonlinear equations of transonic flow. The first two-dimensional transonic solutions were restricted to flows about simple wedges (refs. 1 through 5), but recent methods have extended the transonic solutions to somewhat more general classes of airfoils (refs. 6, 7, and 8).

A number of reports have been published (e.g., refs. 9 to 11) in which experimental data for simple airfoils have been compared with results of transonic theory. The present investigation was undertaken to provide additional experimental results at high subsonic and transonic speeds for several wedge-shaped and circular-arc profiles for which theoretical results are available. In addition to providing a comparison with theory, the present experimental data were intended to be of general interest in showing airfoil characteristics at transonic speeds and possible effects of wall interference in two-dimensional perforated-wall wind tunnels.

## NOTATION

|                    |  |
|--------------------|--|
| $a_0$              | section lift-curve slope, per deg, $\frac{dc_l}{d\alpha_0}$                          |
| $C_p$              | local pressure coefficient, $\frac{p-p_\infty}{q_\infty}$                            |
| $\Delta C_p$       | loading increment, $C_{p_{lower}} - C_{p_{upper}}$                                   |
| $\bar{C}_p$        | reduced pressure coefficient, $\frac{[M_\infty^2(\gamma+1)]^{1/3}}{(t/c)^{2/3}} C_p$ |
| $\bar{C}_{p_{cr}}$ | critical reduced pressure coefficient  |
| $c$                | model chord  |
| c.p.               | center-of-pressure location, chord lengths behind leading edge                       |
| $c_{d_p}$          | section pressure-drag coefficient  |
| $\bar{c}_{d_p}$    | reduced drag coefficient, $\frac{[M_\infty^2(\gamma+1)]^{1/3}}{(t/c)^{5/3}} c_{d_p}$ |
| $c_l$              | section lift coefficient   |
| $c_{m_{0.5}}$      | section pitching-moment coefficient about midchord                                   |
| $h$                | height of wind-tunnel test section   |
| $M$                | local Mach number  |
| $M_\infty$         | tunnel Mach number   |
| $p$                | local static pressure  |
| $p_\infty$         | free-stream static pressure  |
| $q_\infty$         | free-stream dynamic pressure   |
| $R$                | Reynolds number  |
| $t$                | maximum airfoil thickness  |
| $x$                | airfoil abscissa (from leading edge)   |
| $x^*$              | airfoil abscissa at sonic point  |

y airfoil ordinate

y\* airfoil ordinate at sonic point

$\alpha_0$  section angle of attack, deg

$\gamma$  ratio of specific heats, 1.4 for air

$\xi_\infty$  reduced Mach number,  $\frac{M_\infty^2 - 1}{[M_\infty^2(\gamma+1)(t/c)]^{2/3}}$

## APPARATUS AND MODELS

### Wind Tunnel

The investigation was conducted in the Ames 1- by 3-1/2-foot, two-dimensional-flow wind tunnel. The test section of this facility, which basically had solid walls, was adapted for operation at Mach numbers up to 1.1 by the insertion of perforated upper and lower walls. As illustrated in figure 1(a), shallow plenum chambers were created by the gap between the perforated walls and the original solid walls, resulting in a reduction of tunnel height from 42 to 35 inches.

Each perforated wall (fig. 1(b)) was made up of two thicknesses of metal plate, line-drilled in a pattern of equally spaced holes 0.266 inch in diameter. By sliding the adjustment plate within the plenum chamber forward, as shown in figure 1, the porosity was changed in such a way that air flowing through the perforated wall into the plenum chamber must turn through at least a right angle. The wall porosity could be adjusted between the limits of 2- and 10-percent open-area ratio.

The solid wooden inlet fairings ahead of the perforated section were sealed to the walls to prevent leakage of upstream air into the plenum chambers, which were vented at the downstream end by means of an adjustable diffuser step. Angular divergence of the perforated top and bottom walls could be varied in order to obtain better tunnel performance within the power limitations of the two 1000-horsepower tunnel drive motors.

Possible condensation effects due to air exchange at atmospheric conditions were minimized by operation at stagnation temperatures as high as 180° F.

## Models

The airfoil models employed in this investigation were of three simple types - single-wedge, double-wedge, and circular-arc profiles. All were pressure-distribution models which spanned the 1-foot width of the tunnel, passed completely through one or both walls, and were supported by contoured clamps or by a combination of clamps and steel pins. Air leakage around clamps and at pinned ends of the models was prevented by rubber seals.

Details of airfoil sections and orifice locations for the models are presented in figure 2. The 2-1/2-, 4-, and 8-inch wedges of  $9^\circ$  included angle are shown attached to the straight afterbody with which each was tested. The 4-inch wedge was also tested without the afterbody.

The 5-inch double wedge was identical in section to the model employed in reference 11 and, similarly, had orifices on only one surface. As discussed in detail in reference 11, this required two sets of runs to provide pressure distributions corresponding to upper and lower surfaces.

## TESTS AND DATA REDUCTION

### Tunnel Calibration Tests

Initial measurements of pressures along the perforated walls indicated that increased wall-divergence angles permitted attainment of higher Mach numbers, but simultaneously increased the axial pressure gradient in the test section. A divergence angle of  $0.6^\circ$  for each wall was considered a satisfactory compromise and was employed for all of the present perforated-wall results. Preliminary tests showed no large effects of wall porosity or diffuser step setting within the available ranges of variation, so a porosity of 5 percent and a step of 0.44 inch were employed for the present investigation. The Mach number distributions measured along the axis of the empty test section under these conditions are shown in figure 3 for Mach numbers ranging from 0.7 to 1.1.

The plenum-chamber pressure, which is commonly utilized as a reference pressure for transonic wind tunnels, was found to be unsatisfactory for this purpose in the present case under lifting conditions. This effect was attributed to insufficient plenum-chamber volume. Instead, the Mach number at the model position was calibrated with reference to the pressure measured at an orifice on the side-wall center line within the perforated test section and 26 inches upstream of the quarter-chord location of the models.

## Airfoil Tests

The actual testing procedure consisted of setting the model to the desired angle of attack, then operating the wind tunnel at successive Mach numbers through the available range while recording photographically the pressure distributions indicated on a multiple-tube mercury-in-glass manometer.

Pressure distributions were measured for each of the models at Mach numbers ranging from 0.7 to the maximum allowed by the power limitations of the tunnel for each model size and angle of attack. For the smaller models, the maximum Mach number was as high as 1.09. For this range of Mach numbers, and because the wind tunnel operates at atmospheric total pressure, the test Reynolds number per foot was approximately constant at 3.9 million.

The single wedges were tested only at zero angle of attack, whereas the double-wedge and circular-arc models were tested at several angles of attack from  $0^\circ$  to  $4^\circ$ . Tests were also conducted on the circular-arc model to determine the effects of adding, between the 2-percent and 4-percent-chord stations, a spanwise strip of distributed roughness consisting of Carborundum grit of approximately 0.004-inch mean diameter, which, according to reference 12, would assure transition to a turbulent boundary layer.

An additional test was conducted to determine the zero-lift pressure distribution of the circular-arc airfoil in a choked solid-wall test section. For this purpose, the perforated walls were sealed with tape, the wall-divergence angle was reduced to zero, and the wind tunnel was operated at maximum power to assure choking of the flow at the model location.

## Data Reduction

The static pressures measured on the models were reduced to the usual pressure coefficient form,

$$C_p = \frac{p - p_\infty}{q_\infty}$$

In this procedure, the test-section static and dynamic pressures,  $p_\infty$  and  $q_\infty$ , were obtained by correcting the corresponding quantities measured at the reference orifice for the difference in conditions between the reference orifice and the model quarter-chord location, as indicated by

the tunnel-empty calibration. The airfoil pressure distributions have not been corrected for the tunnel-empty longitudinal pressure gradient at the model position; however, calculations have shown this effect to be very small.

Faired plots of  $C_p$  vs.  $x/c$  were integrated mechanically to obtain values of normal-force and pitching-moment coefficients, thereby neglecting the minor effect of chord force on pitching moment. Values of pressure chord-force coefficient were obtained similarly from plots of  $C_p$  vs.  $y/c$  for the circular-arc model and by combining the proper components of integrated normal forces on the various faces of the wedge models. The drag results have been corrected for small buoyancy effects of longitudinal pressure gradients in the test section by the method of reference 13.

### Precision

There are several possible random errors which might have affected the precision, or repeatability, of the results presented here. Partly because of the backlash in the angle-of-attack mechanism, all models were subject to some error in setting angles of attack. In addition, as discussed more fully in reference 11, the double-wedge model was subject to possible errors in duplicating runs with the orifices first on the upper surface and then on the lower surface. It has been estimated from the pressure data at zero lift that uncertainties in angle of attack were approximately  $\pm 0.1^\circ$ .

Consideration of the factors involved in the data reduction indicates that the probable random errors were approximately  $\pm 0.005$  in Mach number and  $\pm 0.01$  in pressure coefficient. (For the front two orifices on each surface of the 4-inch wedge without afterbody, pressure lags due to small tubing caused slight errors which were partially random in nature.) Additional uncertainties in fairing and integrating the pressure distributions cause the estimated random errors in force and moment coefficients to be  $c_l = \pm 0.01$ ;  $c_{m_{0.5}} = \pm 0.005$ ; and  $c_{d_p} = \pm 0.001$ .

### RESULTS AND DISCUSSION

The basic airfoil data are presented in figures 4 through 7 as pressure distributions at representative Mach numbers and angles of attack. Slight discrepancies in the pressure distributions of two of the wedge models require explanations. Unduly high pressures over the rearmost part of the smallest wedge (shown as dashed curves in fig. 4(a)) were caused by an imperfectly fitted afterbody, and for this reason data points for the rear orifices have been deleted from subsequent pressure comparisons. The increase in measured drag attributable to these erroneous pressures



has been estimated to be no more than the precision in measuring drag; hence no correction of these drag results has been made. For the two front orifices on each surface of the wedge without afterbody, time lags due to smaller tubing caused the slight differences between upper and lower surfaces shown as dashed curves in figure 4(d). In subsequent pressure comparisons for this model, the average of upper and lower surface pressures was used. The force and moment coefficients derived from the pressure distributions are shown as functions of Mach number in figures 8, 9, and 10, respectively, for the single-wedge, double-wedge, and circular-arc airfoils.

### Effects of Model Size for Single Wedges

Wall-interference effects for perforated test sections have not been as completely defined, either theoretically or experimentally, as those for the more conventional solid-wall test sections. Since this is particularly true for two-dimensional perforated wind tunnels, an attempt was made to determine experimentally the possible effects of varying model size relative to tunnel height. The wind tunnel employed in the present investigation operates at atmospheric total pressure, so variations in model size caused proportional changes in Reynolds number. Accordingly, the airfoil chosen for the wall-interference study was a single wedge, for which the favorable pressure gradients throughout the transonic speed range might be expected to minimize any resulting viscous effects. Three such models having  $9^\circ$  included wedge angles and thickness-to-tunnel-height ratios from 0.011 to 0.036 were tested with a straight afterbody, for zero angle of attack through the Mach number range available in each case. The interference study was thus restricted to the effects of axial velocity perturbation, or blockage interference. (In a later section, the apparent Mach number shift induced by the walls has been assessed by comparisons between experimental and theoretical results for single-wedge, double-wedge, and circular-arc airfoils at zero angle of attack.)

The effects of model size on the measured pressures could be of interest in terms of either pressure variations with Mach number for given airfoil stations or chordwise pressure distributions at fixed Mach numbers. For this reason, pressure coefficients for the three wedge models of varying size are shown superposed in figure 11 as variations with Mach number for six chordwise stations and in figure 12 as chordwise distributions at Mach numbers 0.70, 0.88, and 1.00. In these two figures (aside from the previously mentioned high pressures over the rear part of the smallest wedge caused by model imperfections) the systematic effects of model size on pressure coefficient were generally no larger than the estimated precision of the pressure data.

Any systematic effects of model size might logically be reflected in the drag results. In figure 8 are presented the variations with Mach number of pressure foredrag coefficients measured at  $\alpha_0 = 0^\circ$  for

three sizes of single wedge with straight afterbody. Small but systematic increases in pressure drag with increasing model size are discernible which, although only of the order of precision of the drag data, might be attributed to perforated-wall interference.

### Effects of Afterbody on Single Wedge

The configuration which has most frequently been studied, both theoretically and experimentally, is the single-wedge airfoil with a straight afterbody. The advantage of this configuration for theoretical investigations lies in fixing a simple boundary condition in the hodograph plane in which the solution is usually obtained. Within the framework of inviscid theory, the corner of the wedge is a fixed sonic point and the beginning of a supersonic region, so the detailed shape of the afterbody can be shown to have negligible influence on the pressures over the front wedge at and above  $M_\infty = 1$ . This assumption permits the use of theoretical sonic and supersonic solutions for the front wedge somewhat independently of the afterbody shape assumed for the theory.

In order to demonstrate the effect of an afterbody on the pressure distribution and drag of a single wedge, the intermediate-sized single-wedge model was tested with and without the straight afterbody. In figure 13 are shown directly the effects of the afterbody on pressure distributions (averaged for upper and lower surfaces) at  $\alpha_0 = 0^\circ$  and at three interpolated Mach numbers. These results indicate that the effect of the afterbody was largely confined to the lower Mach number range and to the more rearward part of the airfoil, as typified by the comparison at  $M_\infty = 0.7$ . At  $M_\infty = 0.88$  and 1.00, the experimental pressure distributions showed very little effect of the afterbody, thus tending to support the theoretical assumption that, near sonic speed, pressures over the front wedge are influenced negligibly by the afterbody geometry. The corresponding effects on pressure foredrag are shown in figure 14, where the presence of the afterbody is seen to have caused significant increases in  $c_{dp}$  at Mach numbers below approximately 0.82 and slight increases at higher Mach numbers.

### Effects of Roughness

In contrast to the results for the single-wedge airfoils, which were chosen to minimize the effects of viscosity, the results for the double-wedge and circular-arc airfoils might be expected to show viscous effects. The basic pressure distributions in figures 5 and 6 for the double-wedge and circular-arc airfoils, respectively, show that under lifting conditions at high subsonic speeds, there existed regions of negative loading over the rear parts of both airfoils which were believed to result from laminar boundary-layer separation in the presence of an adverse pressure gradient.

In order to determine the effects of altering the boundary-layer condition, the circular-arc airfoil was also tested with a roughness element near the leading edge of a type known to induce turbulent flow over airfoils under these conditions.

Comparison of corresponding subsonic pressure distributions with and without roughness (e.g., figs. 6(b) and 7(b)) indicates that addition of roughness caused the negative loadings on the circular-arc model to be reduced in severity, or even eliminated. In figure 15, the effects of roughness on lift are shown in more detail as chordwise distributions of the loading increment,  $\Delta C_p$ , at  $\alpha_0 = 0.5^\circ$  for three Mach numbers, with and without roughness. At Mach numbers of 0.857 and 0.924, addition of the roughness element not only decreased the negative loadings near the trailing edge, but generally increased the loading increment over the complete airfoil. This effect is characteristic of increased circulation brought about by favorable changes in the boundary-layer flow on both surfaces. At  $M_\infty = 1.026$ , the loading was changed only slightly by the addition of roughness, as would have been suggested for Mach numbers above 0.96 by the basic lift results shown in figure 10(a). In contrast to the generally large effects on lift at subsonic Mach numbers and angles of attack below  $2^\circ$ , the effects of roughness on drag and pitching moment shown in figures 10(b) and 10(c) were relatively small.

Because the largest effects of roughness occurred near zero lift, the initial values of lift-curve slope and center of pressure as affected by roughness are of interest. In figure 16 are shown the variations with Mach number of the lift-curve slope and center of pressure near  $\alpha_0 = 0^\circ$  for the circular-arc airfoil with and without the boundary-layer trip. At Mach numbers up to approximately 0.93, the model without roughness had low values of lift-curve slope and center-of-pressure positions varying from the leading edge to as much as one chord length ahead of the leading edge. At these subsonic speeds, the addition of roughness caused the lift-curve slope to more than double and restricted the center of pressure to variations between 0.05 and 0.35 chord lengths behind the leading edge. For Mach numbers of 0.94 and greater, the effects of roughness were less pronounced.

Qualitatively similar effects of roughness were shown in reference 14 for an unswept wing having a modified-wedge airfoil, and similar effects of roughness on pitching moments were observed in reference 15 for the case of a three-dimensional model having an unswept wing of circular-arc cross section. The corresponding effects on lift in the latter case were not large, presumably because the wing was only half as thick as the 6-percent-thick airfoil of the present investigation.

Under lifting conditions, airfoils with a sharp leading edge usually have a separation bubble near the leading edge of the upper surface and markedly different boundary-layer thicknesses on the upper and lower surfaces. The resulting effective camber would vary with the boundary-layer condition and therefore with roughness. This camber effect may

be a factor in the present results, inasmuch as comparisons between figures 6(b) and 7(b) indicate a greater effect of roughness on the lower surface, where flow separation would be less likely to occur.

The slight decrease in lift-curve slope with Mach number shown in figure 16 at subsonic speeds (rather than the increase suggested by the Prandtl-Glauert rule) appears to be a characteristic of the airfoil section, since a similar variation was shown in reference 16 for a 10-percent-thick circular-arc airfoil at subsonic speeds.

### Comparisons With Theory

In the analysis of the present data, it will be instructive to make comparisons between the experimental results and those obtained by means of suitable theory. In making such comparisons use will be made of transonic similarity parameters (ref. 17), which are helpful in obtaining new solutions as well as in correlating experimental transonic data. The forms of the transonic similarity parameters employed in the present case will be those recommended in reference 18.

Experimental and theoretical work in the transonic range have shown the existence of the so-called Mach number freeze phenomenon for a small range of Mach numbers near unity, or stationary local Mach numbers on the body corresponding to those for sonic free-stream flow. This behavior has led to the following simple relation in transonic small-disturbance theory between the reduced pressure coefficient at Mach numbers near unity and that at sonic speed ( $\xi_\infty = 0$ ):

$$C_p = \bar{C}_p|_{\xi_\infty=0} + 2\xi_\infty$$

For each of the types of airfoil of the present investigation, this relation will be used to show the degree of correlation of the parameter  $\bar{C}_p - 2\xi_\infty$  for experimental results near  $M_\infty = 1$ .

Single-wedge airfoil with afterbody.— Because the tests extended to higher Mach numbers and were less influenced by wall interference for the smallest single wedge ( $t/h = 0.011$ ), the data for that model are employed in similarity form to show correlations among the experimental results at various transonic speeds as well as correlations with theory. In figure 17(a), the experimental distributions of  $\bar{C}_p - 2\xi_\infty$  indicate the freeze effect by correlating within a relatively narrow band for Mach numbers varying from 0.961 to 1.065. This band of experimental values is approximately parallel to, but noticeably smaller in magnitude than, the values shown for the sonic theories of references 1 and 7.

It may be of interest to relate this discrepancy to possible tunnel-wall interference at sonic speed. Experience has shown that the boundary condition at a perforated wall may be simulated by the mathematically simpler boundary condition at a porous wall, and such an assumption is commonly made in analyzing the wall interference of a perforated tunnel (see ref. 19). An unpublished approximation to the axial interference flow caused by a porous, two-dimensional test section at sonic speed has been obtained by W. A. Page of the Ames Research Center. The method was analogous to that given by Berndt in reference 20 for slotted tunnels and by Page in reference 21 for three-dimensional porous-wall tunnels, and employed the asymptotic solution given in reference 22 for the flow at a great distance from a planar model. Certain details of the solution suggest the possibility of an axial gradient in wall-interference effect. In the simplest form, however, the interference of a porous, two-dimensional test section containing a vanishingly small model is given approximately as a uniform increment in axial velocity, given by

$$\Delta M = -0.59 \left( \frac{y^*}{x^*} \right)^{2/15} \left( \frac{2y^*}{h} \right)^{2/5}$$

where  $x^*$  and  $y^*$  are the airfoil coordinates at the sonic point and  $h$  is the tunnel height. For the flow in the test section to simulate an unbounded sonic flow, the indicated tunnel Mach number must be set at a slightly higher value given by

$$M_\infty = 1 - \Delta M$$

The interference is therefore of the same sign as that of a subsonic open-jet test section or that which would be indicated by the subsonic porous-wall interference theory of reference 19 for values of wall permeability in common use.

The sonic wall-interference equation stated above would indicate that an unbounded sonic flow should be simulated for the small single-wedge model at an indicated Mach number of 1.069. It follows that if this value of  $\Delta M$  were correct, experimental results obtained at an indicated Mach number of 1.069, but calculated as if the Mach number were unity, might be expected to agree with reliable sonic theory. As is noted in reference 7, the sonic theory of reference 1 for single wedges is generally regarded as virtually an exact solution of the transonic small-disturbance equations, and hence might be considered a suitable reference against which to compare the experimental results and other theories. In order to evaluate the effect of the indicated  $\Delta M$ , one might first compare in figure 17(b) the reduced pressure distributions given by the two sonic theories and the experimental result for the small wedge model at  $M_\infty = 1.065$ , calculated for sonic speed. This experimental pressure distribution is seen to be approximately parallel to the theoretical curves, but significantly higher, suggesting that the correction should have been somewhat different. As a guide, there is also presented in

figure 17(b) an experimental pressure distribution for an interpolated tunnel Mach number of unity, which is also roughly parallel to the theoretical curves, but somewhat lower. Finally, choosing a Mach number between these two extremes, it was found that the experimental pressure distribution for an indicated Mach number of 1.026, but computed for sonic speed, agreed very well with the theories of references 1 and 7. This suggests that at sonic speeds, the data for the single-wedge model support the concept of a perforated-wall interference, but that the magnitude of this effect is approximately half that given by the formula.

It is also instructive to observe the apparent interference over a range of transonic speeds by comparing experimental and theoretical variations with reduced Mach number of  $\bar{C}_p$  and  $\bar{c}_{dp}$ . The usefulness of similarity parameters for this purpose lies in the fact that, for given measured pressures near sonic speed, the values of  $\bar{C}_p$  and  $\bar{c}_{dp}$  are almost invariant with changes in assumed Mach number of the order of the values shown here. In figure 18, experimental values of  $\bar{C}_p$  at two stations on the small single wedge differed systematically through the transonic range from the corresponding theoretical results given by references 1, 2, 3, and 7, although the slopes at sonic speed ( $\xi_\infty = 0$ ) compared quite well. In each case, the theoretical reduced-pressure coefficient was realized at a tunnel Mach number somewhat higher, indicating that the apparent wall interference had the same sign for Mach numbers slightly above and below sonic speed. This conclusion might also be reached by an intuitive argument similar to that employed in deducing the existence of the Mach number freeze; that is, at a slightly supersonic Mach number  $1 + \epsilon$ , the flow conditions at the model location behind the detached shock wave are essentially equivalent to those at  $M_\infty = 1 - \epsilon$ . Hence, the effect of perforated walls on the measured airfoil characteristics might be considered qualitatively similar at equal increments above and below sonic speed.

The apparent wall interference for the single wedge at near-sonic speeds is also evident in figure 19, in which the experimental variation of reduced drag is compared with the corresponding values given by references 2, 4, and 7.

Double-wedge airfoil.— In figure 20(a) theoretical and experimental zero-lift pressure distributions for the double-wedge airfoil are shown in the similarity form  $\bar{C}_p - 2\xi_\infty$  which, according to the Mach number freeze principle, should be relatively invariant with changes in Mach number near sonic speed. As is evident in the figure, experimental pressure distributions correlated among themselves very well to indicate the freeze effect for test Mach numbers from 0.987 to 1.058, but less well for  $M_\infty = 0.945$ . Here again, as for the single-wedge airfoil, the experimental pressures were systematically displaced from the theoretical values given by references 1 and 7.

The geometry of the double-wedge model back to the sonic point is exactly that of the small single wedge, hence use of the  $\Delta M$  formula again indicates that true sonic speed should correspond to  $M_\infty = 1.069$ . In figure 20(b), the reduced pressure distribution at the highest test Mach number, 1.058, is shown as computed for sonic speed and compared with the sonic theories. Again for comparison the experimental results are presented for an interpolated test Mach number of unity and for a test Mach number of 1.029, computed for sonic conditions. Comparisons are best made with the theory of reference 1, which is known to be slightly more exact than that of reference 7. This is particularly true over the rear wedge, where the difference between the two theoretical results represents the effects of neglecting, in reference 7, disturbances reflecting from the sonic line. The experimental pressure distribution for  $M_\infty = 1.029$ , computed for sonic speed, agreed much better with the theory of reference 1 than did the experimental results for either  $M_\infty = 1.000$  or  $M_\infty = 1.058$  computed for sonic speed. Therefore, as with the single wedge, these results tend to verify the existence at sonic speed of a wall-induced interference having a magnitude somewhat less than that calculated by the formula stated previously.

In figure 21, the chordwise variations at sonic speed of the loading increment per degree angle of attack are shown for the double-wedge model. The experimental loadings at angles of attack of  $1^\circ$  and  $2^\circ$  compare reasonably well with the theoretical values obtained from reference 5.

The experimental drag results at  $\alpha_0 = 0^\circ$  are presented in figure 22 in similarity form and compared with transonic theoretical results. The measured values of  $\bar{c}_{d_p}$  near sonic speed were within about 5 percent of those shown by the transonic theory of reference 3 and, like the theoretical values, were relatively constant over a range of near-sonic speeds.

Circular-arc airfoil.— In a manner similar to that employed for the single-wedge and double-wedge airfoils, the experimental pressure distributions for the circular-arc airfoil have been compared in transonic similarity form with those obtained from available theory. In figure 23(a), test values of  $\bar{C}_p - 2\xi_\infty$  show the freeze effect quite well for three Mach numbers from 0.985 to 1.057, but all were significantly more negative than the theoretical sonic values given in reference 7. The pressure distribution at  $M_\infty = 0.961$ , however, differed markedly near the trailing edge.

Use of the theoretical sonic point of a circular-arc airfoil ( $x^*/c = 0.25$ ) in the sonic interference formula indicates that a true Mach number of unity should occur for this combination of model and test section at  $M_\infty = 1.061$ . The experimental pressure distribution for the nearest test Mach number, 1.057, is shown in figure 23(b) as computed for sonic conditions and compared with the sonic theory. Also shown is the experimental distribution interpolated at a test Mach number of unity. Near the leading edge, the agreement with theory was best for an indicated Mach number of 1.000, whereas over the central and rear

parts of the airfoil, agreement was best for  $M_\infty = 1.057$ . Experimental results for an intermediate Mach number of 1.030, computed for sonic conditions, agreed well with theory near the quarter-chord point of the model, but departed gradually from theory both ahead of and behind that point. The tunnel-empty calibration did not indicate axial Mach number gradients of this magnitude near sonic speed and calculations indicated that airfoil boundary-layer growth could account for no more than 20 percent of the discrepancy in pressure gradient over the model. These results therefore tend to confirm the previously mentioned possibility that perforated-wall interference at sonic speed may induce at the model location a pressure gradient as well as a blockage effect.

In recent years, a number of investigations have been conducted to relate the flow in a closed test section under choked conditions to free-air flow at sonic speed. Theoretical investigation of this problem in reference 23 indicated that choked flow resembles sonic free-air flow very closely. In order to investigate this effect, the circular-arc airfoil was tested at  $\alpha_0 = 0^\circ$  under choked conditions with the perforated walls taped over and the wall divergence reduced to zero. The resulting pressure distribution, computed for sonic speed, is presented in figure 23(c) for comparison with the perforated-wall results interpolated at sonic speed and with the sonic theory of reference 7. Also shown in this figure is the experimental sonic pressure distribution given in reference 10 for a similar profile. Under choked conditions, the pressure distribution over the forward part of the circular arc agreed very well with the theory. Over the more rearward part, however, the choked-flow results fell about midway between the theory and the sonic perforated-wall results. The choked-flow pressure distribution, in fact, agreed slightly better with the sonic theory than did the best perforated-wall data of figure 23(b) (for  $M_\infty = 1.030$ ), and hence might be considered a good approximation to free-air sonic flow.

The data from reference 10 shown in figure 23(c) were obtained on a half-model of a 6-percent-thick circular-arc airfoil mounted on the floor of an ONERA tunnel which had a ventilated upper wall. Over the center part of the model, the ONERA pressure distribution fell between the interpolated sonic- and choked-flow results of the present investigation. Near the leading and trailing edges, however, the pressures deviated more toward a subsonic pattern. As discussed in reference 7, this effect is attributable to the fact that the model was embedded in the wall boundary layer. Poorer agreement with theory might therefore be expected near the leading and trailing edges, where the profile thickness is particularly small in comparison with the wall boundary-layer thickness. In addition, the pressure distribution near the trailing edge at sonic speed can be expected to be influenced by interaction between the trailing-edge shock waves and the thick boundary layer.

In reference 8 an approximate solution has been obtained for the high-subsonic flow over a family of airfoils, among which are those of circular-arc section. These results are shown in figure 23(d) together with the present experimental similarity pressure distributions at six



Mach numbers from 0.723 to 0.896. At the two lowest Mach numbers, the agreement between experiment and theory was very satisfactory. At and above  $M_\infty = 0.833$ , which was the critical Mach number for this airfoil by transonic theory, the difference between experiment and theory became increasingly large. In the supercritical speed range a tendency is evident for experimental reduced pressure distributions to resemble more nearly the theoretical distribution for a lower Mach number, in a manner similar to the effect shown near sonic speed. In order to demonstrate this behavior, two arbitrary cases are shown in figure 23(d) in which experimental reduced pressure distributions have been recomputed as if they had been obtained at the next lower Mach number. For instance, experimental data corrected from  $M_\infty = 0.850$  to 0.833 agreed much better with the theory for the lower Mach number, and similarly for data corrected from  $M_\infty = 0.880$  to 0.850. The remaining marked difference at supercritical speeds results from the discontinuous pressure jump across the shock shown by the theory, compared with the gradual recompression indicated by the experimental data as influenced by the boundary layer at the surface.

An indication of the general tendency to a Mach number shift throughout the transonic speed range may be noted by comparing experimental and theoretical values of reduced pressure coefficient at a given point on the airfoil, as presented in figure 24. It has been noted previously that values of  $\bar{C}_p$  or  $\bar{C}_{d_p}$  are relatively insensitive to small shifts in assumed Mach number. As a result, points being corrected to a different Mach number would be shifted essentially at constant  $\bar{C}_p$ , or horizontally in figure 24. In the present case, for the experiment to duplicate the theoretical values of  $\bar{C}_p$  at the airfoil midpoint, the experimental Mach numbers obviously would require correction to lower values for all transonic speeds at which this airfoil was tested.

Also shown in figure 24 at the sonic condition ( $\xi_\infty = 0$ ) is the corresponding  $\bar{C}_p$  for the model in the choked tunnel. As previously noted in connection with figure 23(c), these results agreed more nearly with the transonic theory than did the sonic data in the perforated tunnel.

The values of  $\bar{C}_p$  at midchord obtained from the experimental results of reference 10 agreed quite well with the theory near sonic speed, but agreement was rather poor at values less than  $\xi_\infty = -0.6$  (or less than  $M_\infty = 0.92$ ). Again, this discrepancy in the data of reference 10 may logically be attributed at least partly to the effects of wall boundary layer. For instance, the critical Mach number given by the transonic theory of reference 7 was 0.833 ( $\xi_\infty = -1.42$ ) for the 6-percent-thick circular-arc airfoil, whereas the corresponding critical Mach number measured in reference 10 was 0.875. This tends to indicate that, at least up to high subsonic speeds, a thick embedding boundary layer causes the flow over a given model to resemble the inviscid flow over a somewhat thinner model. As indicated in figure 24, this effect at midchord

disappeared at Mach numbers above 0.92 ( $\xi_\infty = -0.6$ ), which may be a favorable effect of the increasing region of accelerating flow over the center and rear of the model.

The pressure-drag variations over the transonic Mach number range for the circular-arc airfoil are shown in similarity form in figure 25 for the present results, the experimental results of reference 10, and the theoretical results of references 7 and 8. The present experimental drag in the perforated-wall tunnel showed a smooth rise beginning near the critical speed,  $\xi_\infty = -1.42$ . Near sonic speed, the agreement with the theoretical sonic drag was quite good. At high subsonic speeds, however, the agreement between experimental drag and the approximate nonlinear theory of reference 8 was rather poor. In this region of sharply increasing drag, wall interference is obviously a factor. In fact, the Mach number shift indicated in figure 24 by comparison of experimental and theoretical pressures at midchord explains more than one-half the discrepancy between the theoretical and present experimental drag results shown in figure 25 at high subsonic speeds. The remaining subsonic drag discrepancy is at least partly attributable to the differences in the recompression pattern between theory and experiment that were shown in figure 23(d), inasmuch as the pressure drag of an airfoil symmetrical about the midchord is entirely caused by the amount of pressure asymmetry about the midchord. The effective rounding-off of the recompression pattern over the rear part of the airfoil, by reducing the amount of pressure asymmetry, therefore has a definite tendency to reduce the drag below that of the theory. As was noted for figure 10(b), the drag of the circular-arc model was not appreciably influenced by the addition of roughness to induce a turbulent boundary layer, hence roughness would not have changed this comparison.

Under the influence of the enveloping wall boundary layer with possible shock-wave interactions, the experimental pressure distributions shown for the 6-percent-thick circular-arc airfoil in reference 10 were more symmetrical than those obtained in the present investigation. The resulting drag values were much lower than either the present experimental results or theory, as shown in figure 25. The low drag at subsonic speeds may be interpreted as another indication that the models of reference 10, because of the wall boundary layer, had pressure distributions resembling those of a somewhat thinner airfoil. At sonic and slightly supersonic speeds, the drag data of reference 10 were shown to compare more closely with theory when the experimental pressure distributions were "extrapolated" to eliminate the rounding-off near the trailing edge believed attributable to interaction between the wall boundary layer and the trailing-edge shock wave.

The subsonic drag comparisons of figure 25 thus show a systematic trend of drag reduction with increasing boundary-layer thickness, from the inviscid conditions of the theory to the small boundary-layer thickness of the present tests and the thick wall boundary layer of the tests of reference 10. To some extent, as was previously noted, the drag reduction in the case of the thick wall boundary layer resulted from

shock-wave formation being delayed to a somewhat higher Mach number. In addition, however, it appears entirely plausible that the sharp pressure discontinuity across the shock wave at the rear of the model may diffuse through the boundary layer and generally tend to reduce the pressure drag. As compared with inviscid theory, the drag values of the present tests may have been slightly influenced in this way by the relatively thin boundary layer, whereas the drag results of reference 10 could have been seriously affected by pressure perturbations along the thick boundary layer in those tests. Conversely, decreasing the boundary-layer thickness behind the maximum-thickness point of an airfoil by such means as suction might be expected to increase the pressure drag at supercritical speeds. Additional observations are made in reference 24 regarding transonic effects of shock-wave boundary-layer interaction on drag.

### CONCLUSIONS

An experimental investigation has been conducted in a perforated, two-dimensional wind tunnel of the transonic pressure distributions of several simple airfoils, in order to provide comparisons with corresponding results from available theory and to indicate the possible existence of perforated-wall interference at transonic speeds. The airfoils included three single wedges of different sizes having  $9^\circ$  included wedge angles and straight afterbodies, a similar single wedge without afterbody, a symmetrical double wedge of  $9^\circ$  included angle, and a circular-arc airfoil 6 percent thick. The Mach numbers varied from 0.7 up to 1.09 for the smallest model, and the Reynolds number per foot was approximately 3.9 million. The following conclusions were drawn from the results of the investigation:

1. Comparisons of experimental pressure distributions and drag at zero lift for the three single wedges with afterbodies showed small but systematic effects of model size for area blockage ratios ranging from 0.36 down to 0.11.

2. The experimental zero-lift pressure distributions agreed relatively well with results given by available theory for the single-wedge, double-wedge, and circular-arc airfoils. The slight but systematic departures from ideal agreement between experiment and theory indicated the existence of an open-jet type of wall interference throughout the Mach number range from 0.7 to 1.09, thus qualitatively verifying recent porous-wall-interference theory. The magnitude of the apparent Mach number shift at sonic speed, however, was about one-half that shown by theory. For models of approximately 1-percent blockage ratio, agreement with theoretical sonic pressure distribution was best for experimental data obtained at a tunnel Mach number of approximately 1.03 but computed for sonic conditions. Even better agreement with sonic theory was obtained for a circular-arc airfoil under choked-flow conditions in a

closed test section and computed for sonic speed. The results also indicated the probable existence of a wall-induced positive pressure gradient over the model chord near sonic speed.

3. The agreement between experimental and theoretical values of zero-lift pressure drag was in general only fair. The discrepancies were attributable partly to the wall-interference effect. In addition, the drag comparisons showed for the circular-arc airfoil at high subsonic speeds a progressive reduction in drag with increasing boundary-layer thickness. This was presumably caused by diffusion through the boundary layer of the increased pressures behind the shock wave near the trailing edge.

4. Experimental zero-lift results for a single-wedge model with and without a straight afterbody indicated only slight effects of the afterbody on pressure distribution and pressure drag for Mach numbers above 0.82. At lower Mach numbers, the pressure drag of the wedge without afterbody was reduced to moderately large negative values as a result of general reductions in surface pressures from those measured in the presence of the afterbody. The magnitude of this pressure decrement became larger for points approaching the shoulder of the wedge.

5. At angle of attack, viscous effects were evident as negative aerodynamic loadings over the rear portions of the double-wedge and circular-arc airfoils at subsonic Mach numbers. Addition of distributed roughness near the leading edge of the circular-arc model reduced the extent of negative loadings, more than doubled the lift-curve slope at Mach numbers up to 0.93, and eliminated most of the extreme forward center-of-pressure travel near 0.92 Mach number.

Ames Research Center

National Aeronautics and Space Administration  
Moffett Field, Calif., Mar. 17, 1959

## REFERENCES

1. Guderley, Gottfried, and Yoshihara, Hideo: The Flow Over a Wedge Profile at Mach Number 1. Jour. Aero. Sci., vol. 17, no. 11, Nov. 1950, pp. 723-735.
2. Yoshihara, Hideo: On the Flow Over a Finite Wedge in the Lower Transonic Region. WADC Tech. Rep. 56-268, June 1956.
3. Vincenti, Walter G., and Wagoner, Cleo B.: Transonic Flow Past a Wedge Profile With Detached Bow Wave. NACA Rep. 1095, 1952.
4. Cole, Julian D.: Drag of a Finite Wedge at High Subsonic Speeds. Jour. Math. and Phys., vol. XXX, no. 3, July 1951, pp. 79-93.
5. Guderley, Gottfried, and Yoshihara, Hideo: Two-Dimensional Unsymmetric Flow Patterns at Mach Number 1. Jour. Aero. Sci., vol. 20, no. 11, Nov. 1953, pp. 757-768.
6. Spreiter, John R., and Alksne, Alberta: Theoretical Prediction of Pressure Distributions on Nonlifting Airfoils at High Subsonic Speeds. NACA Rep. 1217, 1955. (Supersedes NACA TN 3096)
7. Spreiter, John R., and Alksne, Alberta Y.: Thin Airfoil Theory Based on Approximate Solution of the Transonic Flow Equation. NACA TN 3970, 1957.
8. Spreiter, John R., Alksne, Alberta Y., and Hyett, B. Jeanne: Theoretical Pressure Distributions for Several Related Nonlifting Airfoils at High Subsonic Speeds. NACA TN 4148, 1958.
9. Bryson, Arthur Earl, Jr.: An Experimental Investigation of Transonic Flow Past Two-Dimensional Wedge and Circular-Arc Sections Using a Mach-Zehnder Interferometer. NACA Rep. 1094, 1952. (Supersedes NACA TN 2560)
10. Michel, R., Marchaud, F., and Le Gallo, J.: Étude des écoulements transsoniques autour des profils lenticulaire, à incidence nulle. O.N.E.R.A. Pub. No. 65, 1953.
11. Vincenti, Walter G., Dugan, Duane W., and Phelps, E. Ray: An Experimental Study of the Lift and Pressure Distribution on a Double-Wedge Profile at Mach Numbers Near Shock Attachment. NACA TN 3225, 1954.
12. Braslow, Albert L., and Knox, Eugene C.: Simplified Method for Determination of Critical Height of Distributed Roughness Particles for Boundary-Layer Transition at Mach Numbers From 0 to 5. NACA TN 4363, 1958.

13. Pankhurst, R. C., and Holder, D. W.: Wind-tunnel Technique. Sir Isaac Pitnam and Sons, Ltd. (London), 1952, pp. 378-380.
14. Schwartzberg, Milton A.: Effects of Roughness and Reynolds Number on the Nonlinear Lift Characteristics of a Wing With Modified Hexagonal Airfoil Sections. NACA RM L52L26a, 1953.
15. Stivers, Louis S., Jr., and Lippmann, Garth W.: Effects of Fixing Boundary-Layer Transition for an Unswept-Wing Model and an Evaluation of Porous Tunnel-Wall Interference for Mach Numbers From 0.60 to 1.40. NACA TN 4228, 1958.
16. Summers, James L., and Page, William A.: Lift and Moment Characteristics at Subsonic Mach Numbers of Four 10-Percent-Thick Airfoil Sections of Varying Trailing-Edge Thickness. NACA RM A50J09, 1950.
17. von Kármán, Theodore: The Similarity Law of Transonic Flow. Jour. Math. and Phys., vol. XXVI, no. 3, Oct. 1947, pp. 182-190.
18. Spreiter, John R.: On the Application of Transonic Similarity Rules to Wings of Finite Span. NACA Rep. 1153, 1953. (Supersedes NACA TN 2726)
19. Baldwin, Barrett S., Jr., Turner, John B., and Knechtel, Earl D.: Wall Interference in Wind Tunnels With Slotted and Porous Boundaries at Subsonic Speeds. NACA TN 3176, 1954. (Supersedes NACA RM A53E29)
20. Berndt, Sune B.: Theoretical Aspects of the Calibration of Transonic Test Sections. Flygtekniska Forsöksanstalten Rep. 74, Stockholm, Sweden, 1957. (Supersedes FFA Rapp. AE-400)
21. Page, William A.: Experimental Study of the Equivalence of Transonic Flow About Slender Cone-Cylinders of Circular and Elliptic Cross Section. NACA TN 4233, 1958.
22. Barish, David T., and Guderley, Gottfried: Asymptotic Forms of Shock Waves in Flows Over Symmetrical Bodies at Mach 1. Jour. Aero. Sci., vol. 20, no. 7, July 1953, pp. 491-499.
23. Marschner, Bernard W.: The Flow Over a Body in a Choked Wind Tunnel and in a Sonic Free Jet. Jour. Aero. Sci., vol. 23, no. 4, April 1956, pp. 368-376.
24. Liepmann, H. W., and Roshko, A.: Elements of Gasdynamics. John Wiley & Sons, Inc., 1957, pp. 342-346.

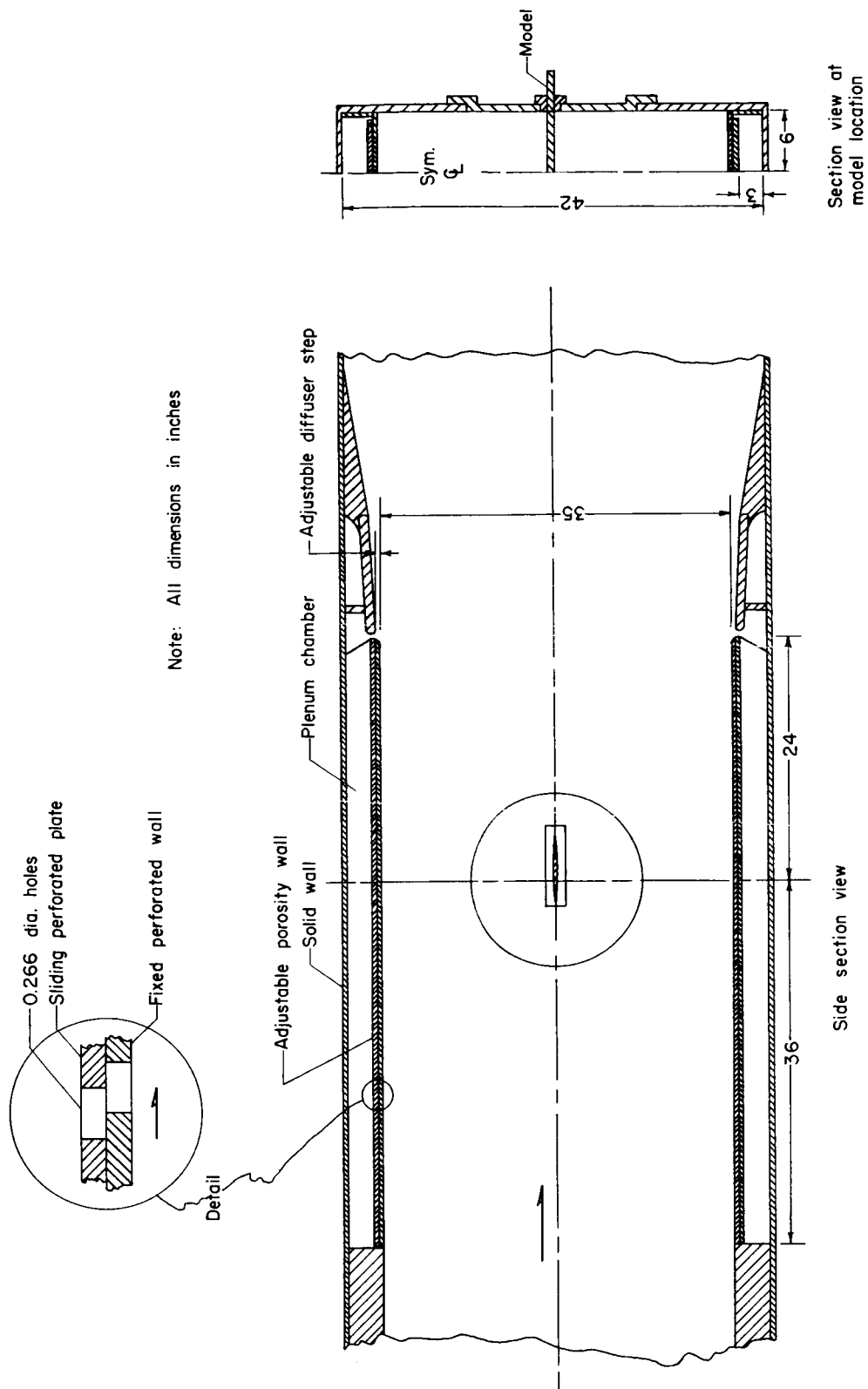
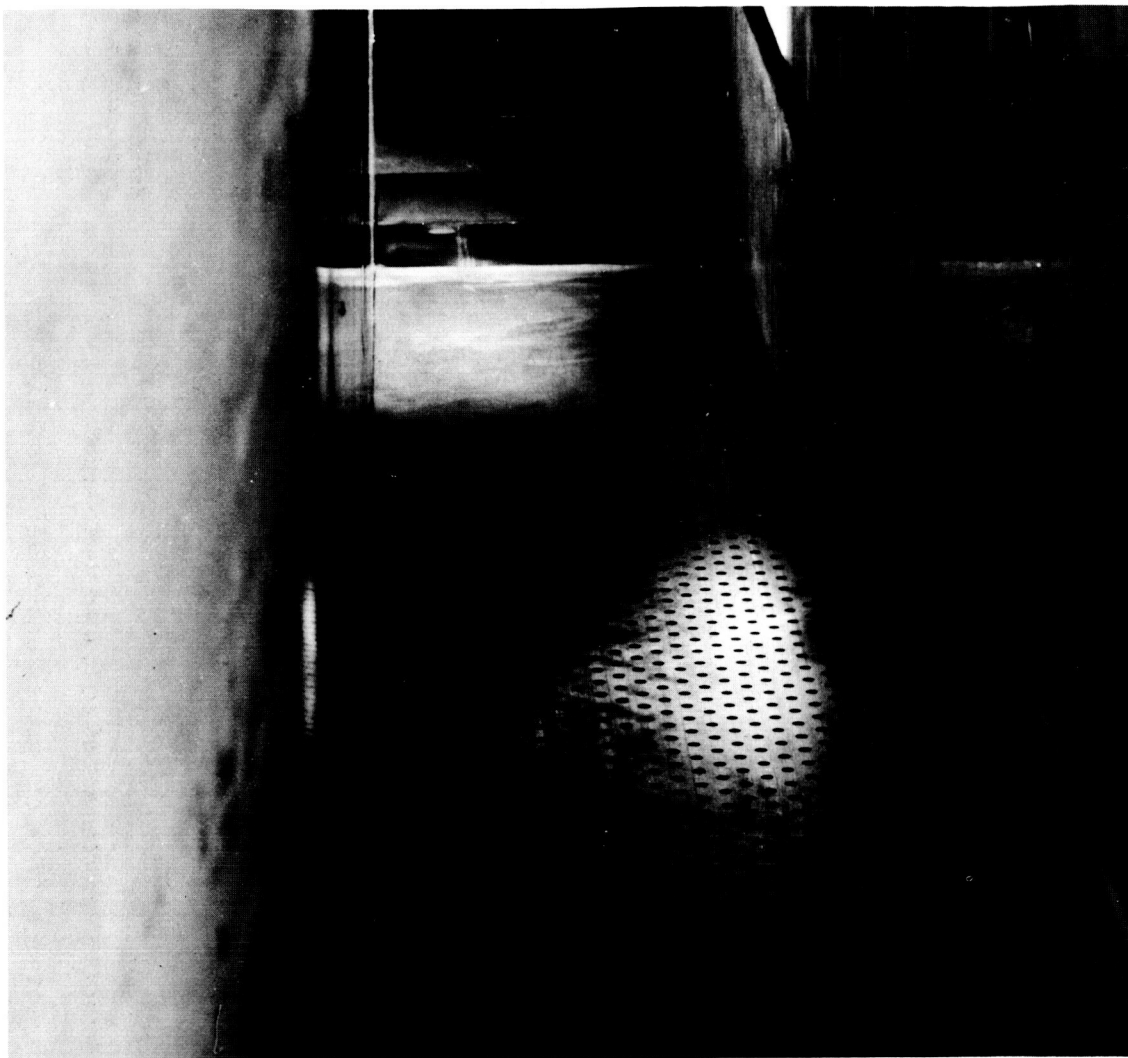


Figure 1.- Details of wind tunnel and model installation.



(b) Survey tube installed in the test section.

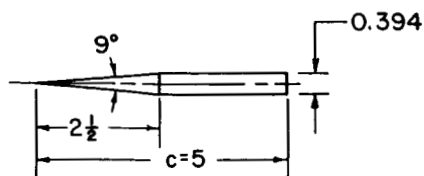
A-23553

Figure 1.- Concluded.

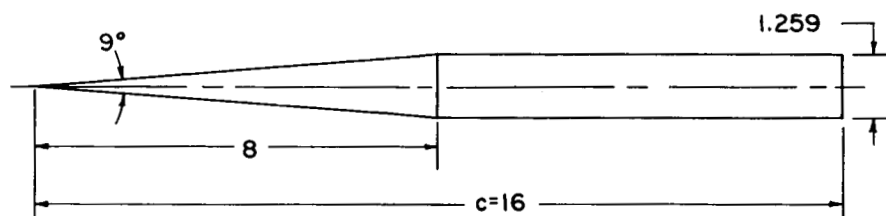
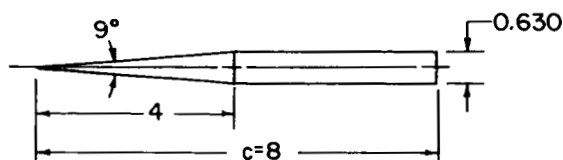


All dimensions in inches

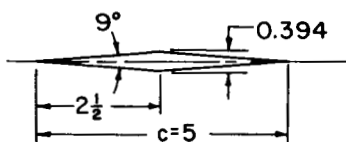
Orifice locations  
 $2\frac{1}{2}$ -inch wedge (Top only)  
 $x/c = .06, .15, .20, .35, .44, .48$



4-inch and 8-inch wedges)  
 (Top and bottom surfaces)  
 $x/c = .062, .093, .125, .187, .250, .312, .375, .438, .495$

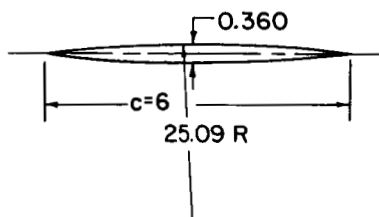


Double wedge (Top only)  
 $x/c = .06, .15, .20, .35, .44, .48, .52, .56, .60, .65, .75, .84, .88, .94$



Wedge models 7.87-percent-chord thick

Circular-arc airfoil  
 (Top and bottom surfaces)  
 $x/c = .05, .10, .15, .20, .25, .30, .35, .40, .45, .475, .50, .525, .55, .60, .65, .70, .75, .80, .85, .90, .95$



Circular-arc model 6-percent-chord thick

Figure 2.- Airfoil section details and orifice locations.

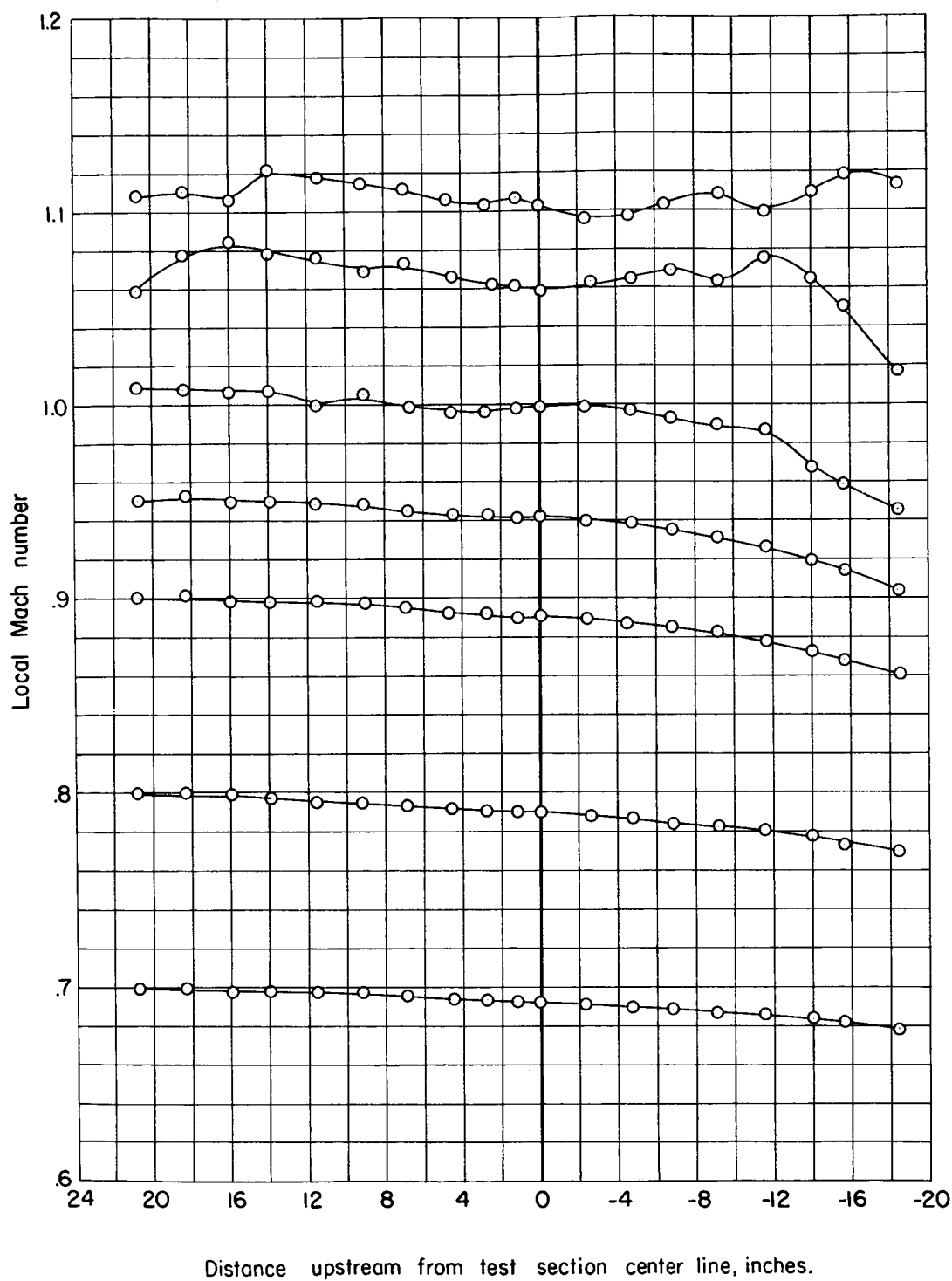
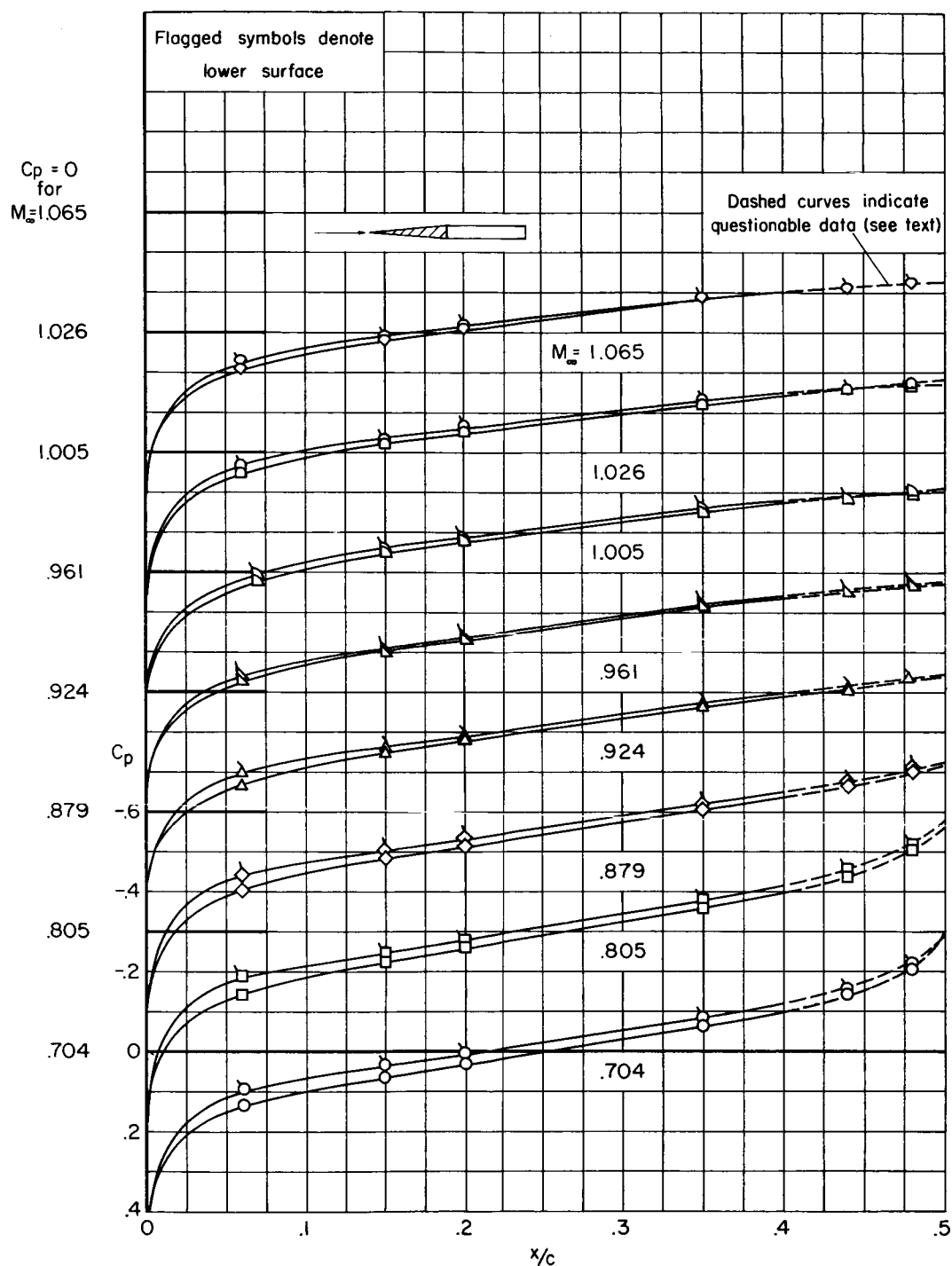
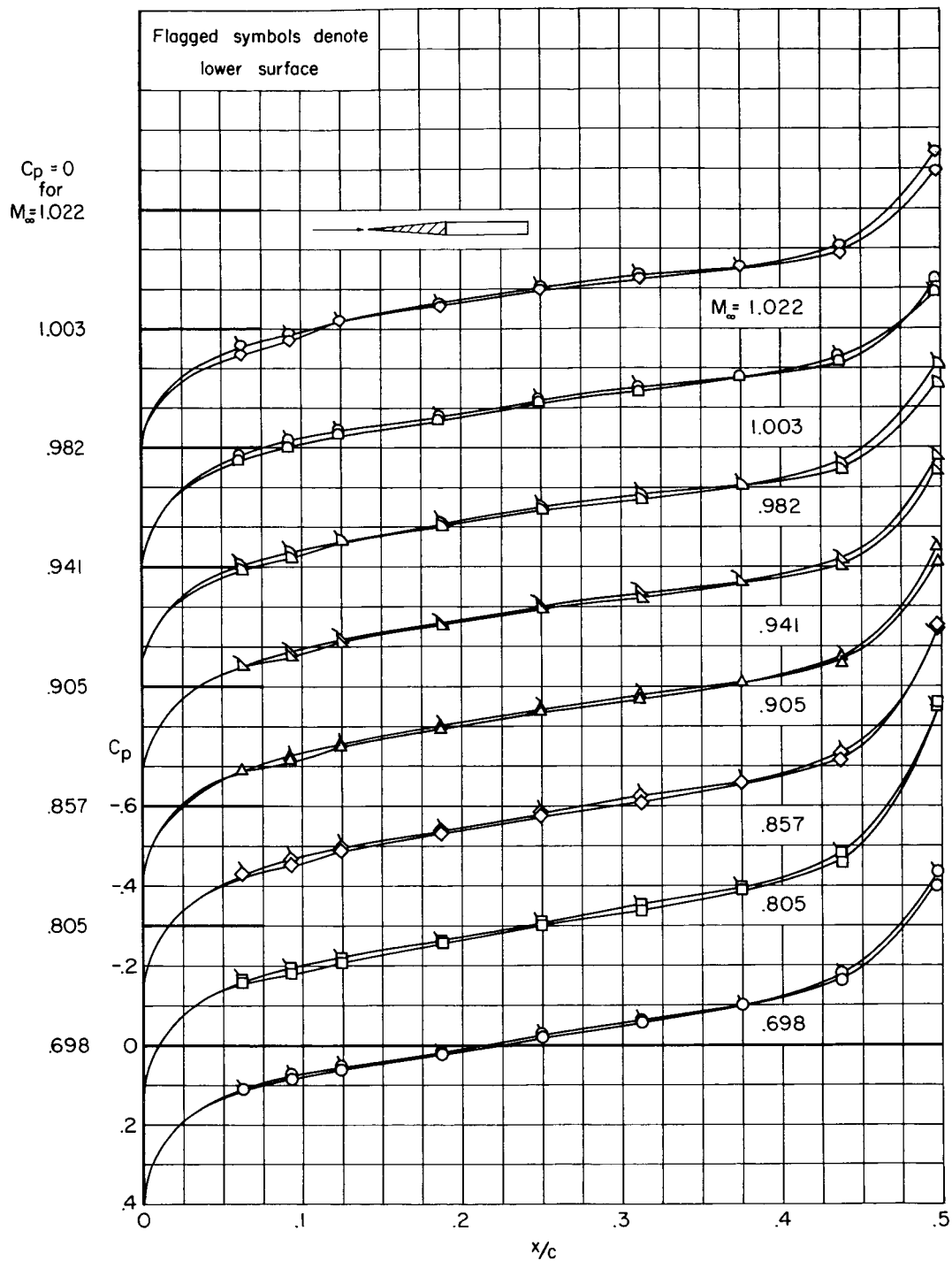


Figure 3.- Axial distribution of Mach number in the Ames 1- by 3-1/2 foot wind tunnel with perforated walls of 5 percent porosity.



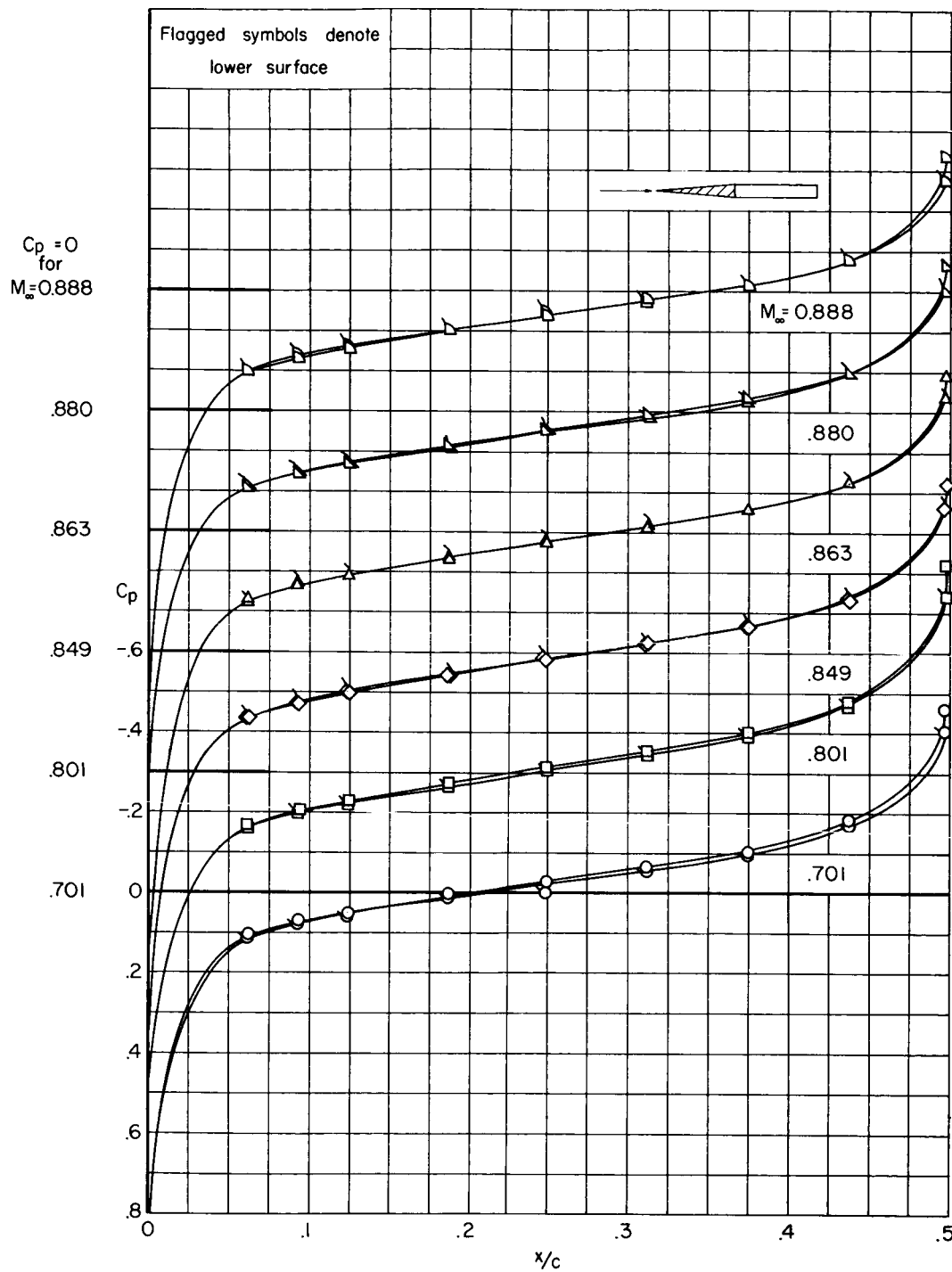
(a)  $2\frac{1}{2}$ -inch wedge with straight afterbody.

Figure 4.- Representative pressure distributions over single-wedge airfoils at  $\alpha_0 = 0^\circ$ .



(b) 4-inch wedge with straight afterbody.

Figure 4.- Continued.



(c) 8-inch wedge with straight afterbody.

Figure 4.- Continued.

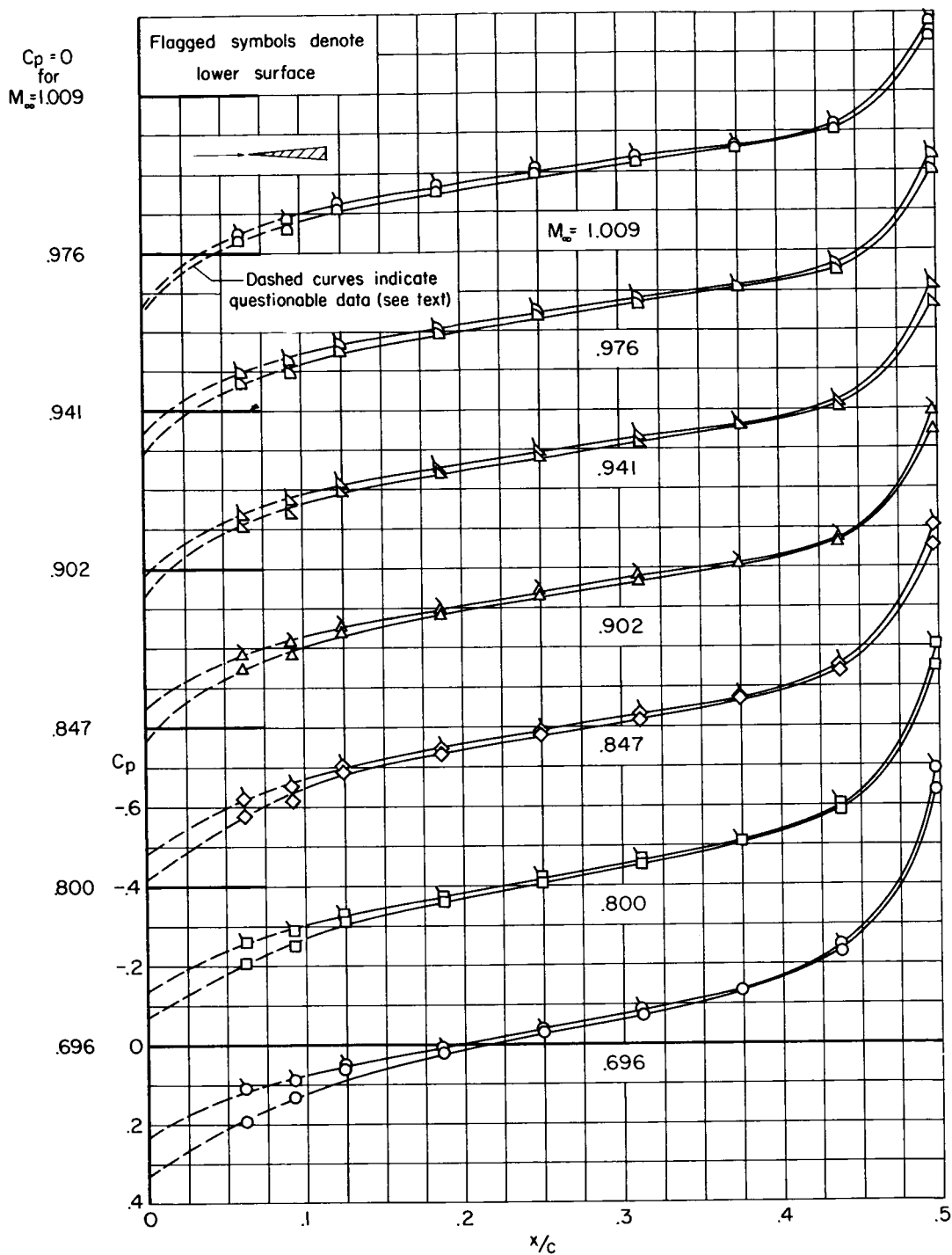


Figure 4.- Concluded.

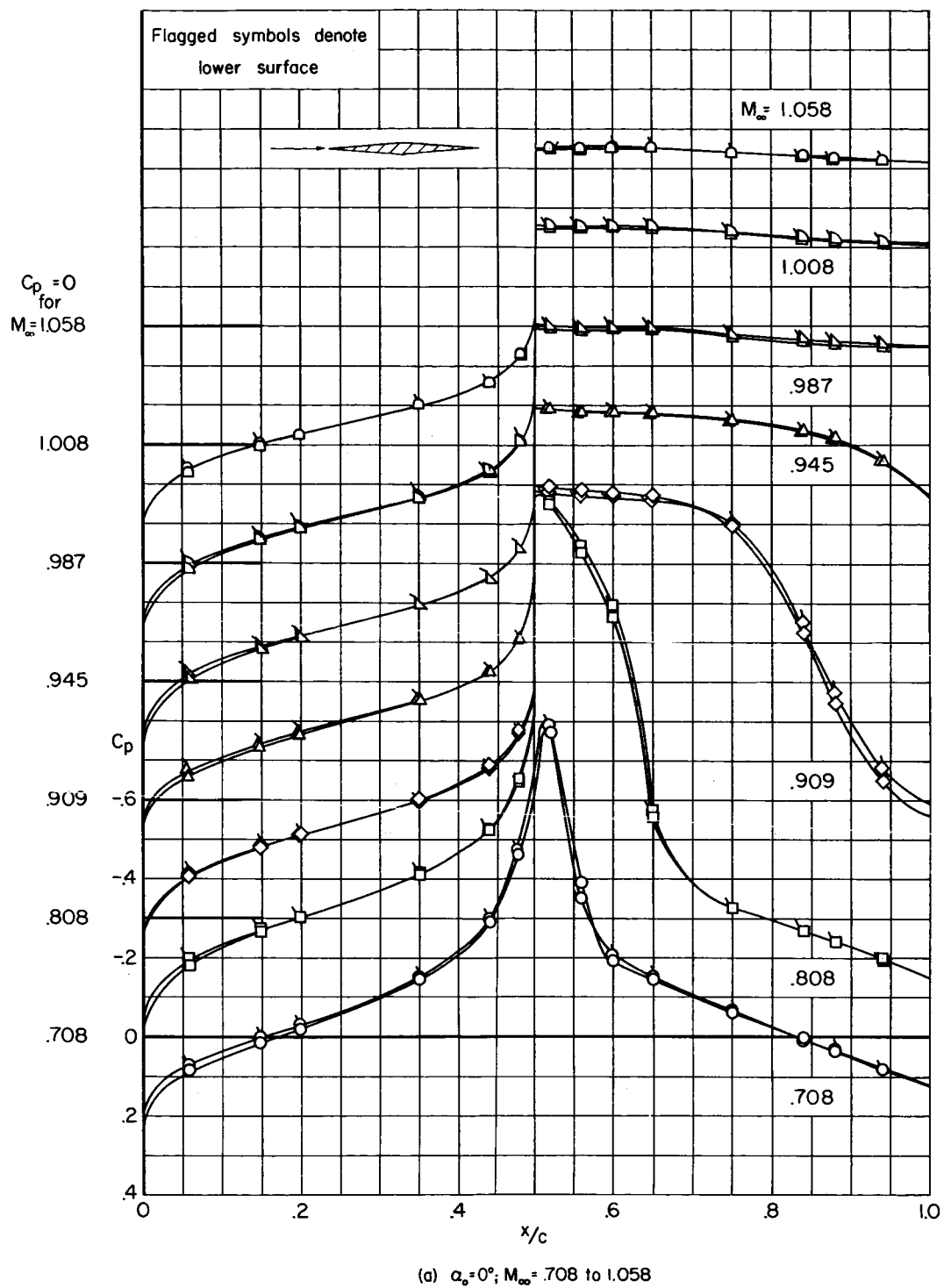


Figure 5.- Representative pressure distributions over the double-wedge airfoil.

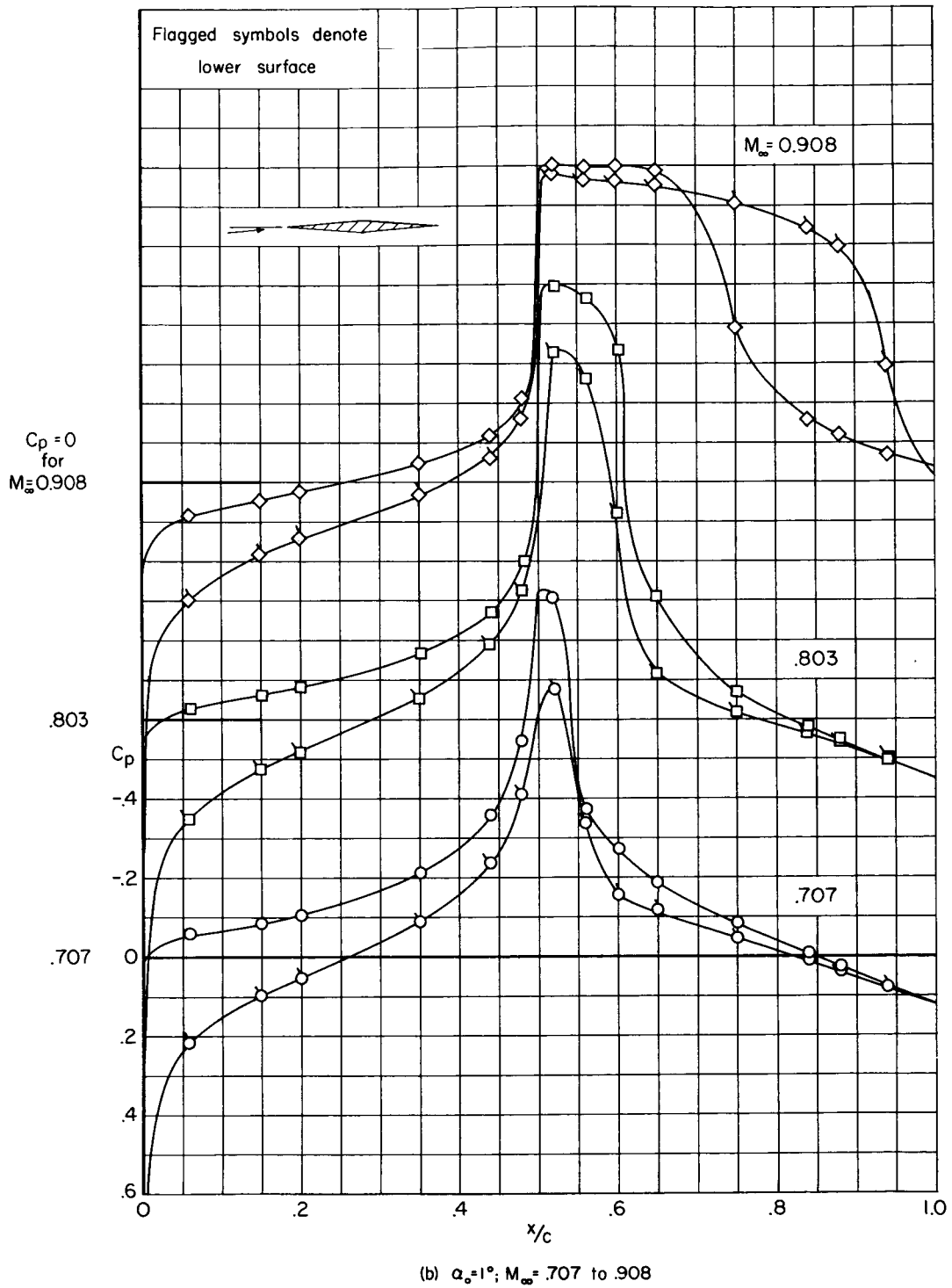
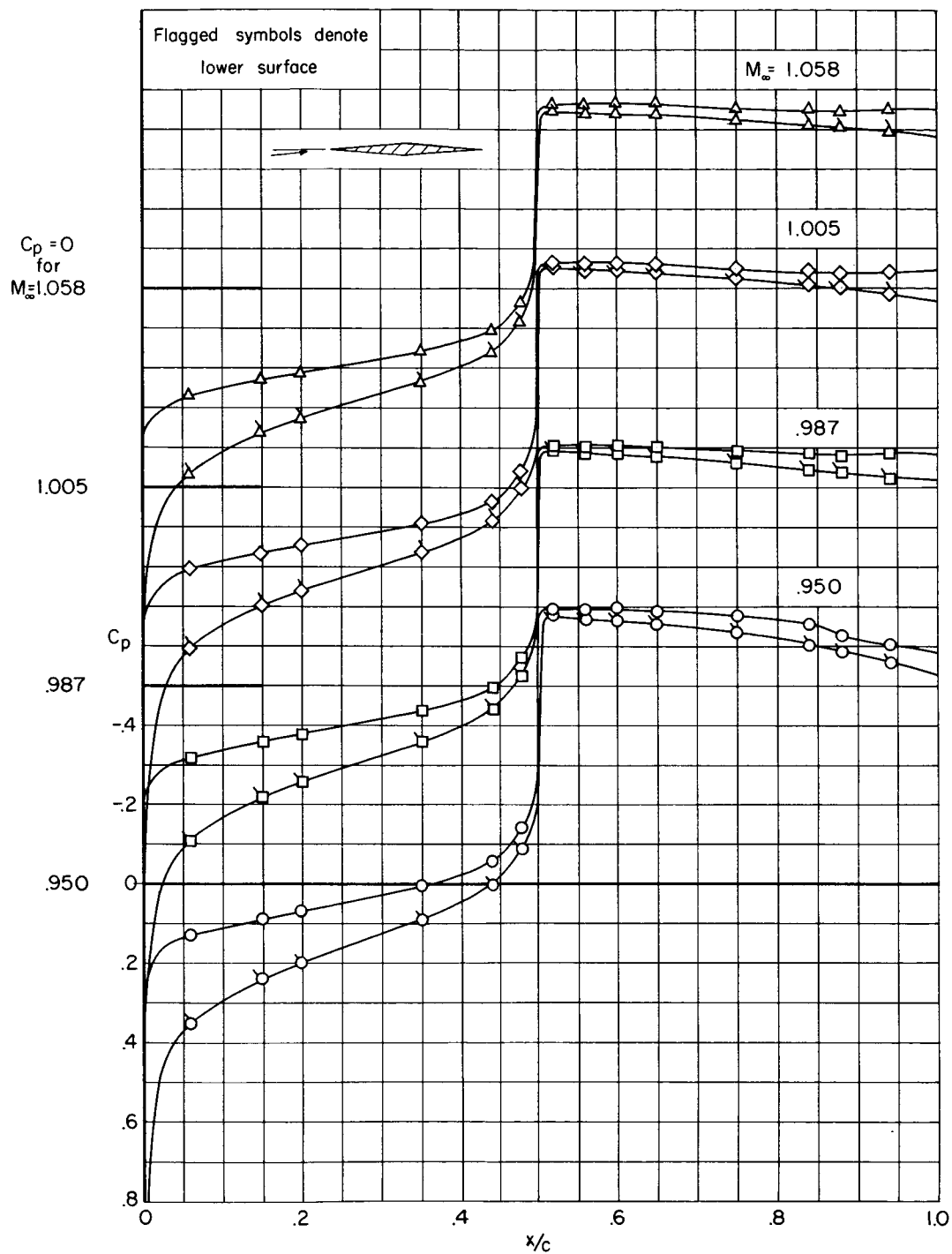


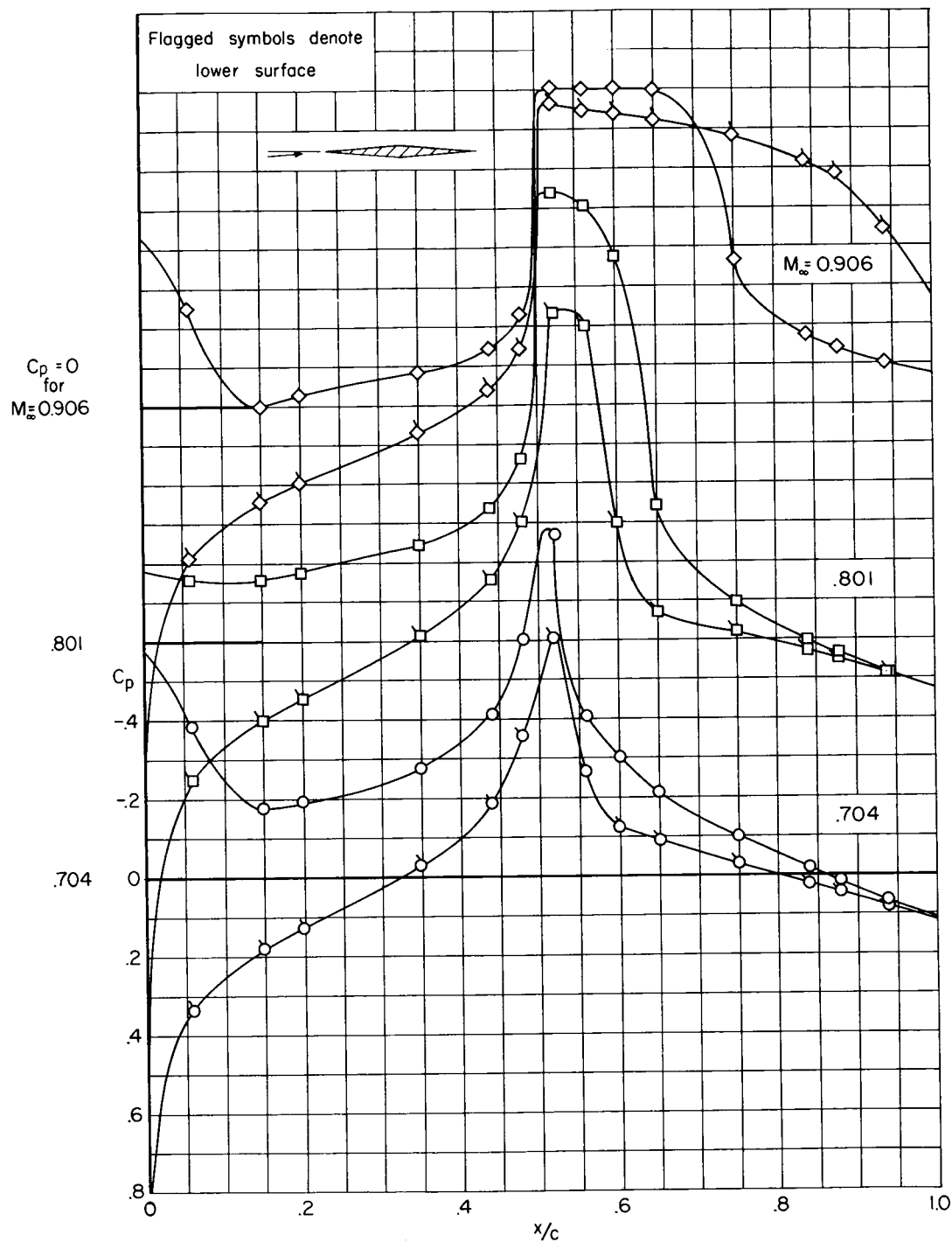
Figure 5.- Continued.





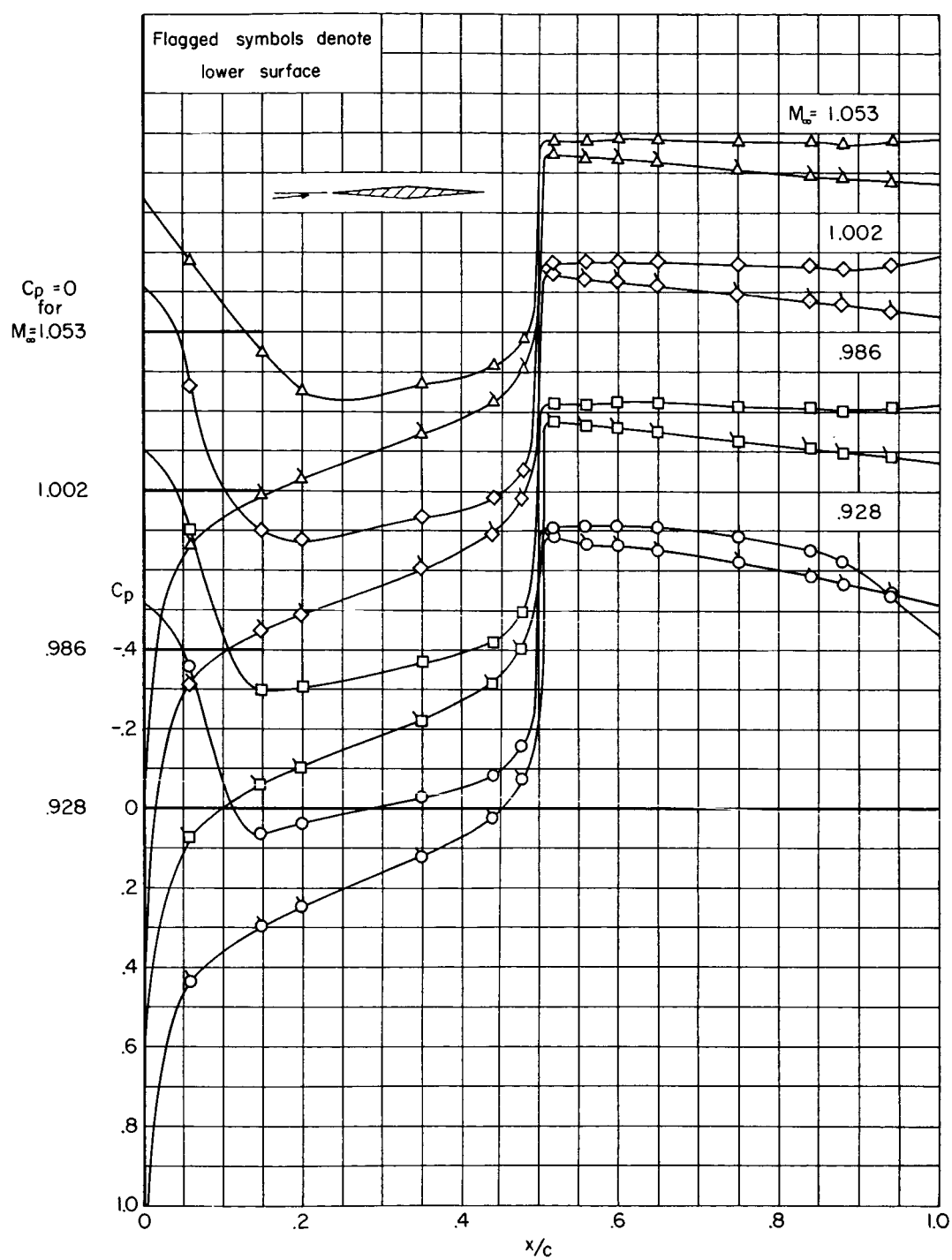
(c)  $\alpha_o = 1^\circ$ ;  $M_\infty = .950$  to 1.058

Figure 5.-Continued.



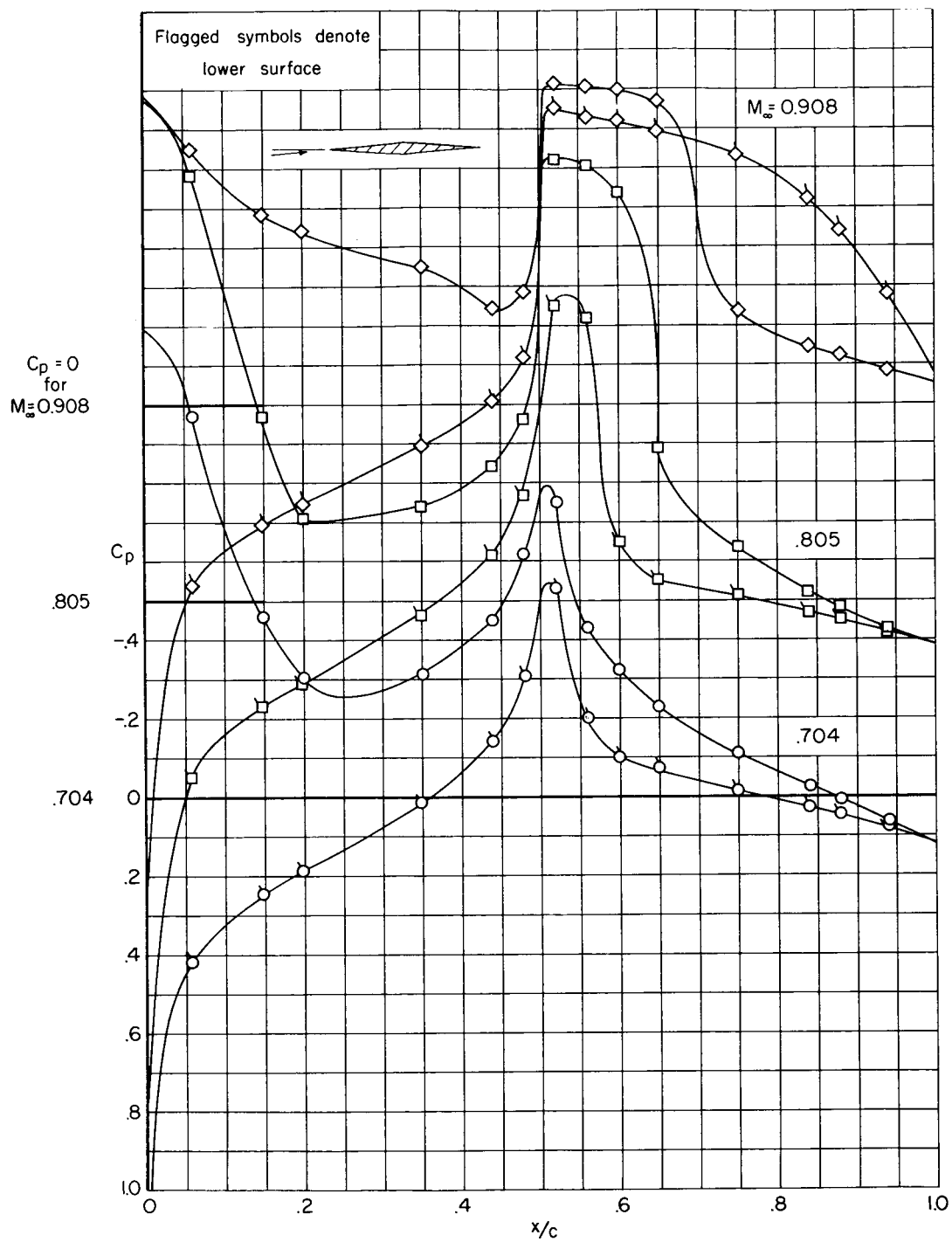
(d)  $\alpha_0 = 2^\circ$ ;  $M_\infty = .704$  to .906

Figure 5.- Continued.



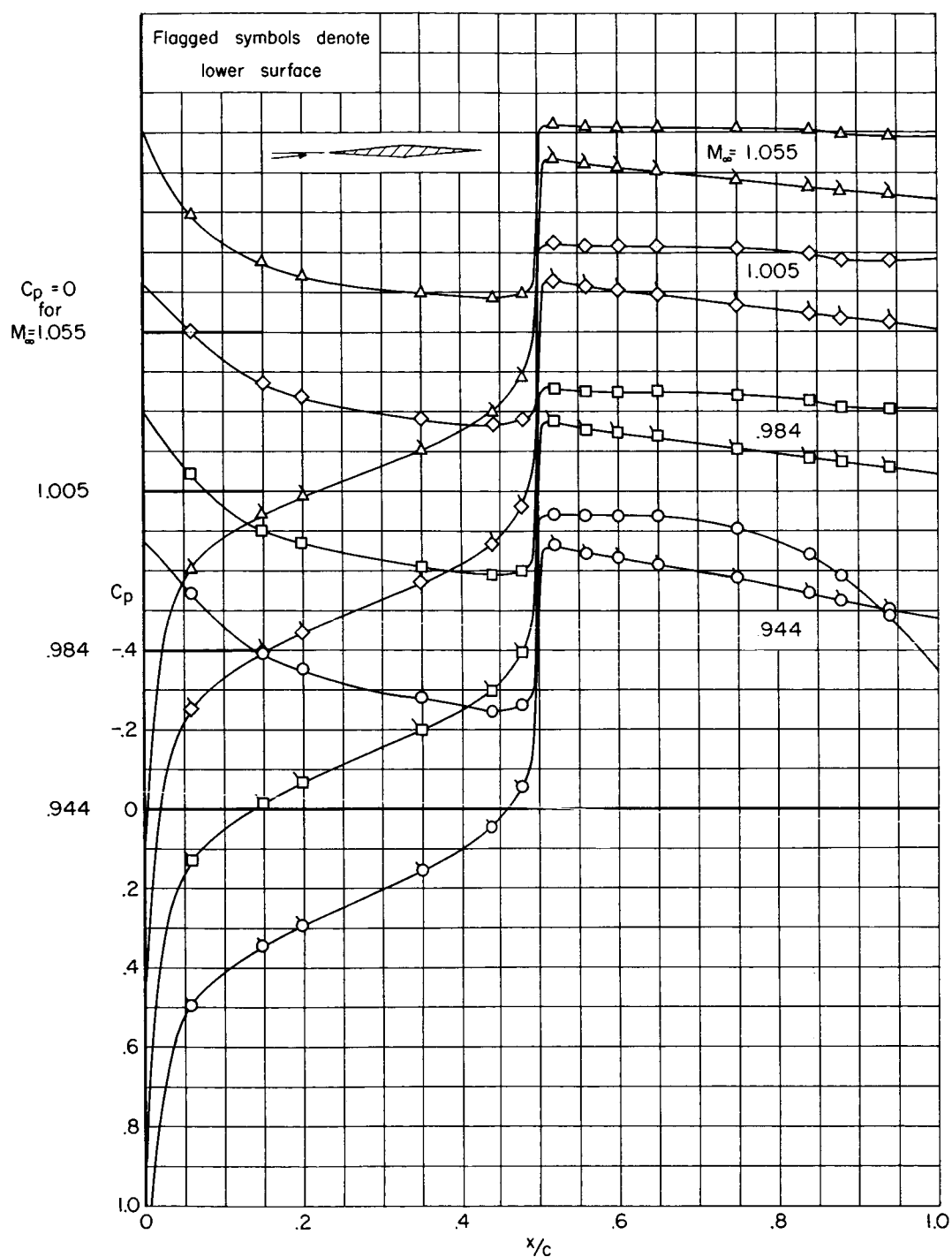
(e)  $\alpha_o = 2^\circ$ ;  $M_\infty = .928$  to 1.053

Figure 5.- Continued.



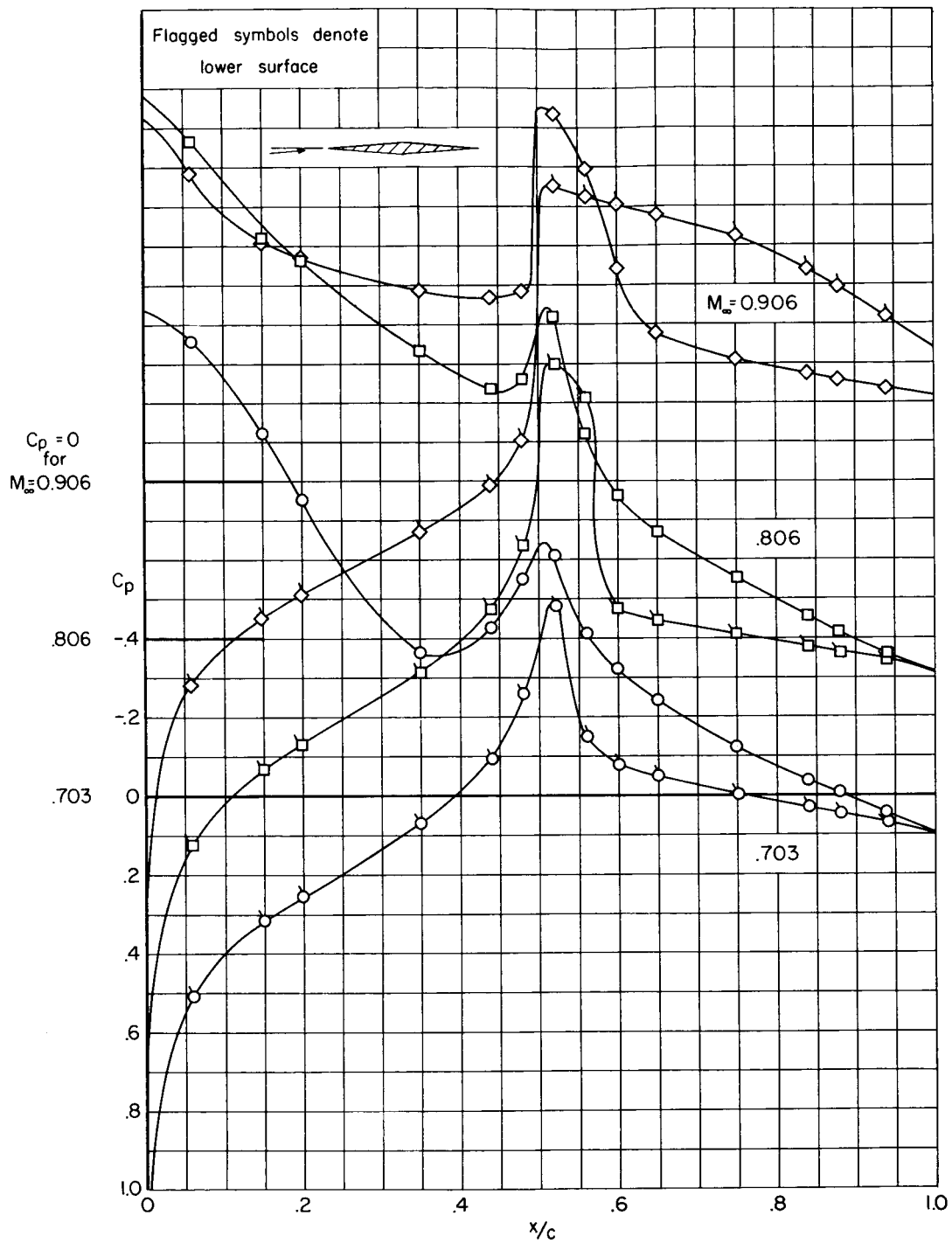
(f)  $\alpha_o = 3^\circ$ ;  $M_\infty = .704$  to  $.908$

Figure 5.- Continued.



(g)  $\alpha_o = 3^\circ$ ;  $M_\infty = .944$  to 1.055

Figure 5.- Continued.



(h)  $\alpha_o = 4^\circ$ ;  $M_\infty = .703$  to .906

Figure 5.- Continued.

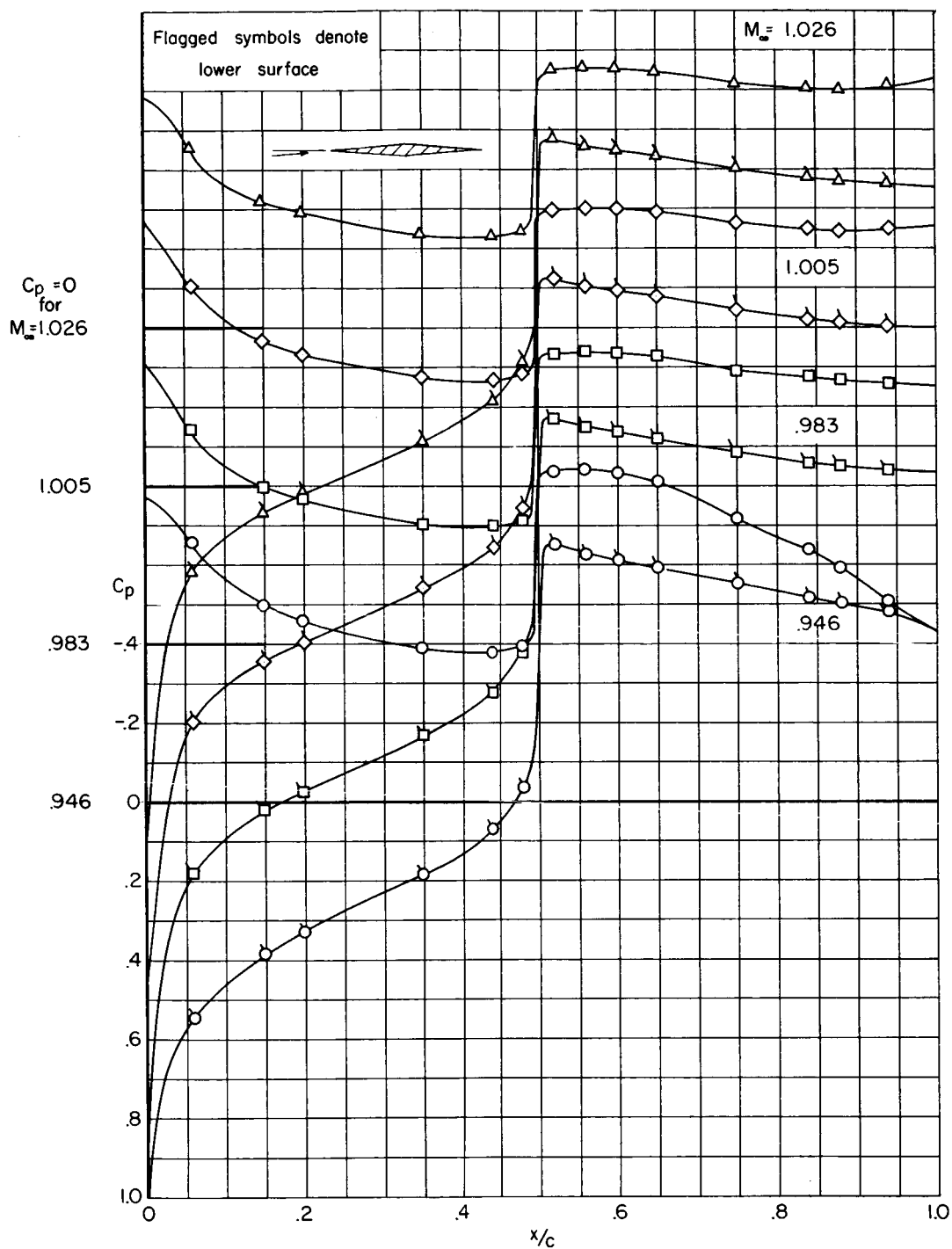


Figure 5.- Concluded.

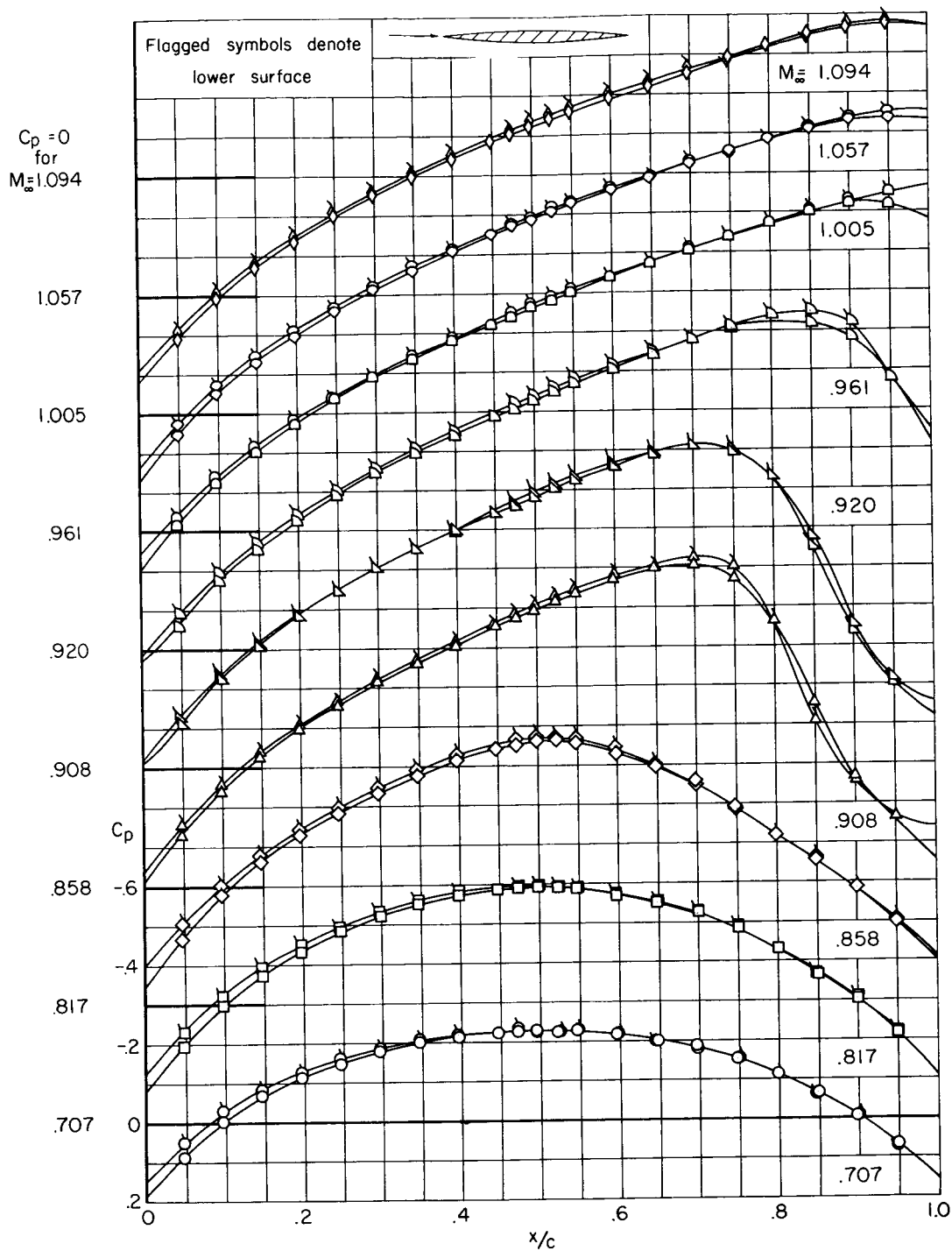
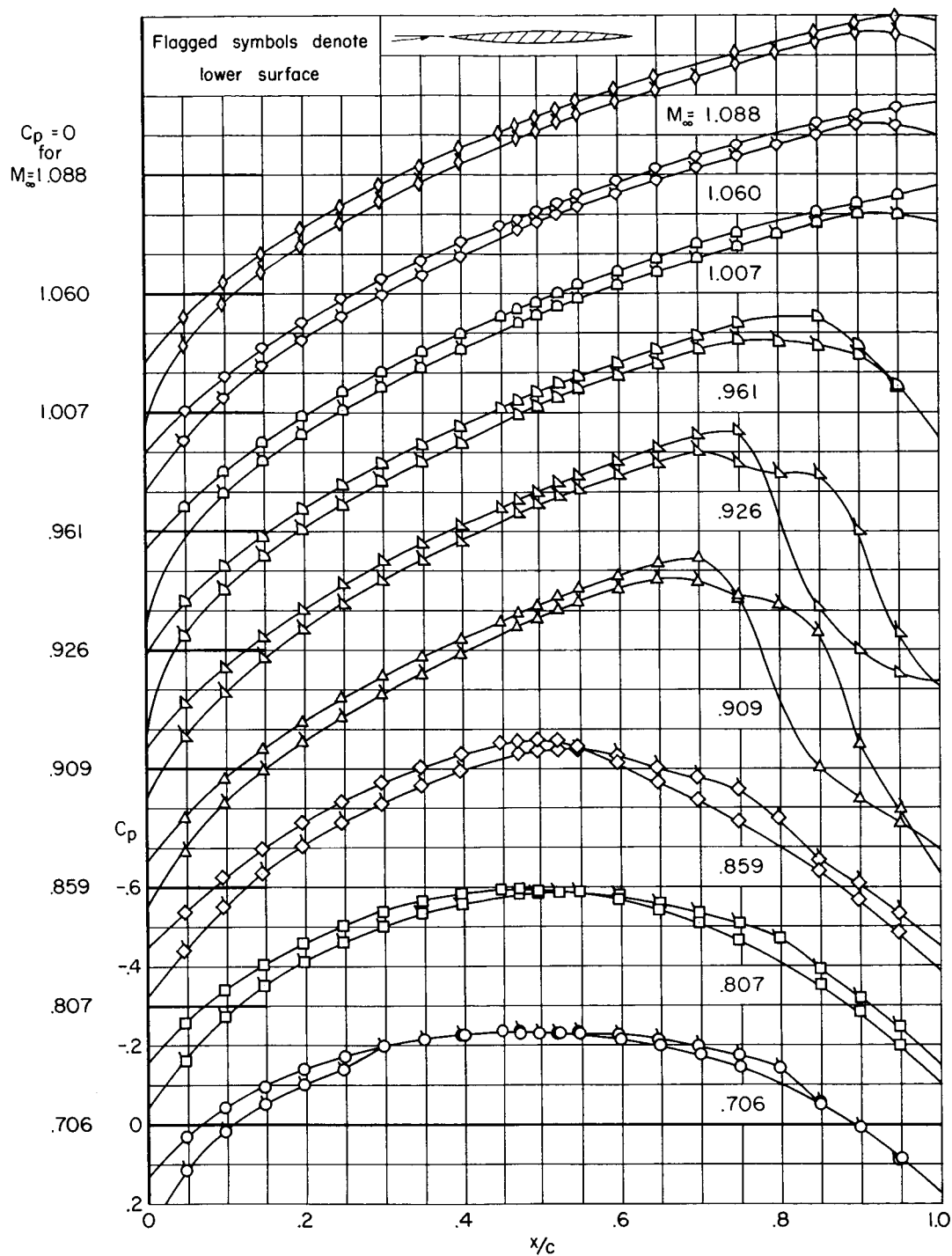


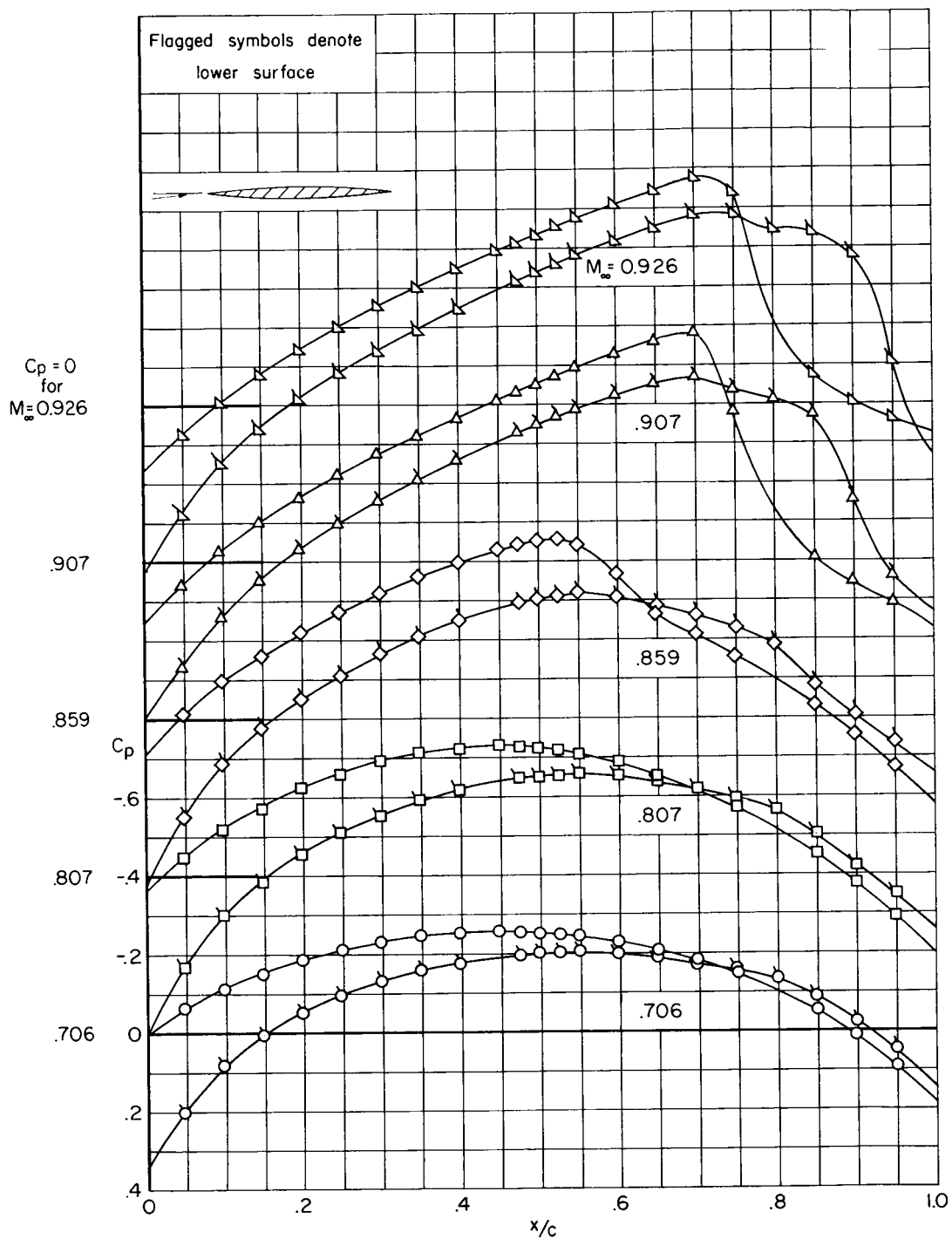
Figure 6.- Representative pressure distributions for 6-percent-thick circular-arc airfoil.





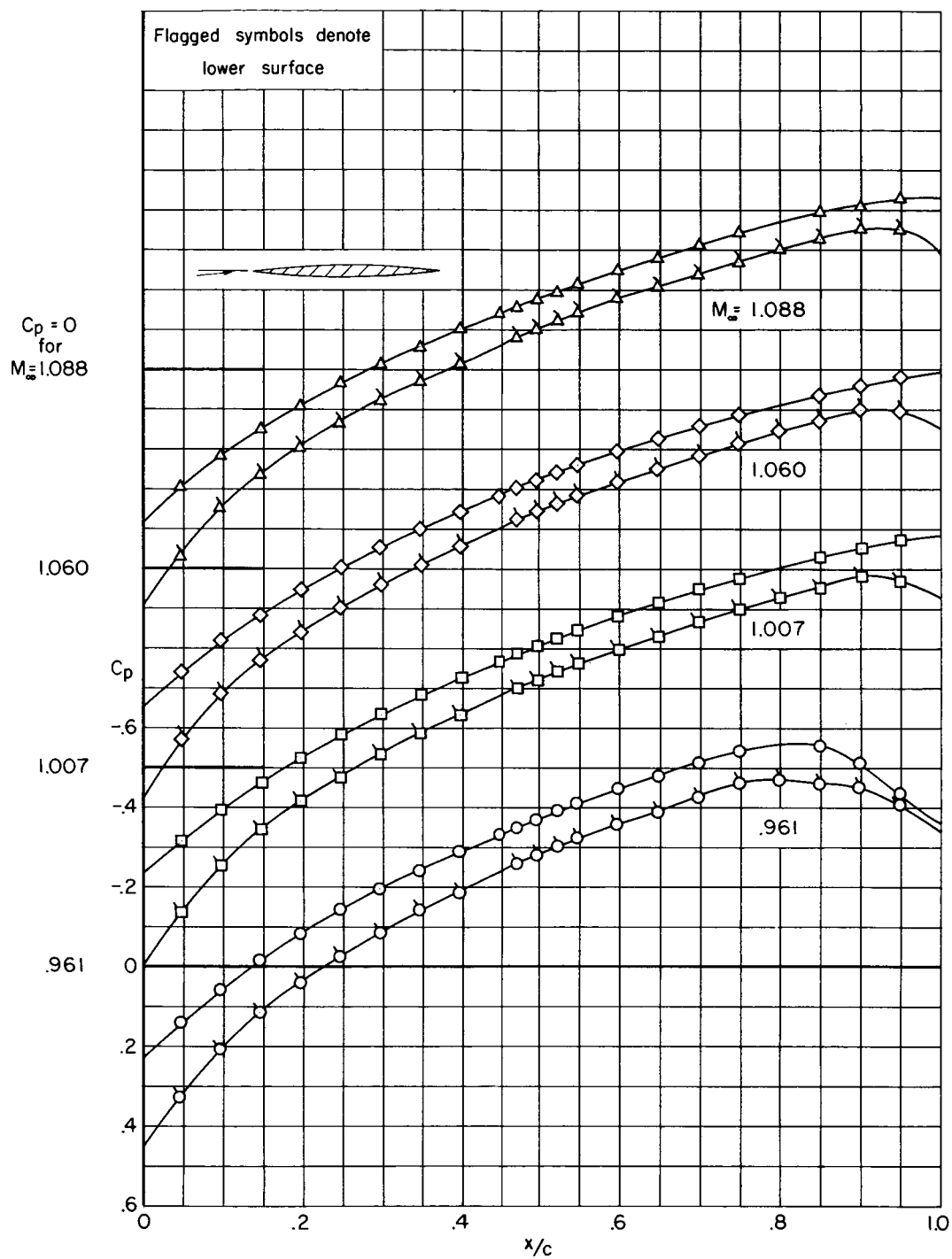
(b)  $\alpha_o = 5^\circ$ ;  $M_\infty = .706$  to 1.088

Figure 6.- Continued.



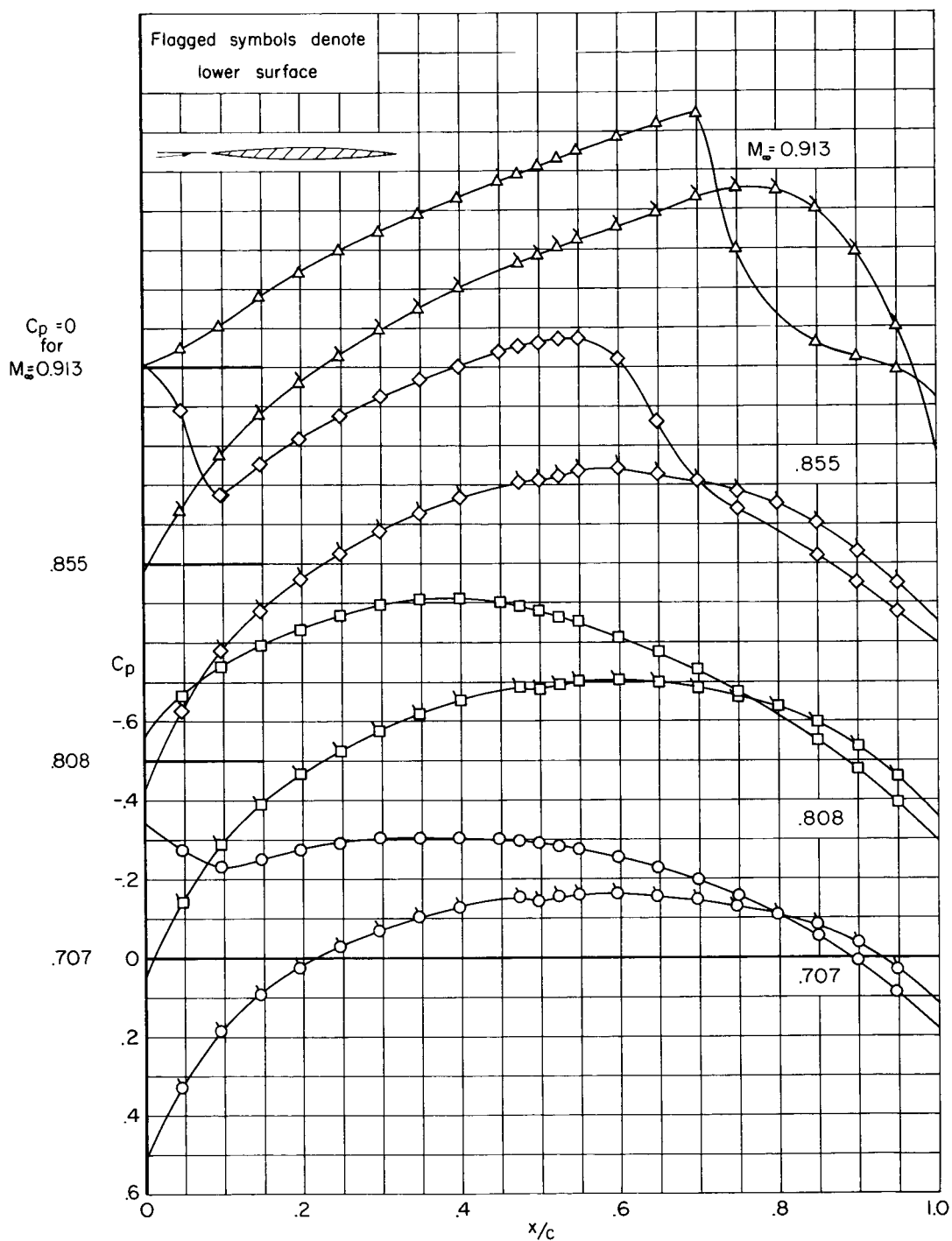
(c)  $\alpha_o = 1^\circ$ ;  $M_\infty = .706$  to .926

Figure 6.- Continued.



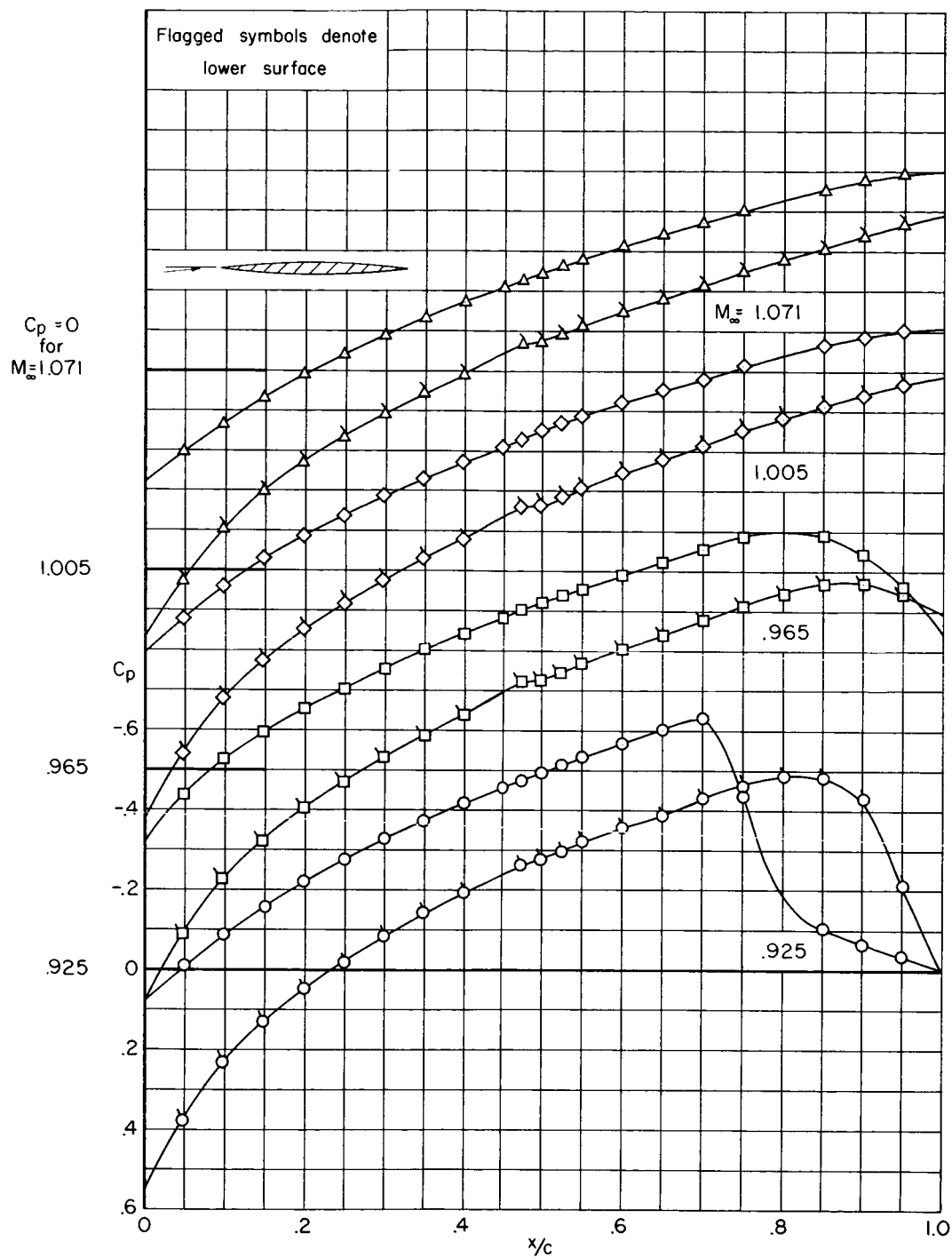
(d)  $\alpha_o = 1^\circ$ ;  $M_\infty = .961$  to  $1.088$

Figure 6.- Continued.



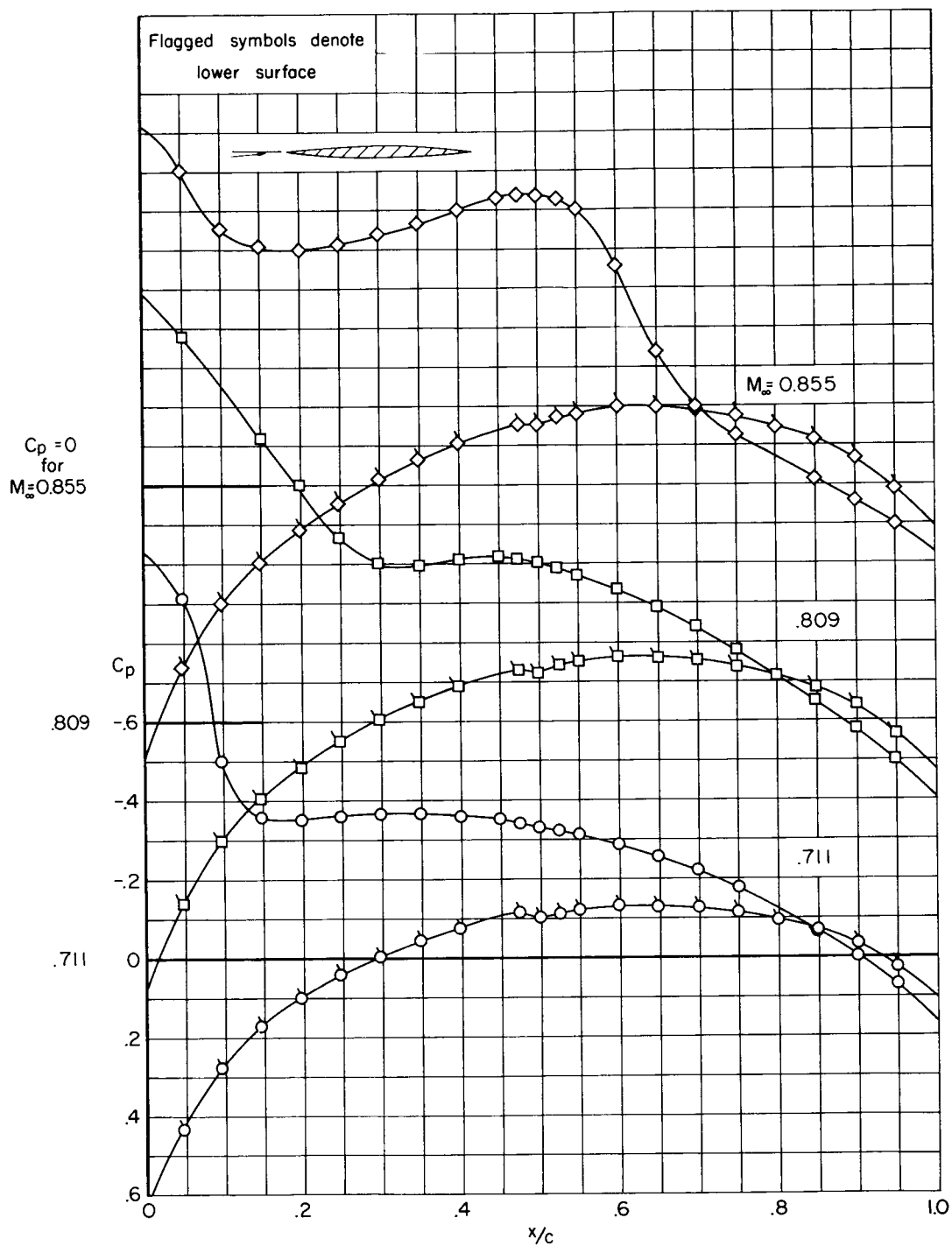
(e)  $\alpha_o = 2^\circ$ ;  $M_\infty = .707$  to  $.913$

Figure 6.- Continued.



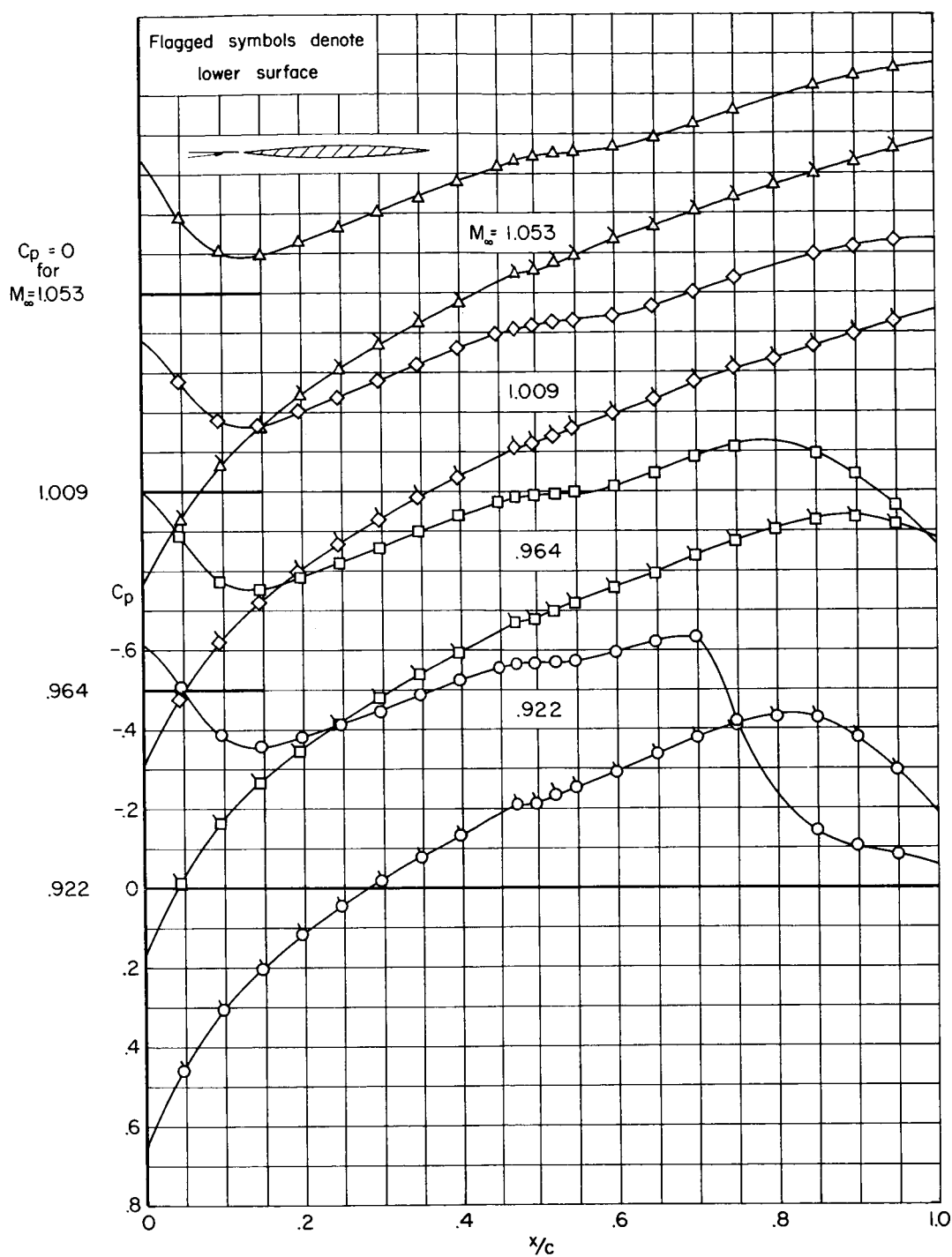
(f)  $\alpha_o = 2^\circ$ ;  $M_\infty = .925$  to 1.071

Figure 6.- Continued.



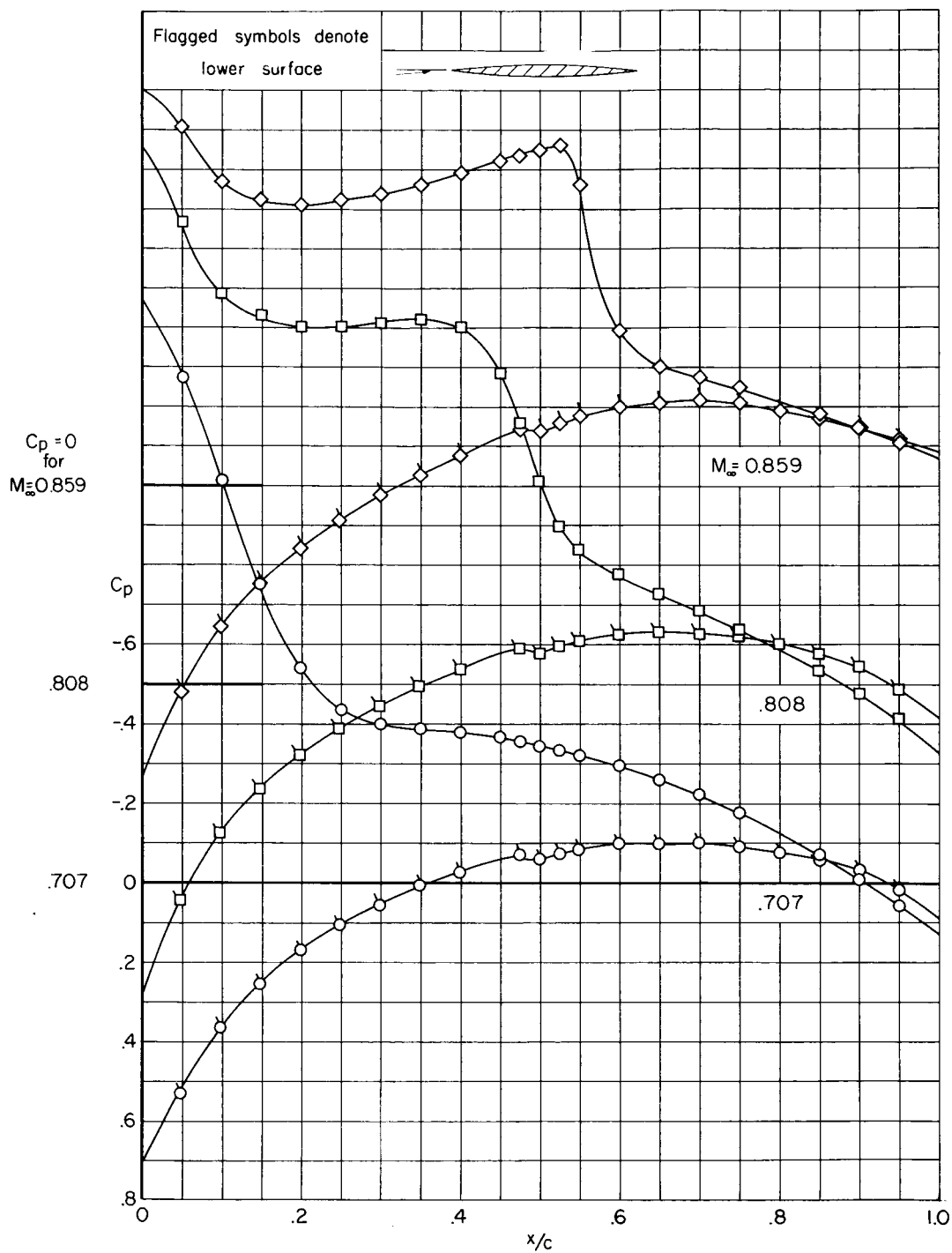
(g)  $\alpha_o = 3^\circ$ ;  $M_\infty = .711$  to .855

Figure 6.- Continued.



(h)  $\alpha_o = 3^\circ$ ;  $M_\infty = .922$  to 1.053

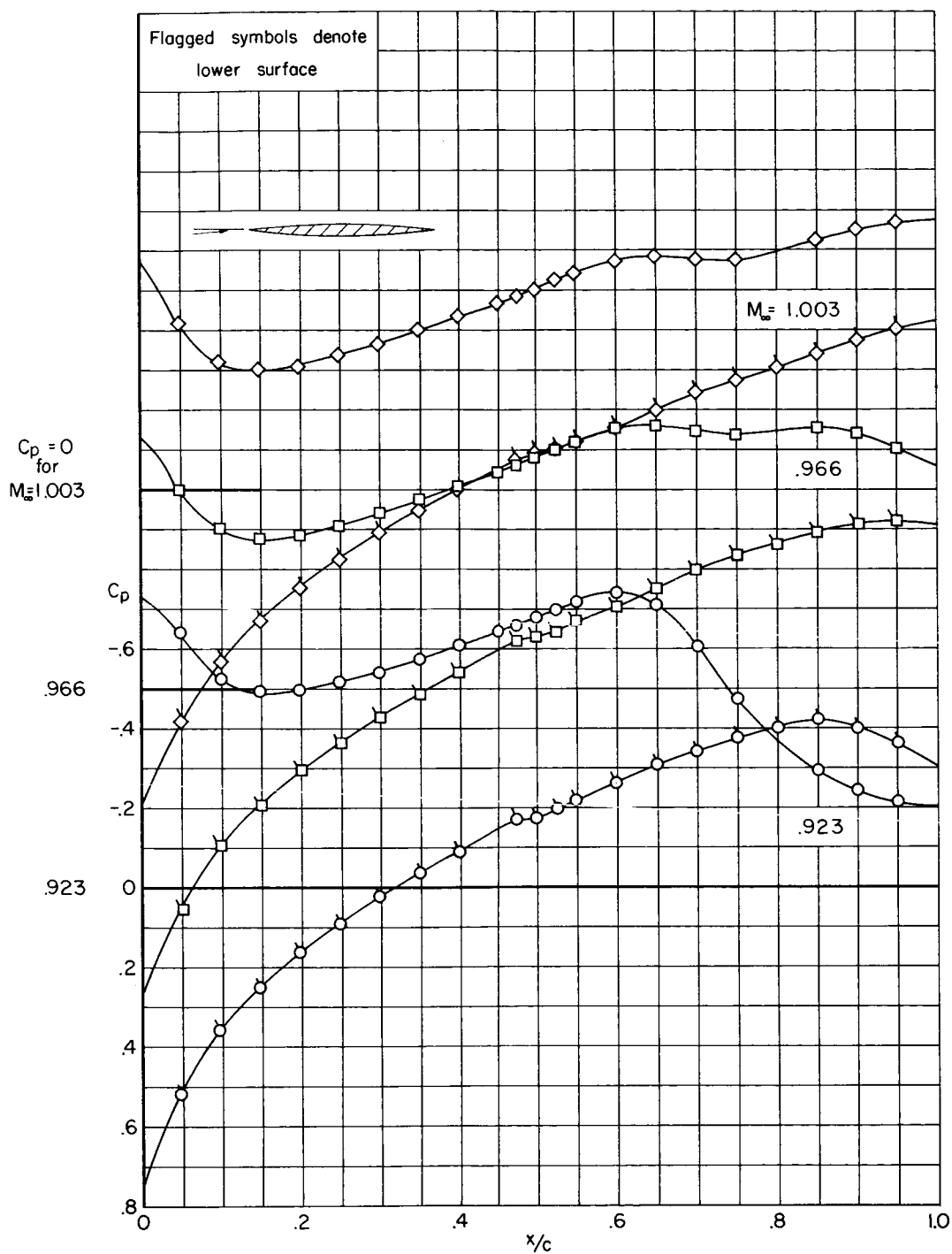
Figure 6.- Continued.



(i)  $\alpha_o = 4^\circ$ ;  $M_\infty = .707$  to .859

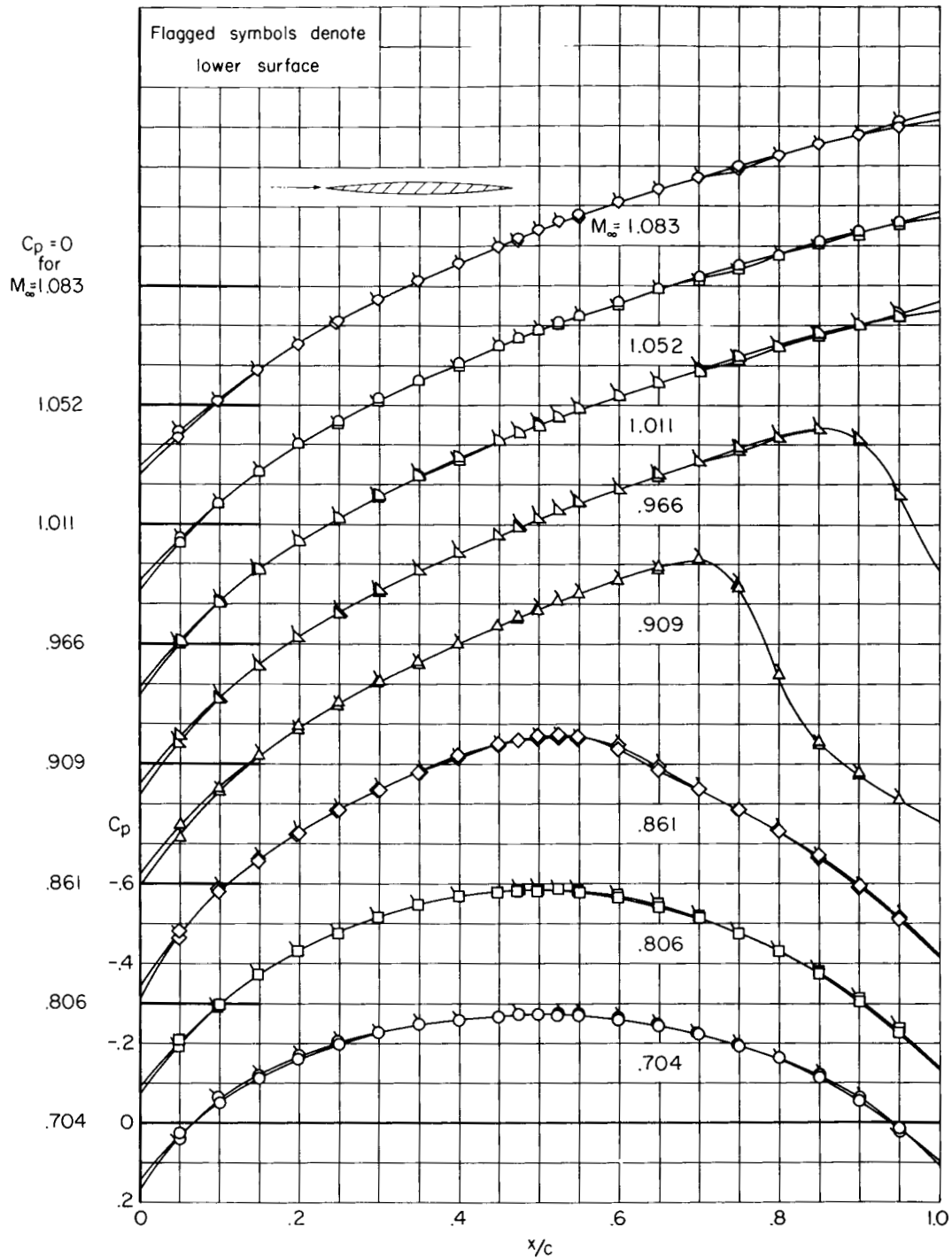
Figure 6.- Continued.





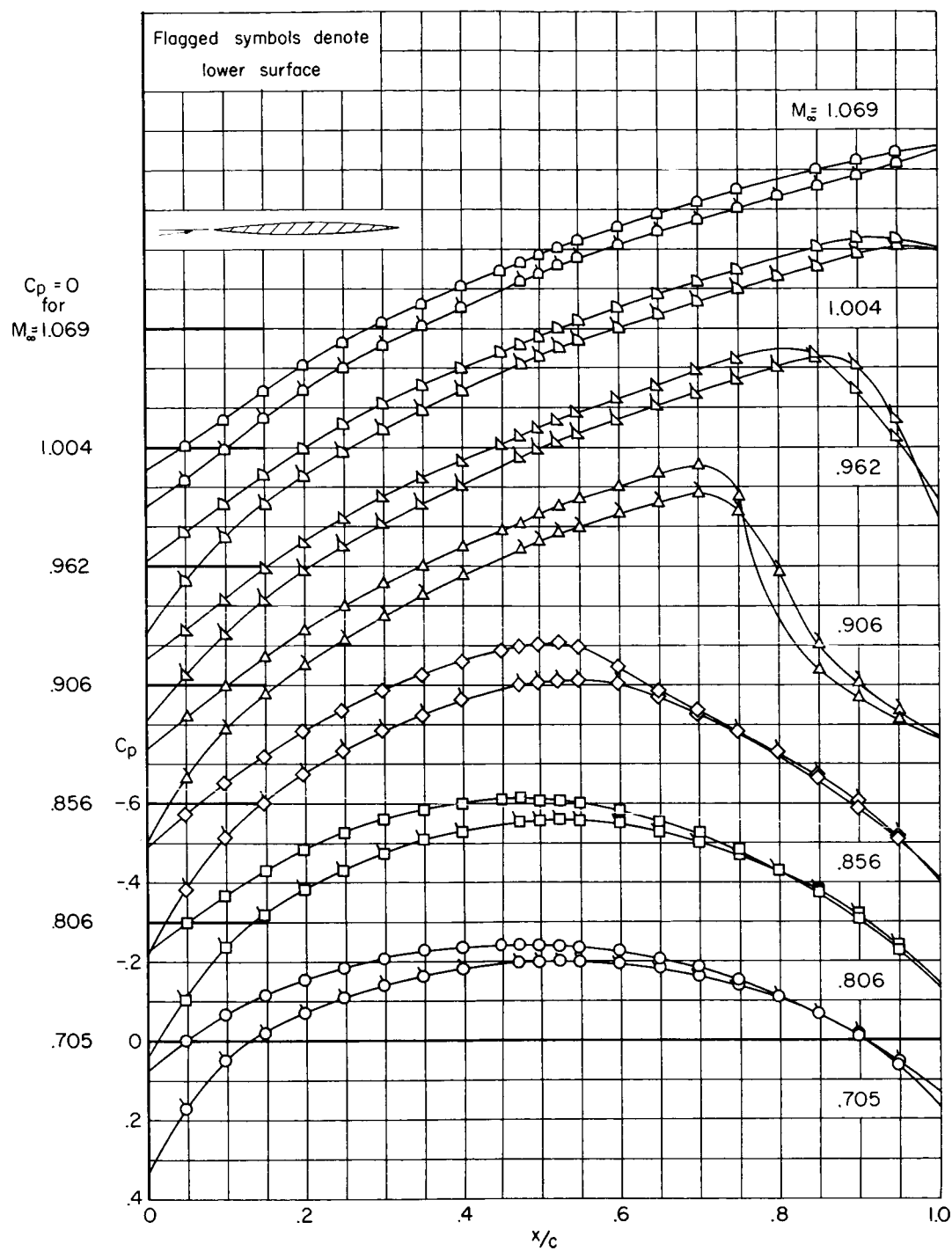
(j)  $\alpha_o = 4^\circ$ ;  $M_\infty = .923$  to  $1.003$

Figure 6.- Concluded.



(a)  $\alpha_o = 0^\circ$ ;  $M_\infty = .704$  to 1.083

Figure 7.- Representative pressure distributions for 6-percent-thick circular-arc airfoil with roughness elements near the leading edge.



(b)  $\alpha_o = 5^\circ$ ;  $M_\infty = .705$  to 1.069

Figure 7.- Continued.

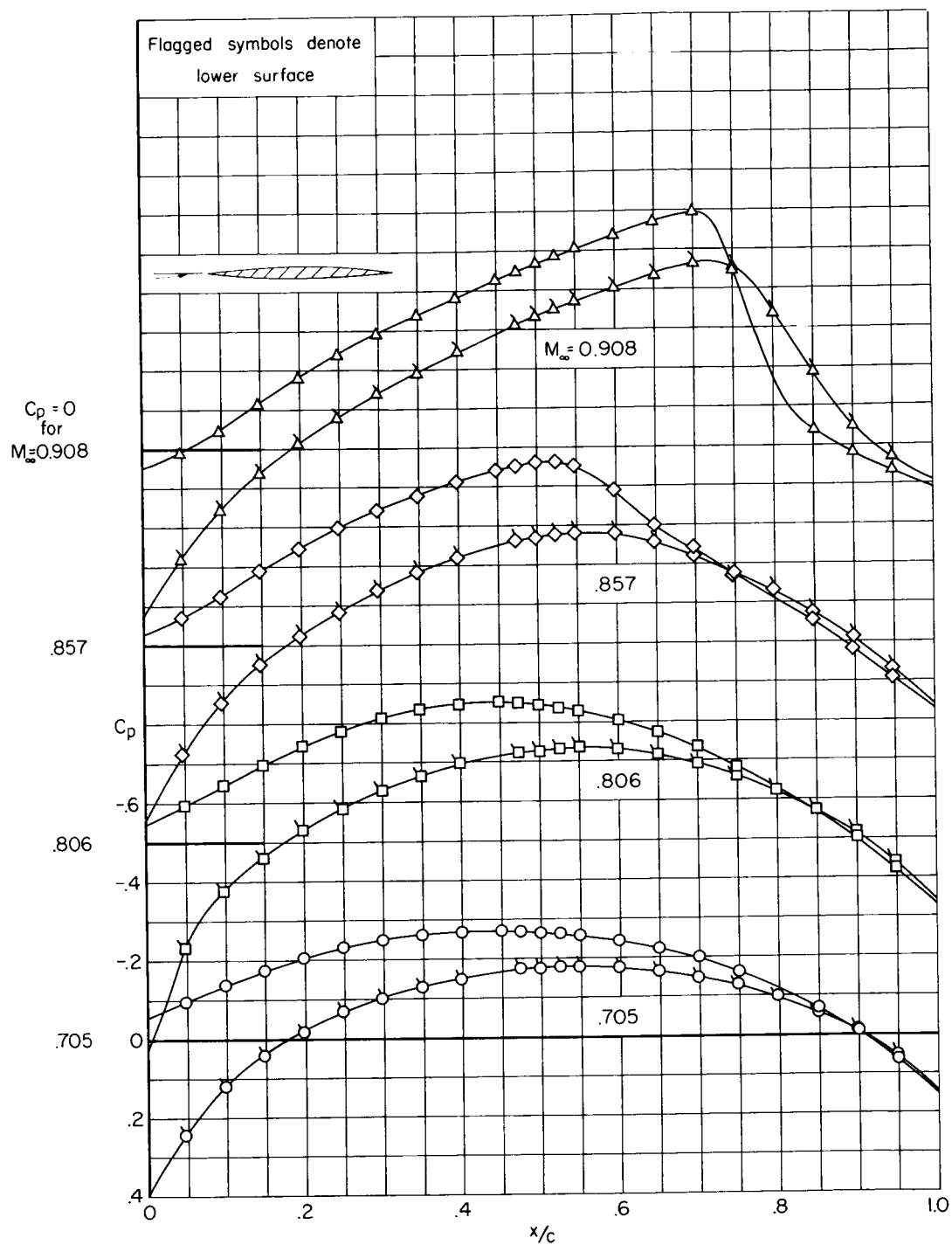
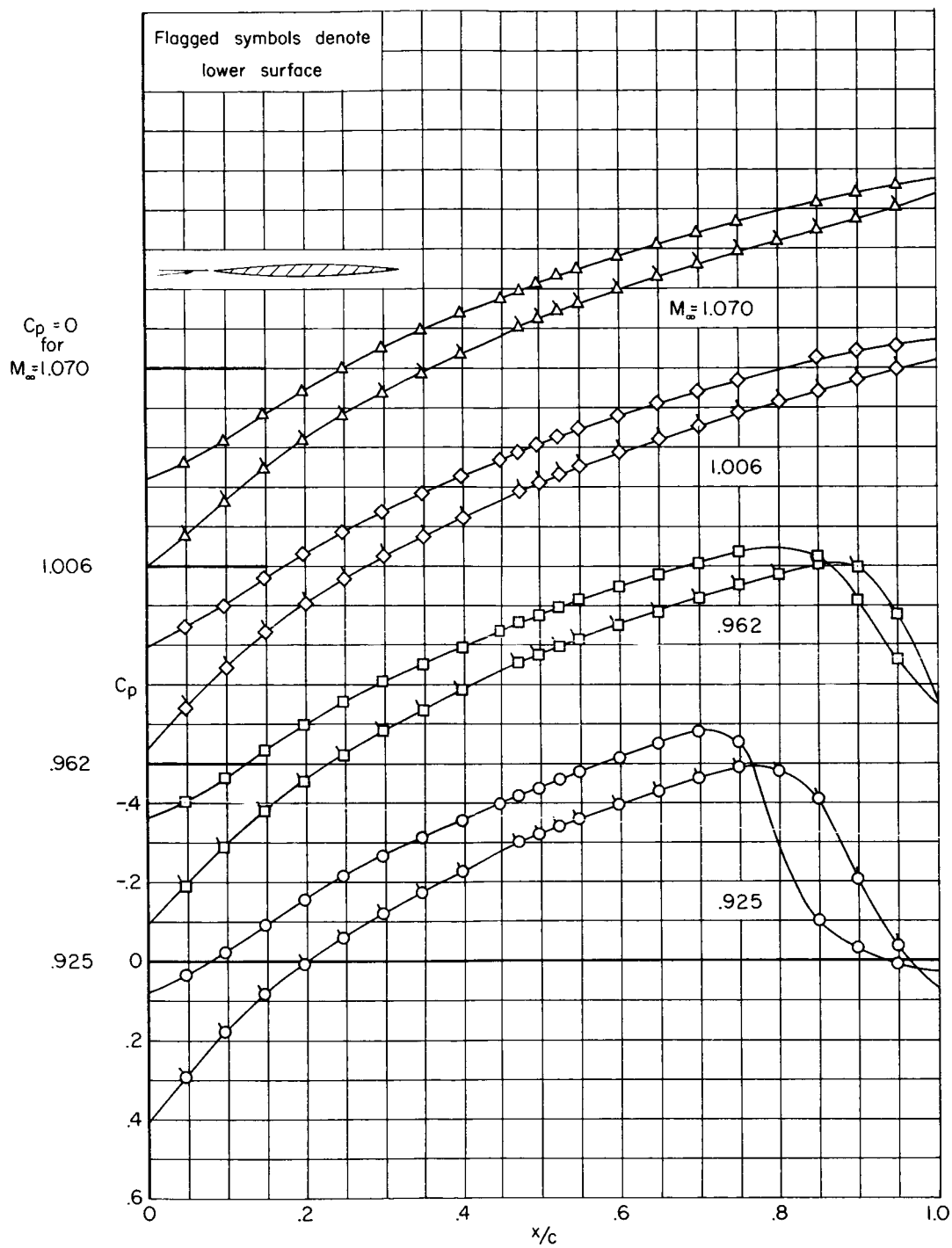
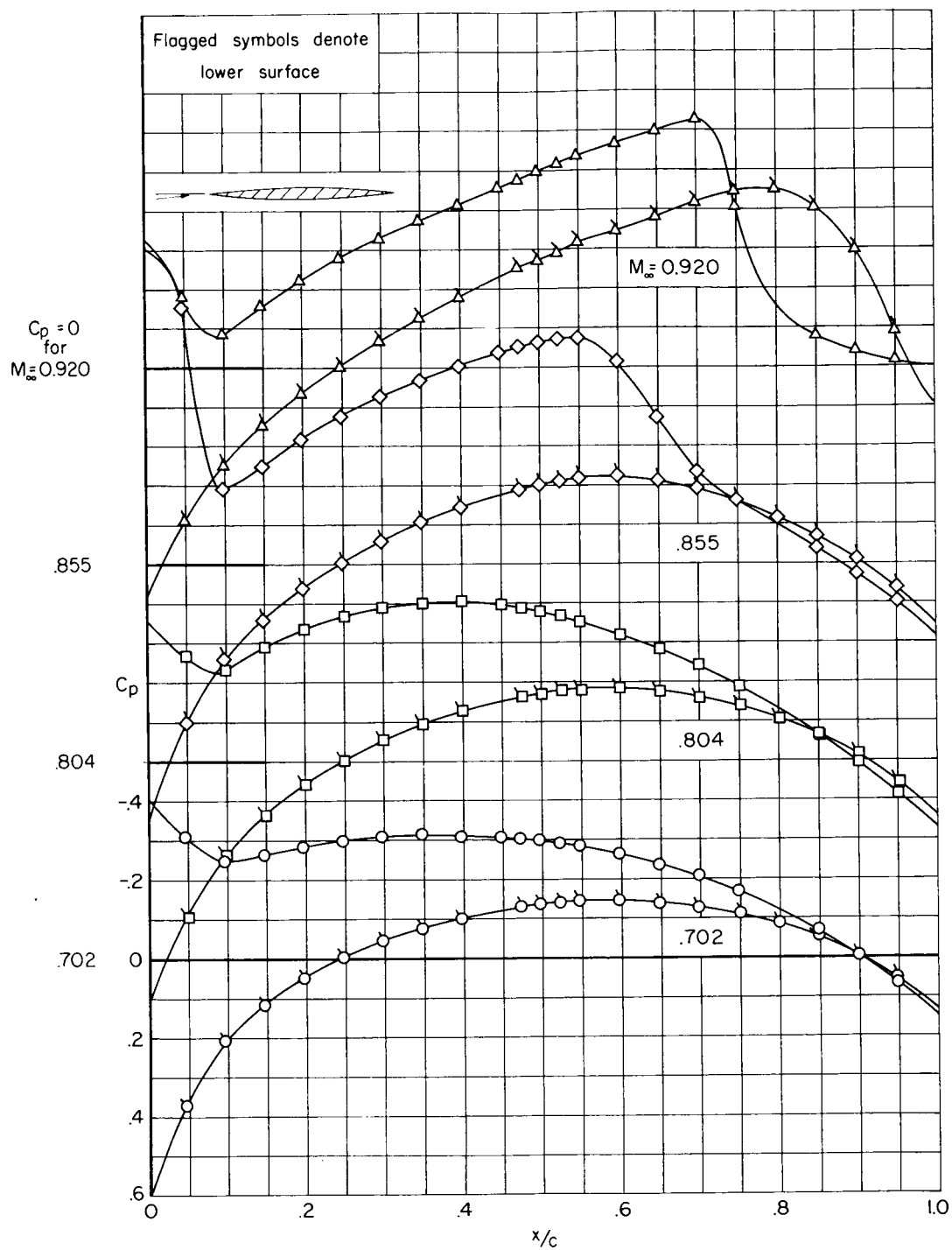


Figure 7.- Continued.



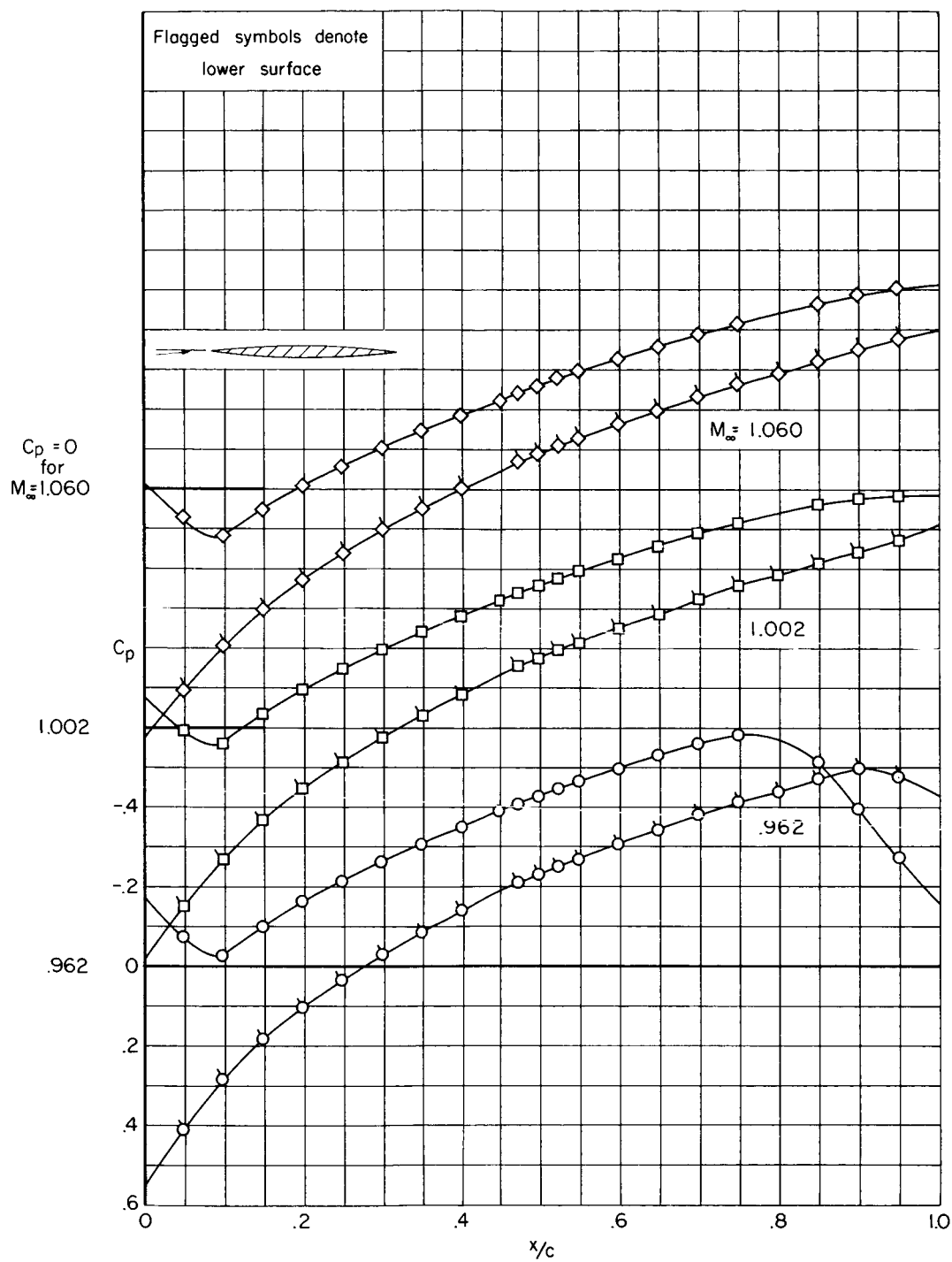
(d)  $\alpha_o = 1^\circ$ ;  $M_\infty = .925$  to 1.070

Figure 7.- Continued.



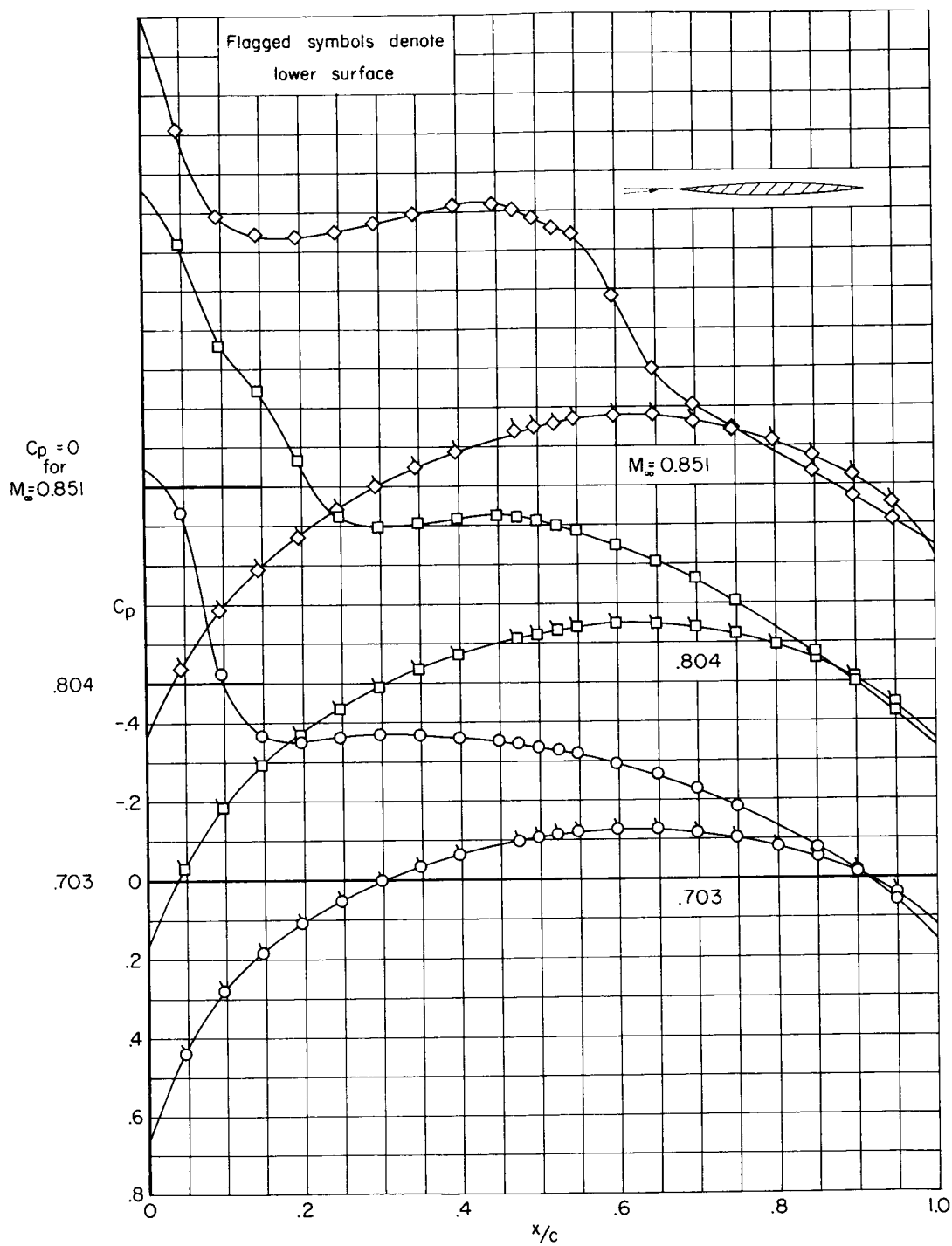
(e)  $\alpha_o = 2^\circ$ ;  $M_\infty = .702$  to  $.920$

Figure 7.- Continued.



(f)  $\alpha_o = 2^\circ$ ;  $M_\infty = .962$  to  $1.060$

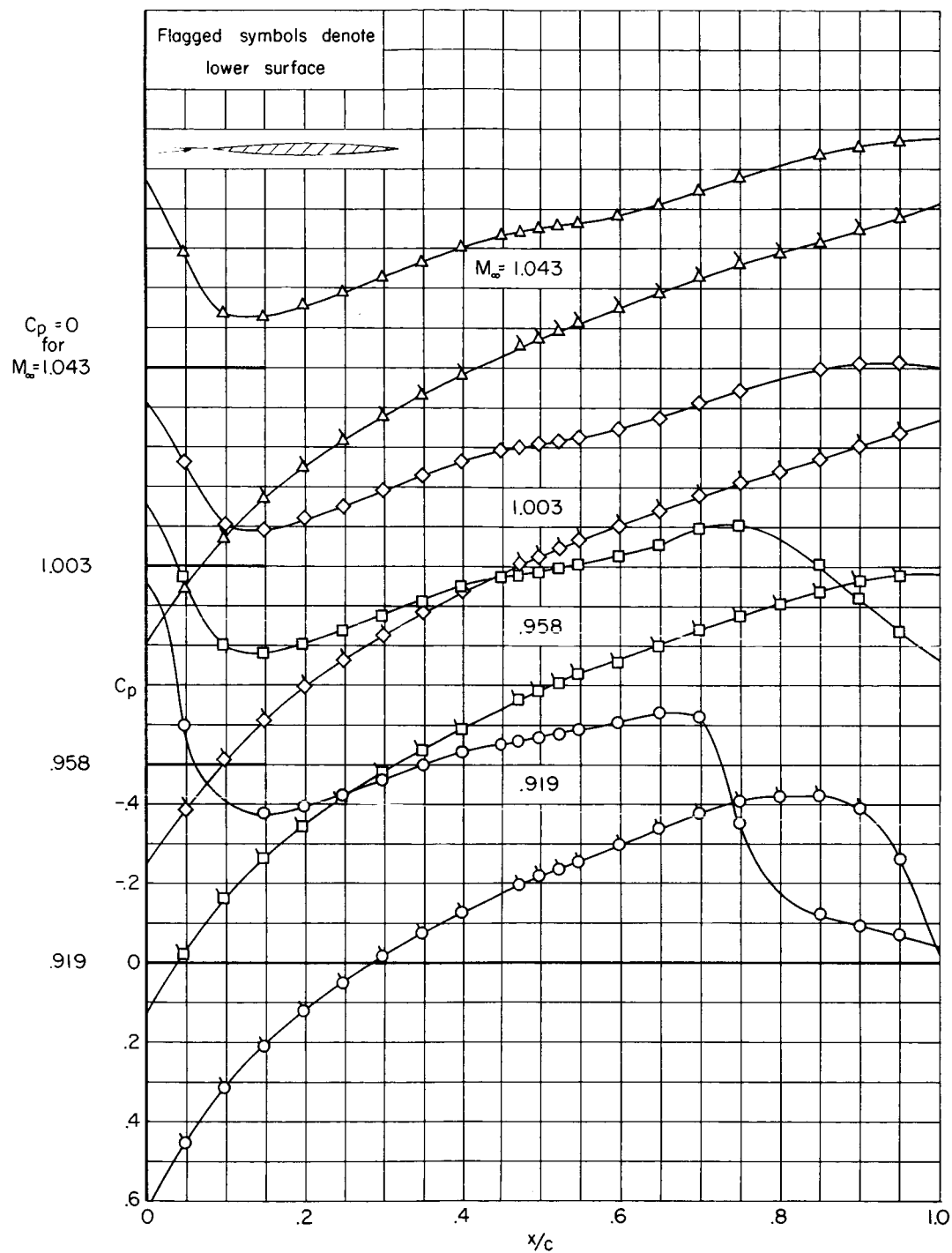
Figure 7.- Continued.



(g)  $\alpha_o = 3^\circ$ ;  $M_\infty = .703$  to  $.851$

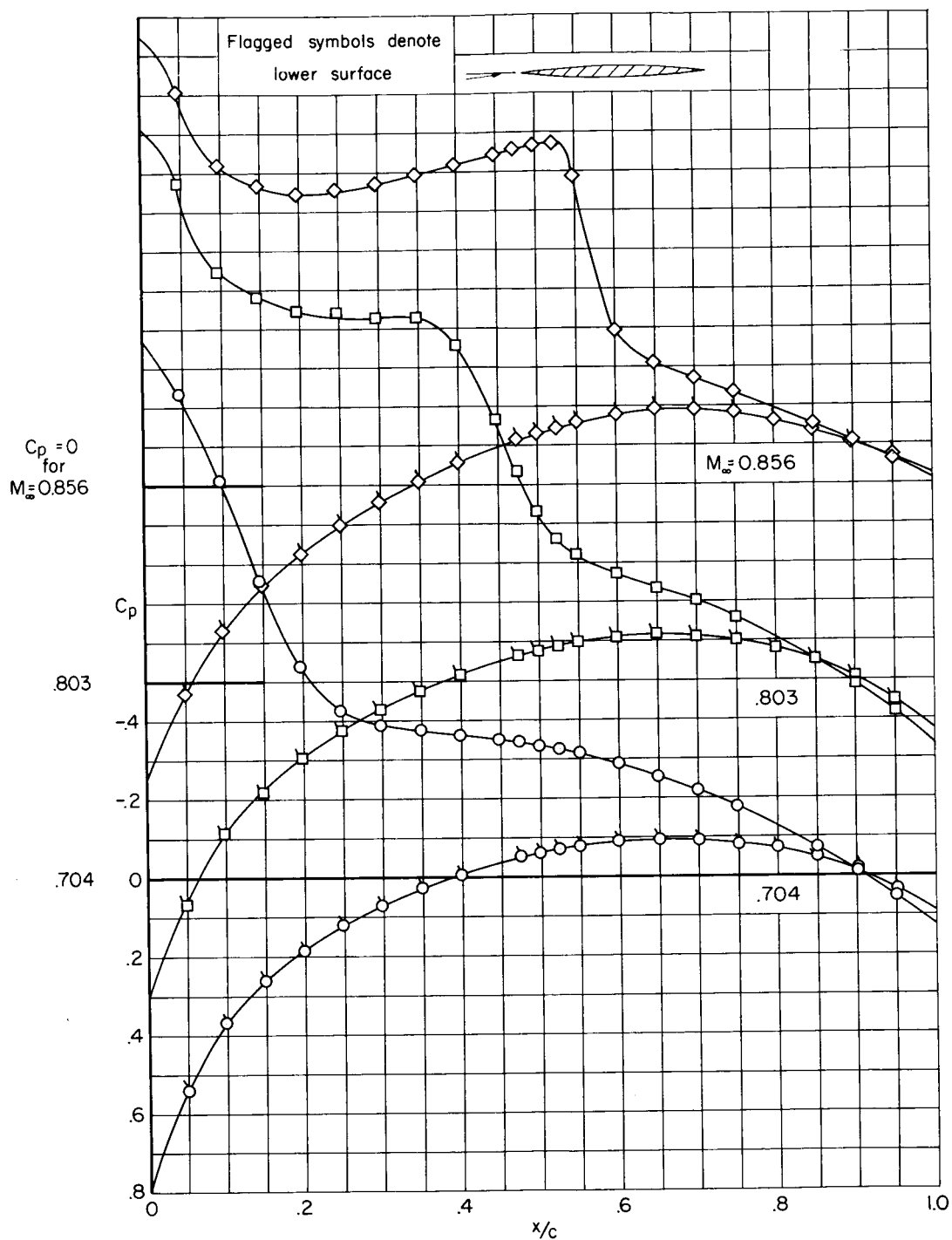
Figure 7.- Continued.





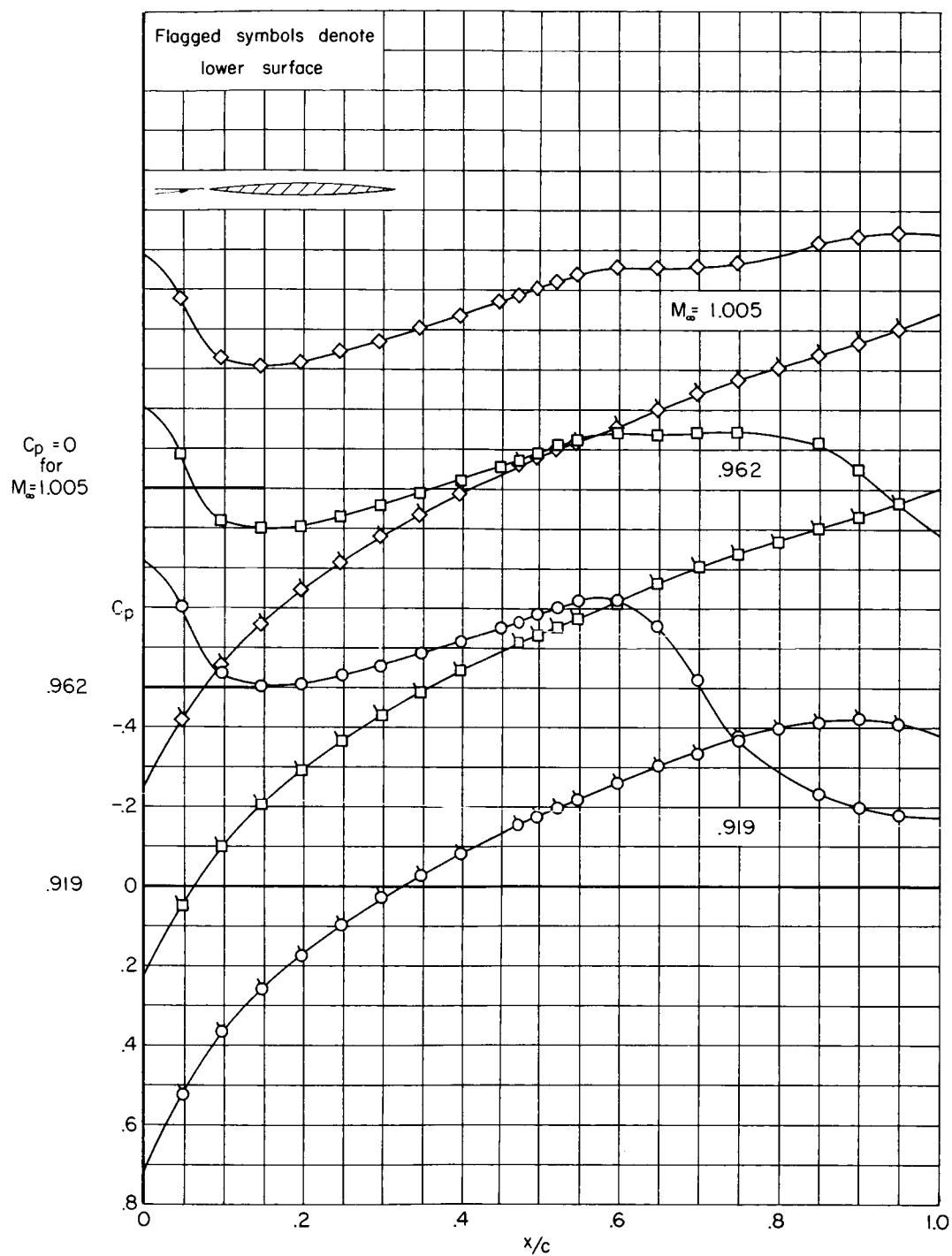
(h)  $\alpha_o = 3^\circ$ ;  $M_\infty = .919$  to 1.043

Figure 7.- Continued.



(i)  $\alpha_o = 4^\circ$ ;  $M_\infty = .704$  to .856

Figure 7.- Continued.



(j)  $\alpha_o = 4^\circ$ ;  $M_\infty = .919$  to  $1.005$

Figure 7.- Concluded.

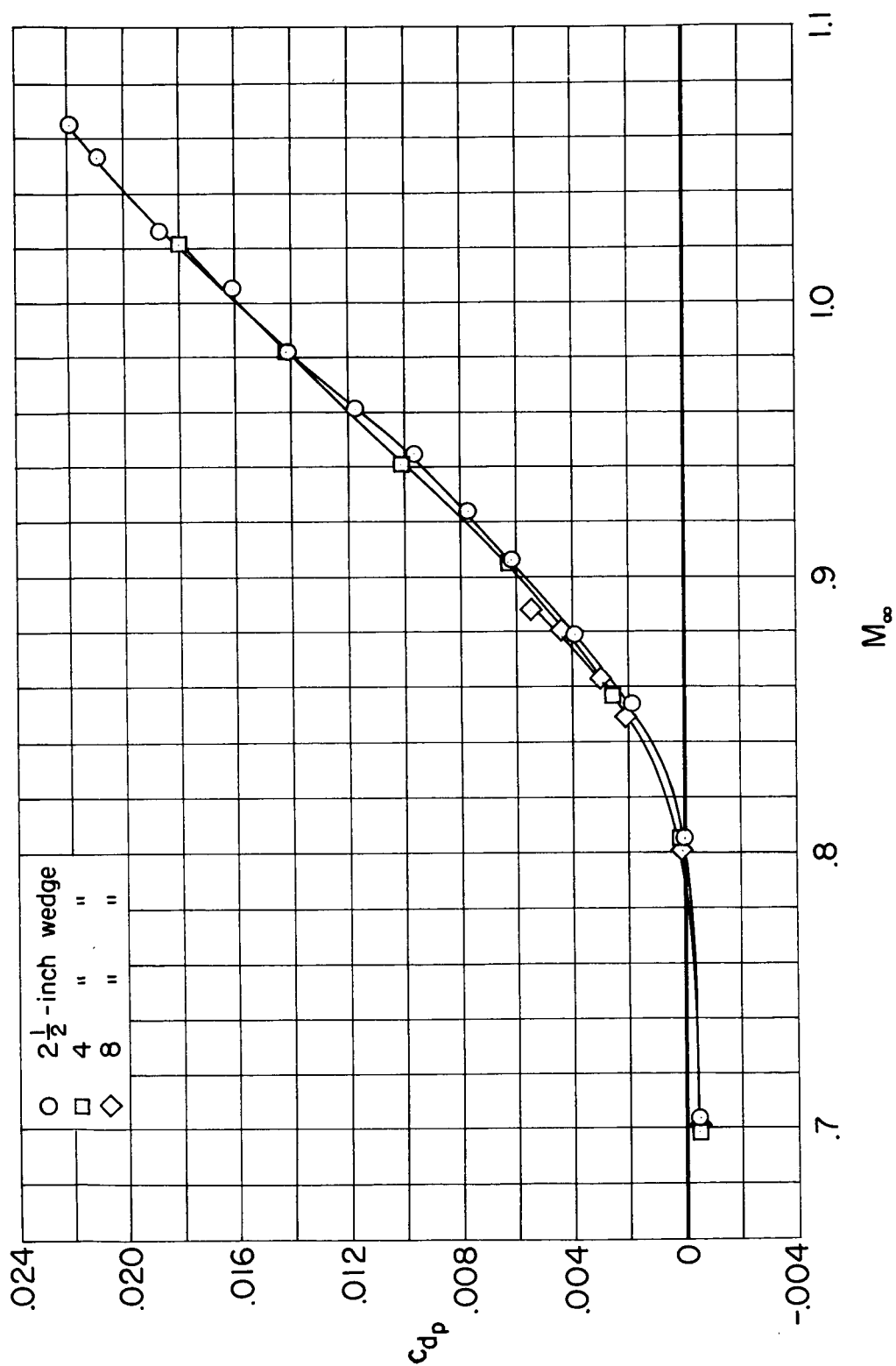


Figure 8.- Variation with Mach number of pressure-drag coefficient at  $\alpha_0 = 0^\circ$  for single wedges with a straight afterbody.

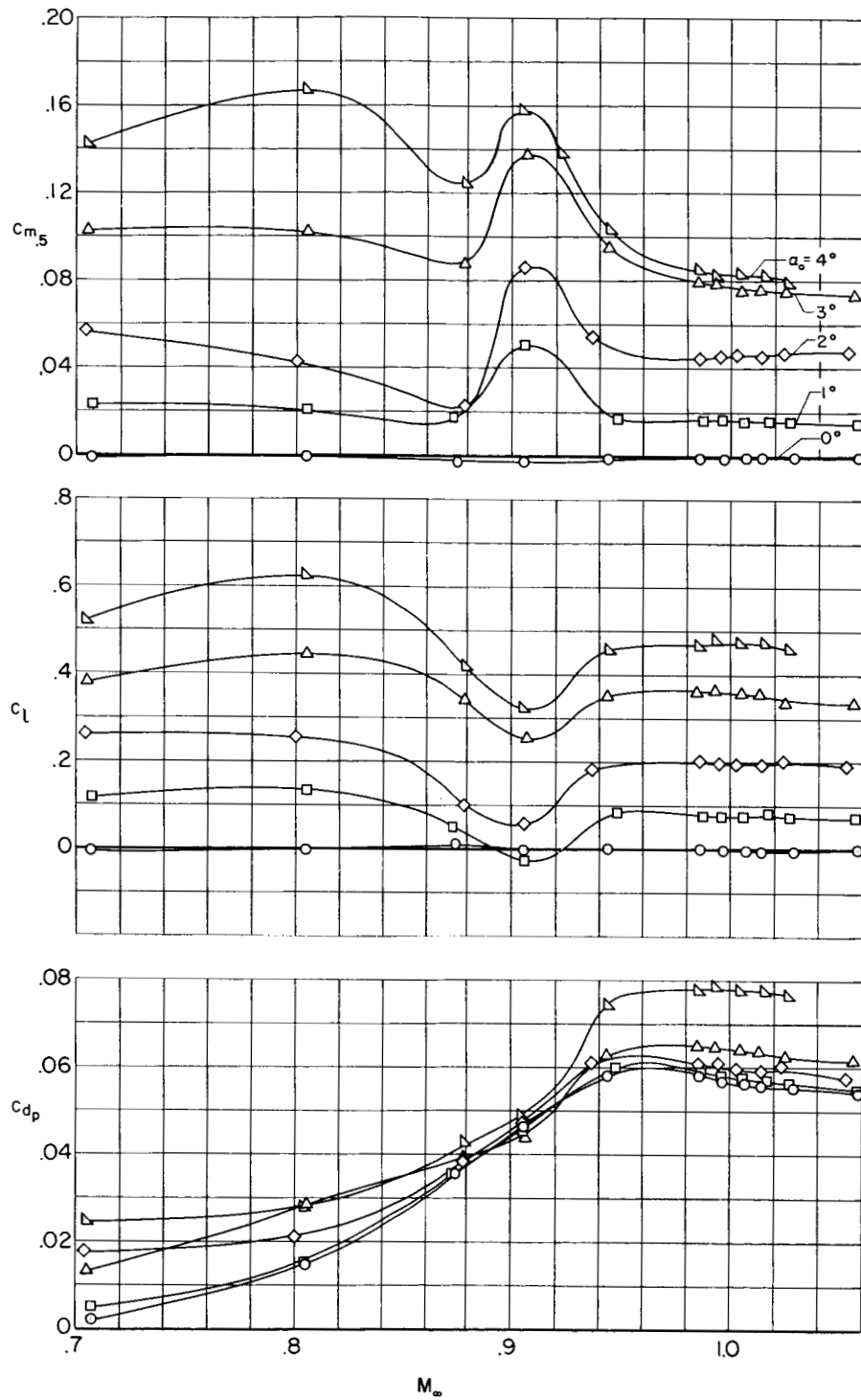
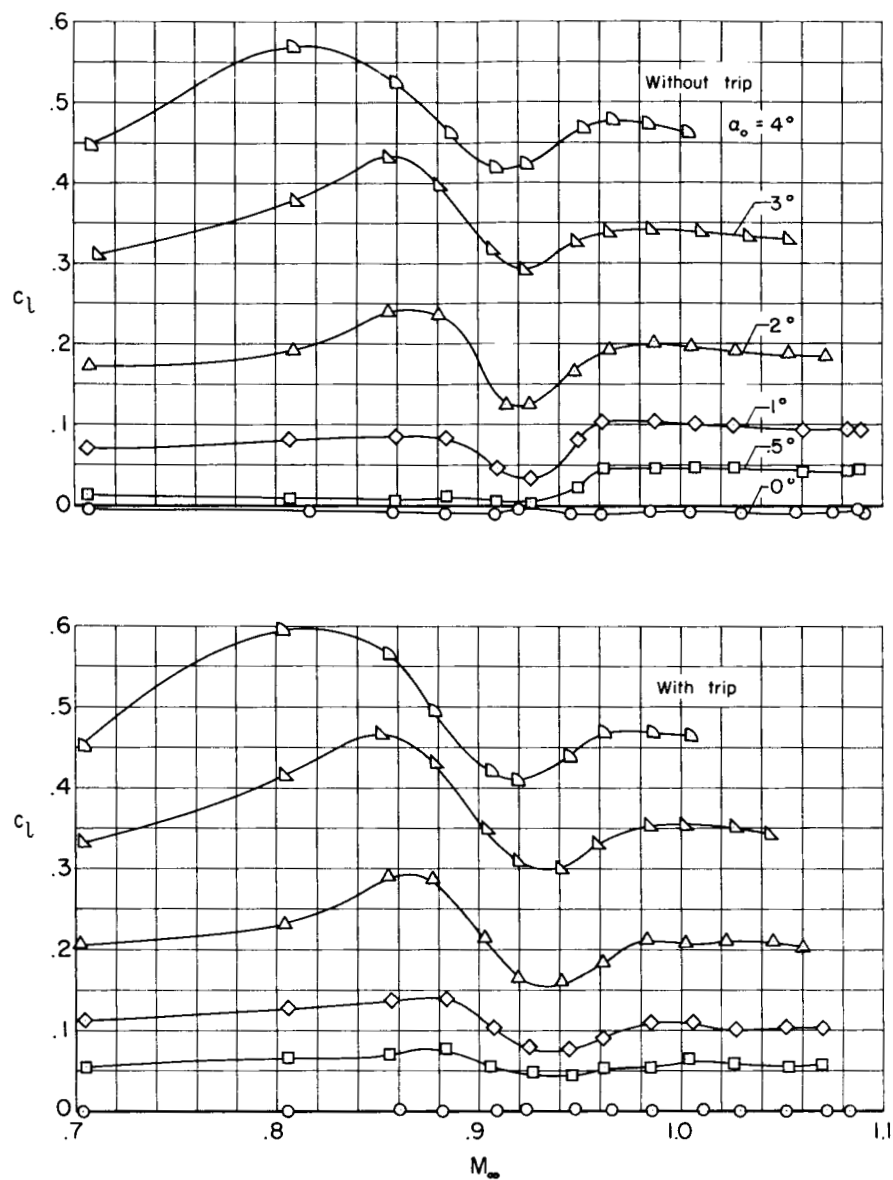
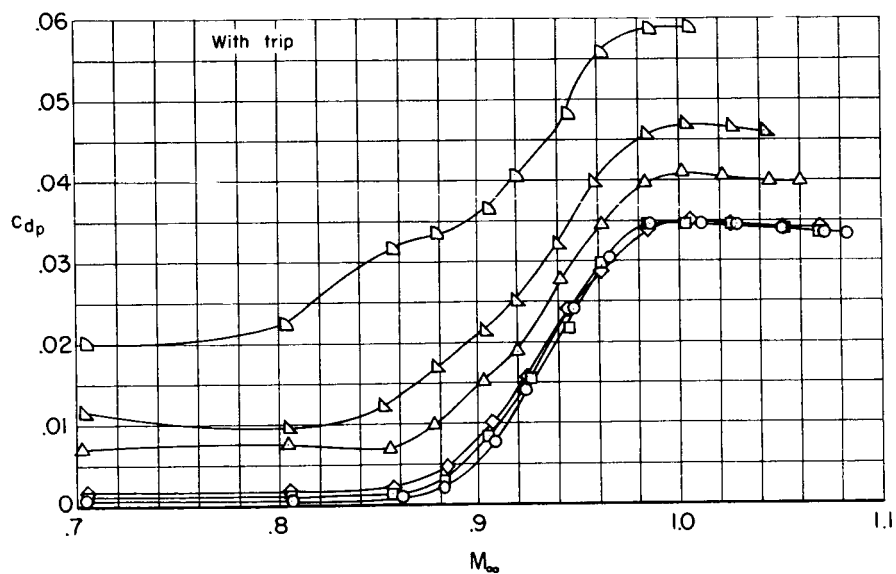
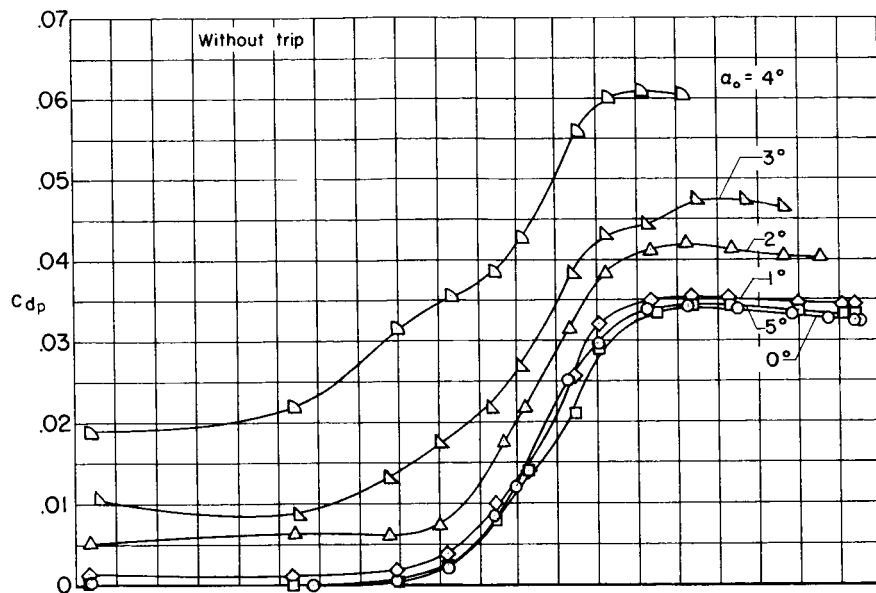


Figure 9.- Variation with Mach number of coefficients of lift, pressure drag, and pitching moment for the double-wedge airfoil.



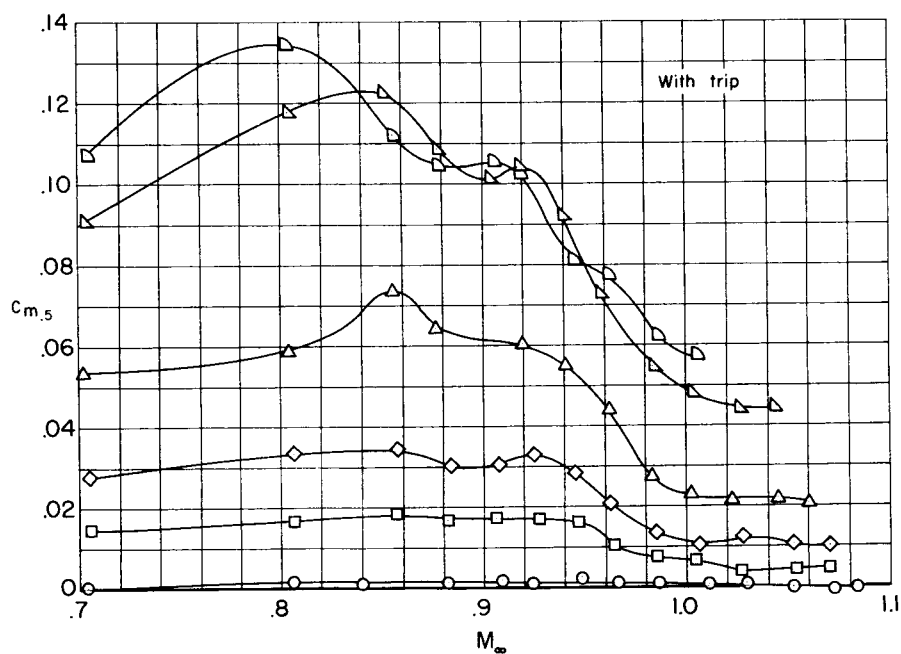
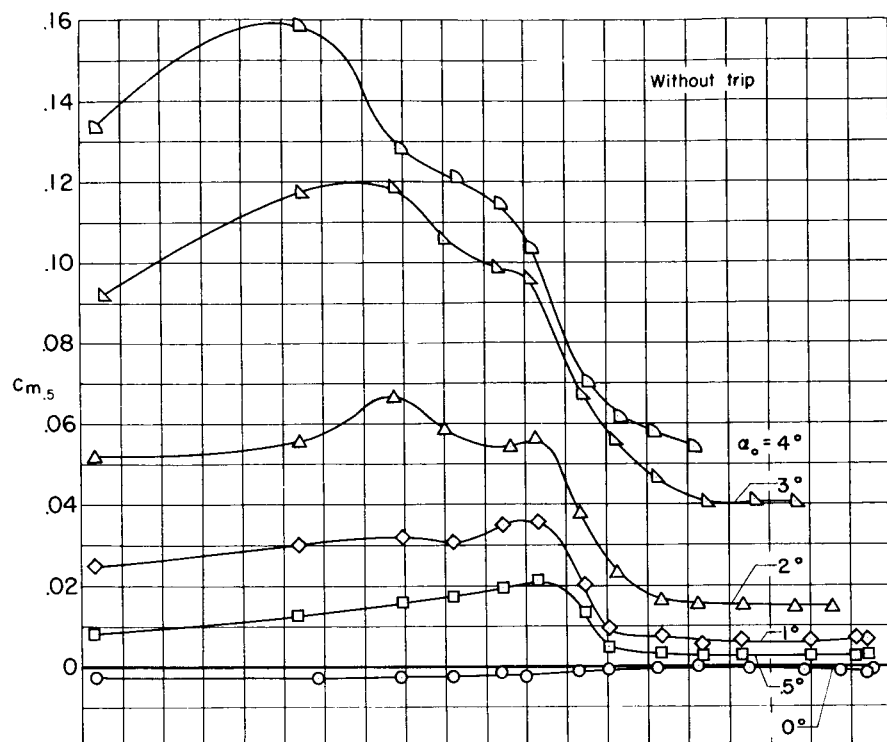
(a) Lift coefficient.

Figure 10.- Aerodynamic characteristics of circular-arc airfoil with and without roughness element.



(b) Pressure-drag coefficient.

Figure 10.- Continued.



(c) Pitching-moment coefficient.

Figure 10.- Concluded.



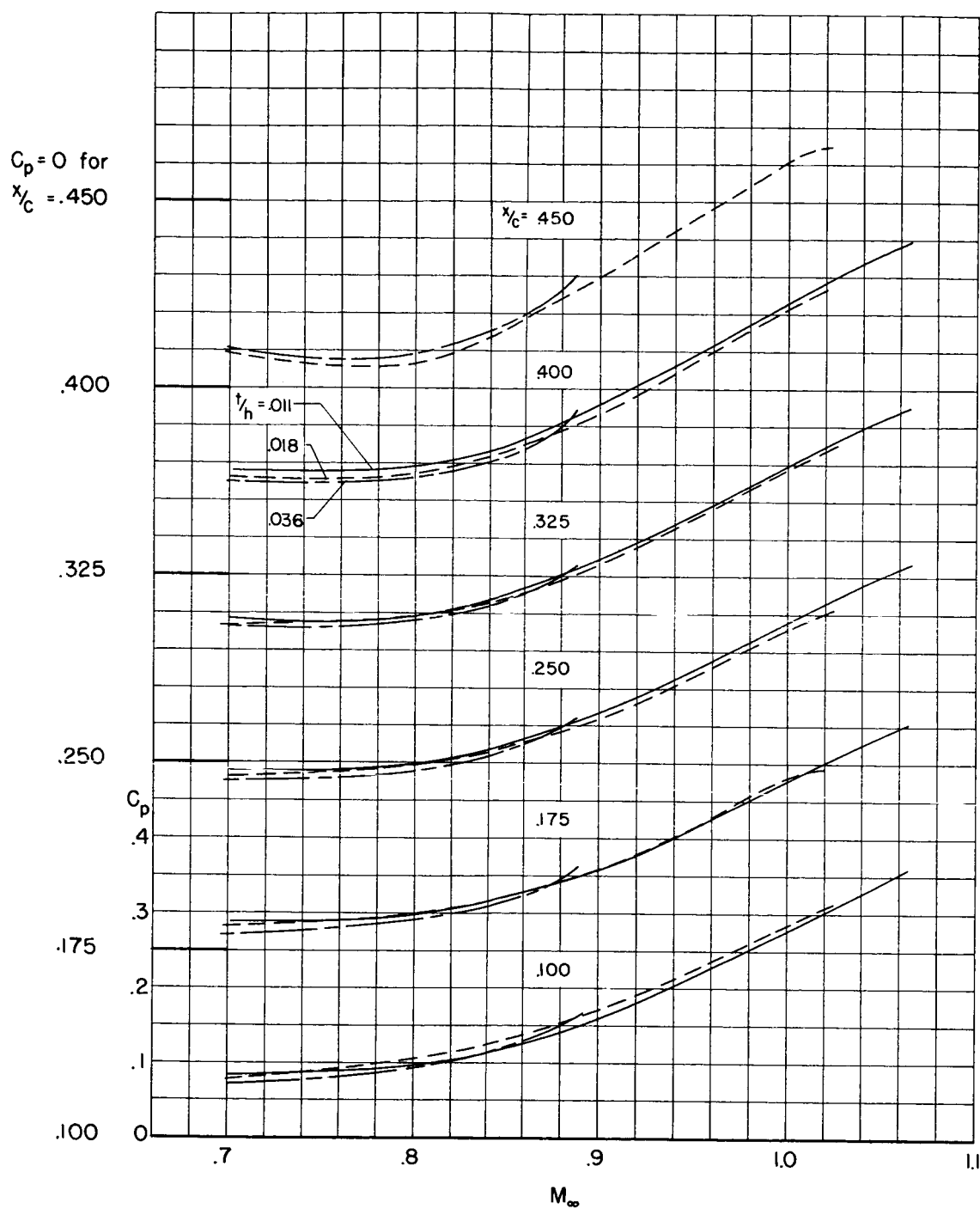


Figure 11.- Variation with Mach number of pressure coefficient at various chordwise stations for three sizes of single wedge with afterbody.

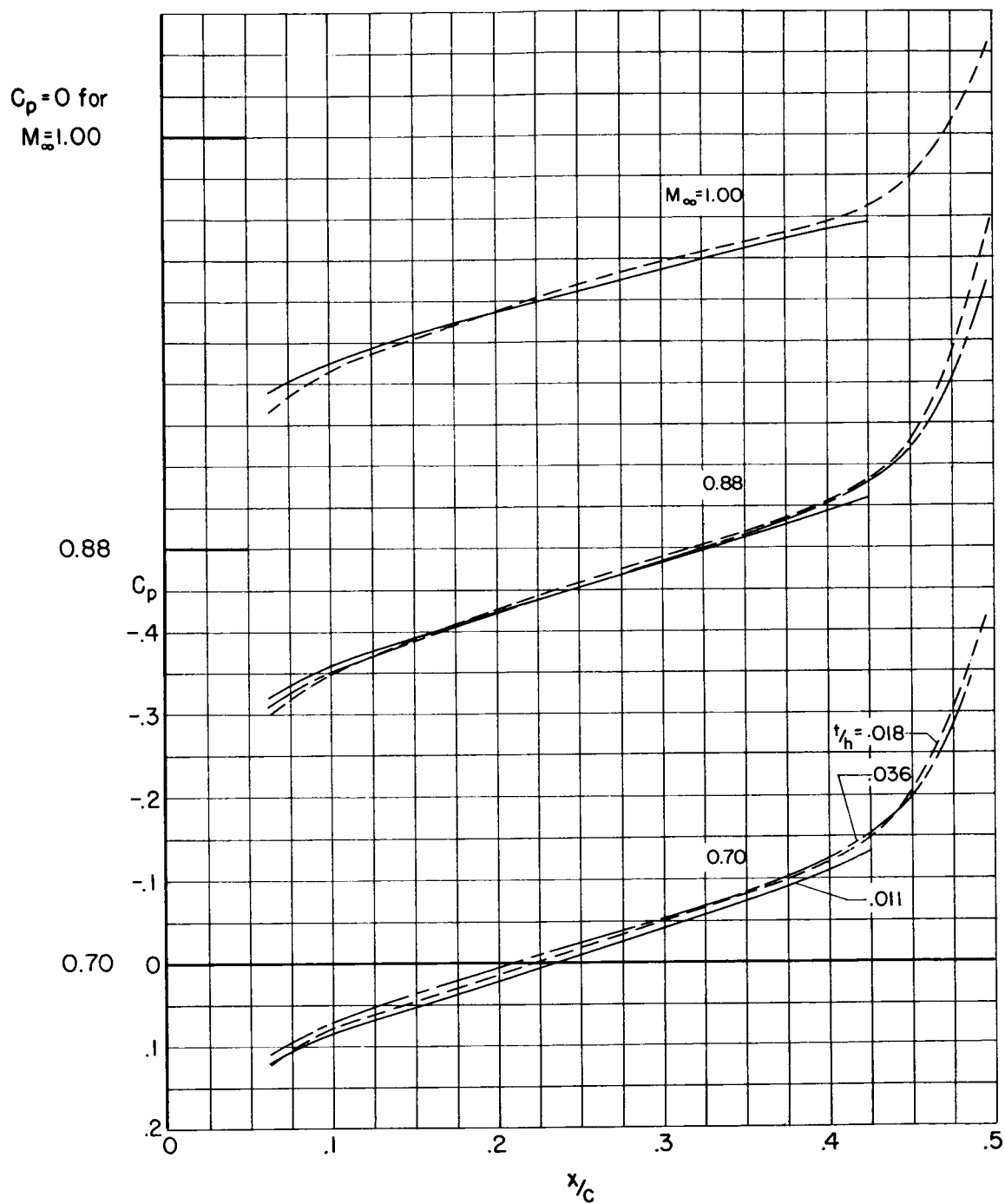


Figure 12.- Effect of model size on pressure distributions of wedge airfoil with afterbody at  $\alpha_0 = 0^\circ$  for three Mach numbers.

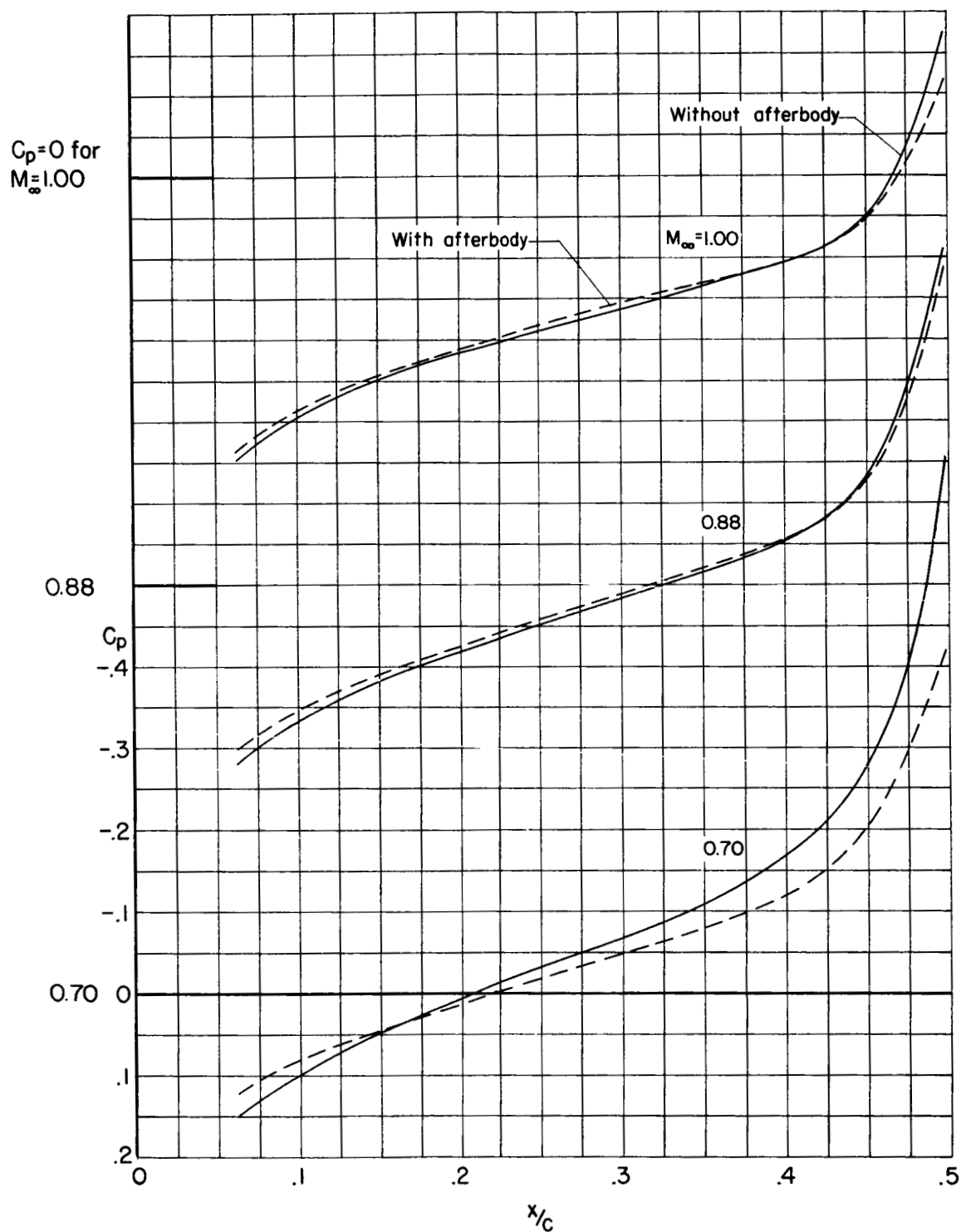


Figure 13.- Effect of straight afterbody on pressure distribution of 4-inch wedge at  $\alpha_0 = 0^\circ$  for three Mach numbers.

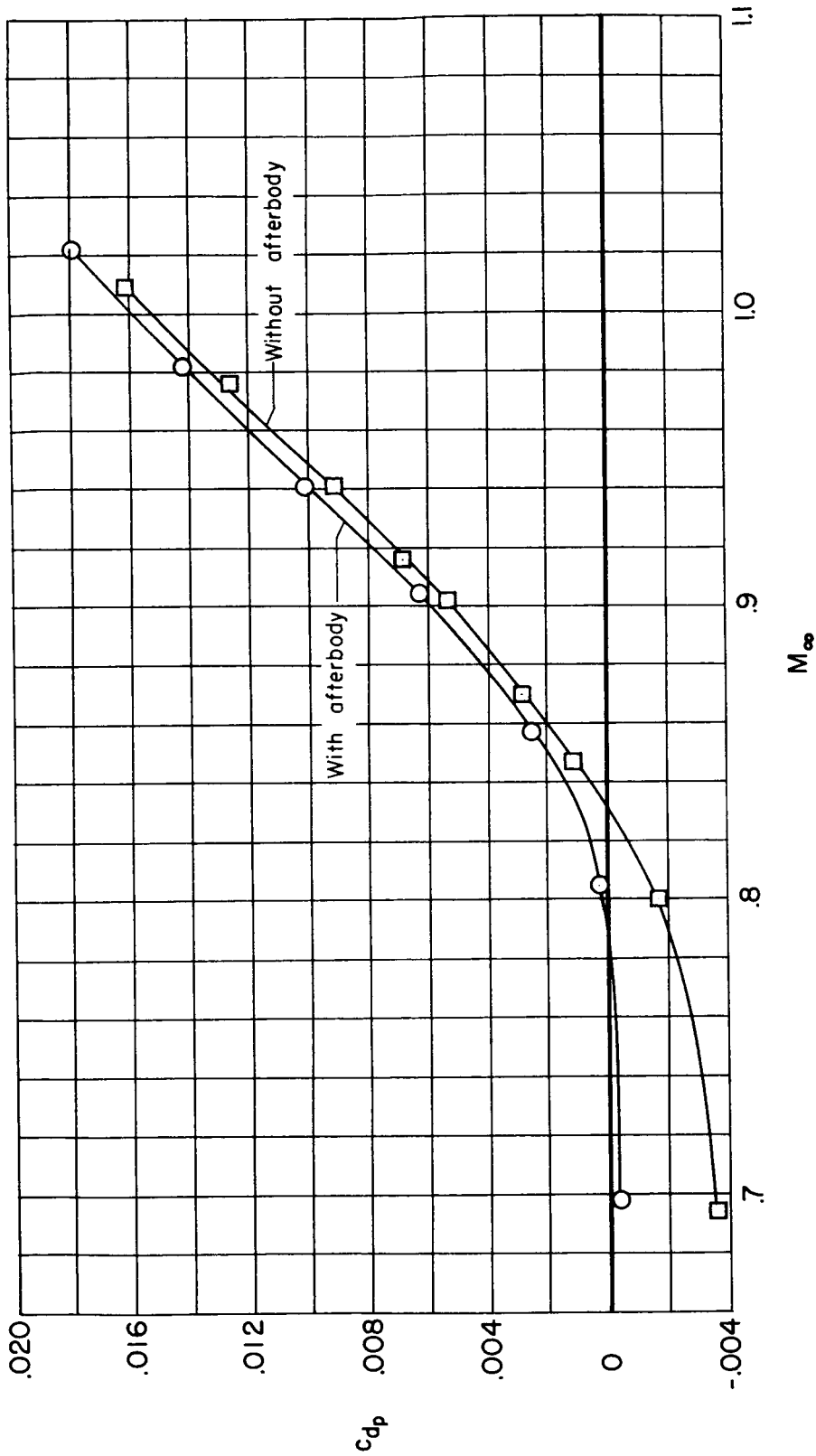


Figure 14.- Variation with Mach number of pressure-drag coefficient at  $\alpha_0 = 0^\circ$  for 4-inch single wedge, with and without afterbody.

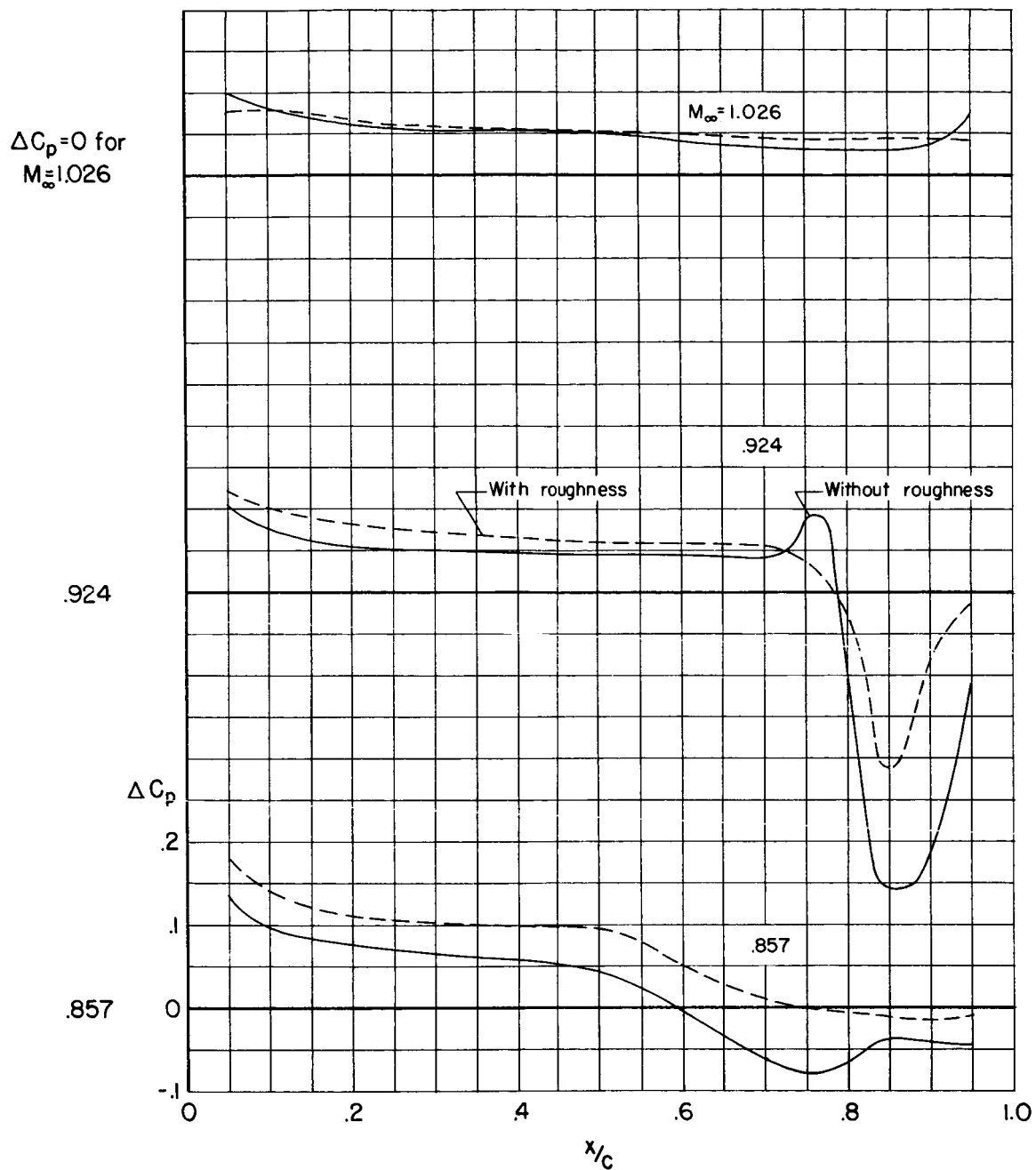


Figure 15.- Effect of boundary-layer trip on aerodynamic loading of the circular-arc airfoil at  $\alpha_0 = 0.5^\circ$  for three Mach numbers.

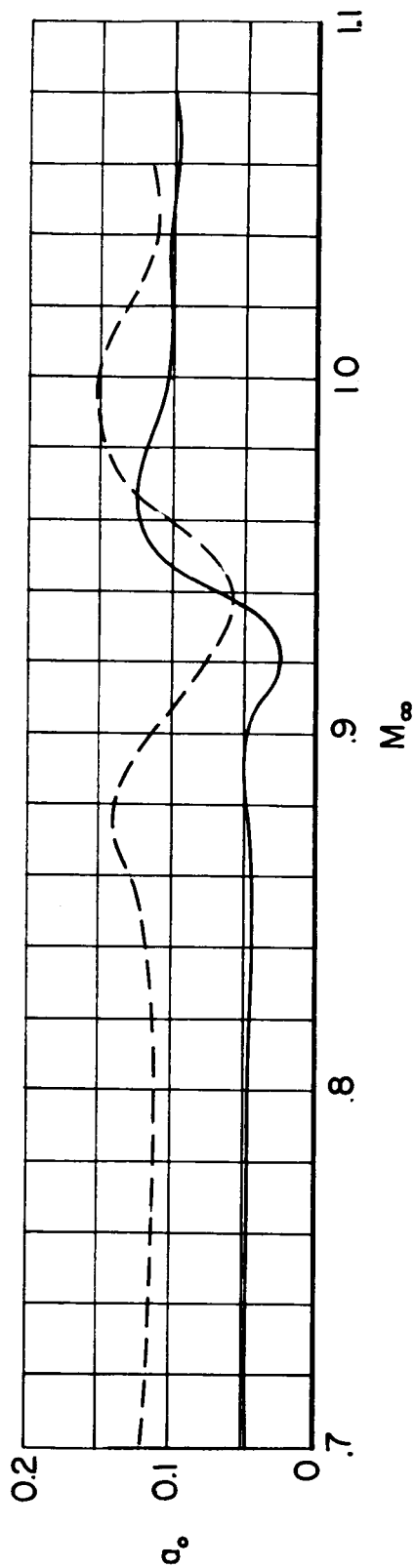
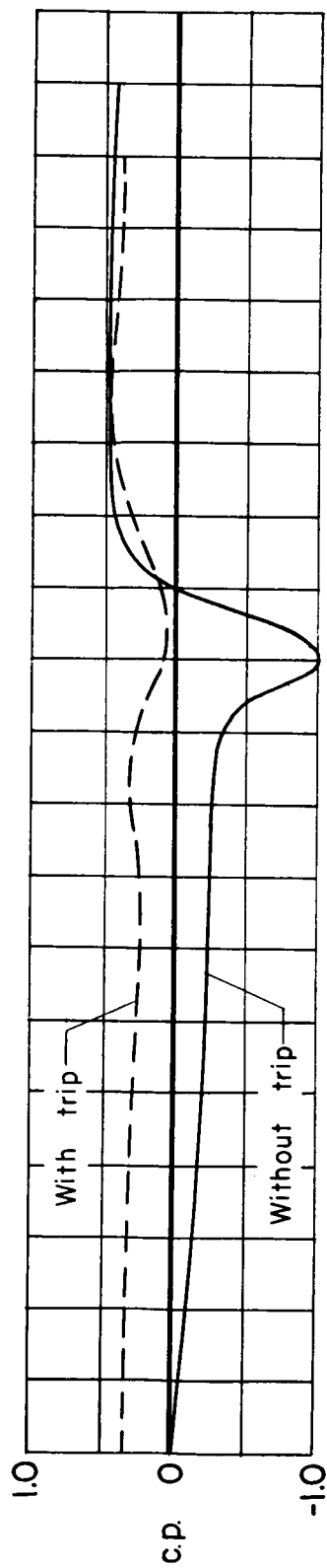
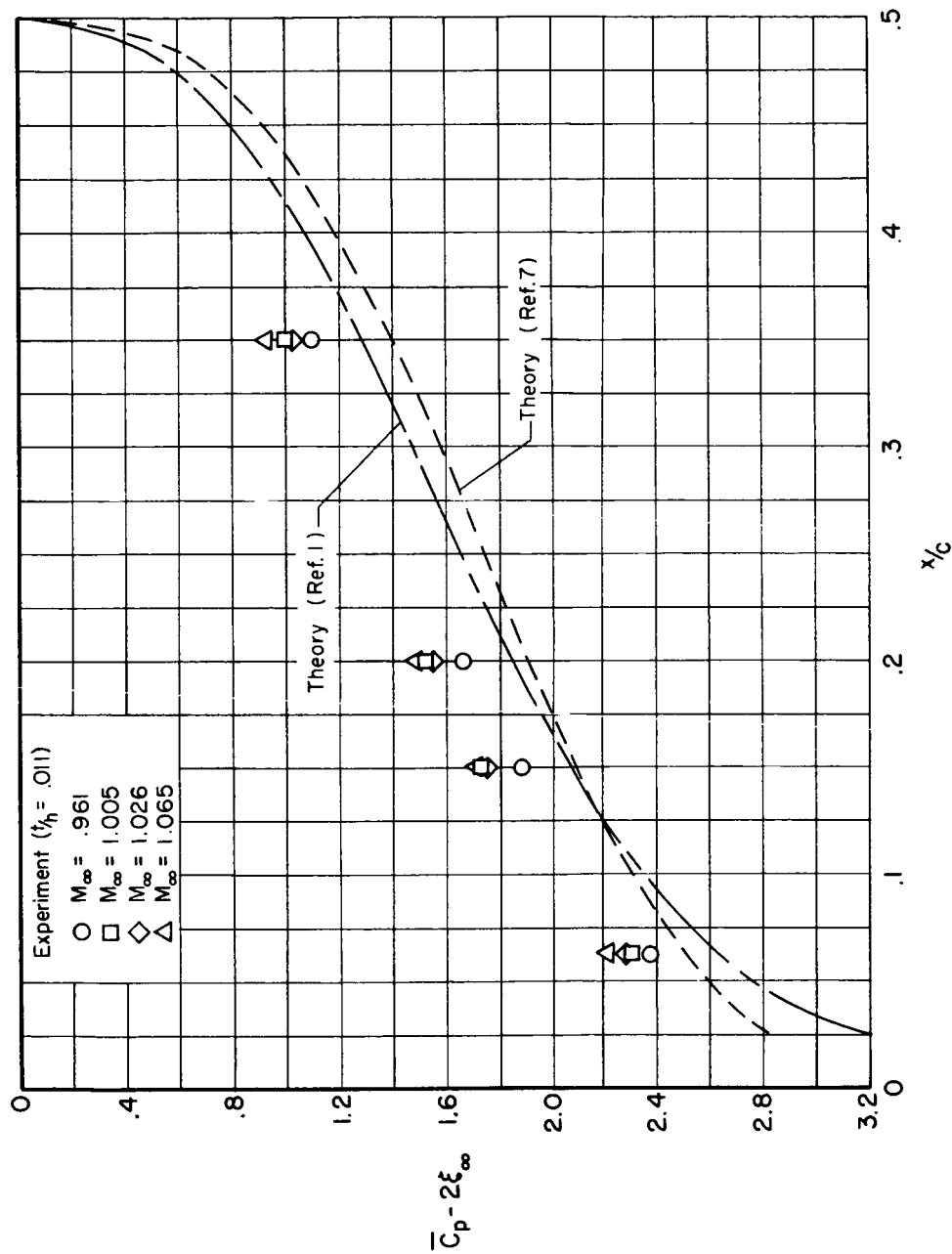
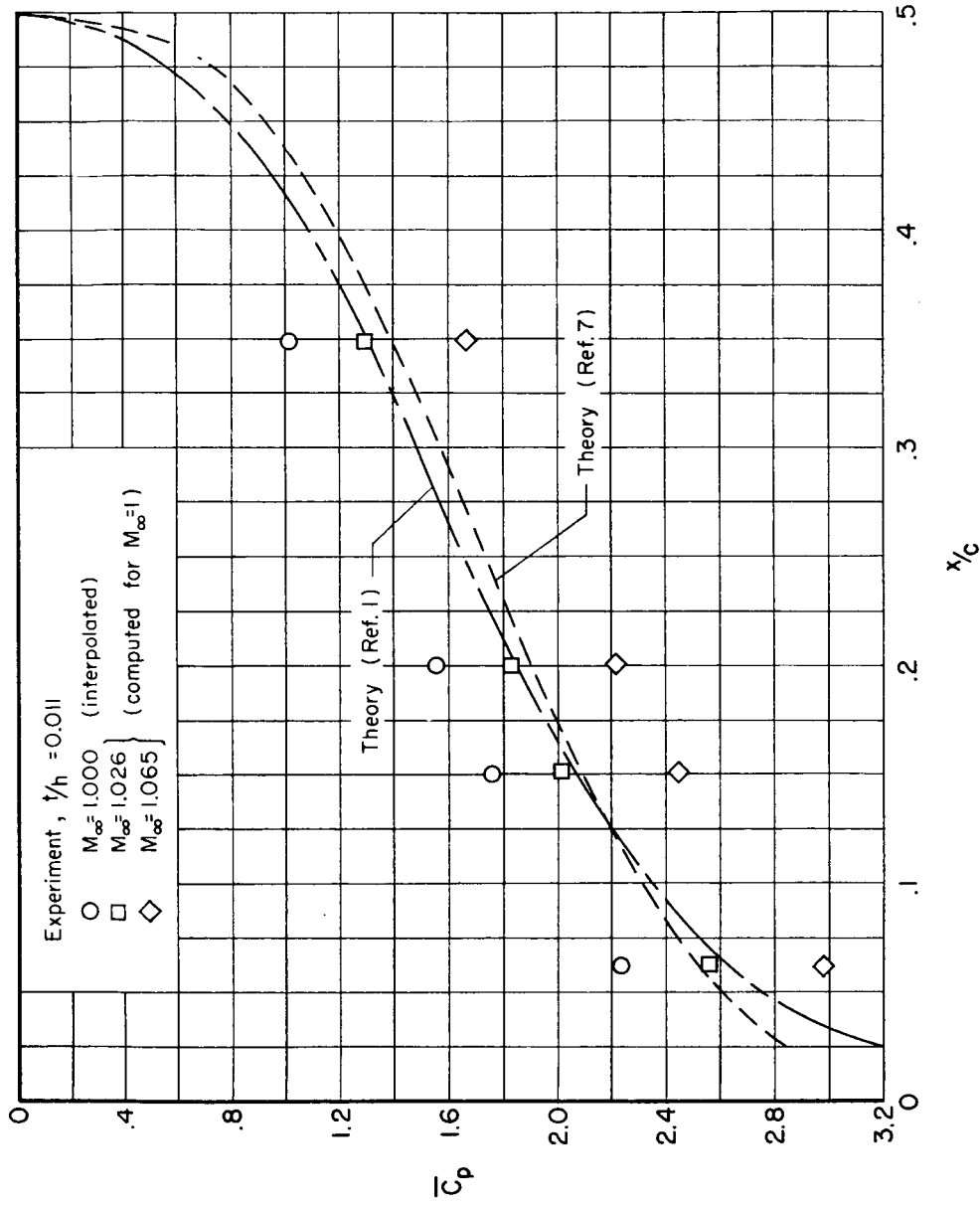


Figure 16.- Effect of boundary-layer trip on the variation with Mach number of lift-curve slope and center of pressure of the circular-arc airfoil at  $\alpha_0 = 0^\circ$ .



(a) Effect of free stream speed.

Figure 17.- Transonic similarity pressure distributions for single-wedge airfoil at  $\alpha_0 = 0^\circ$ .



(b) Effect of Mach number shifts.

Figure 17.- Concluded.



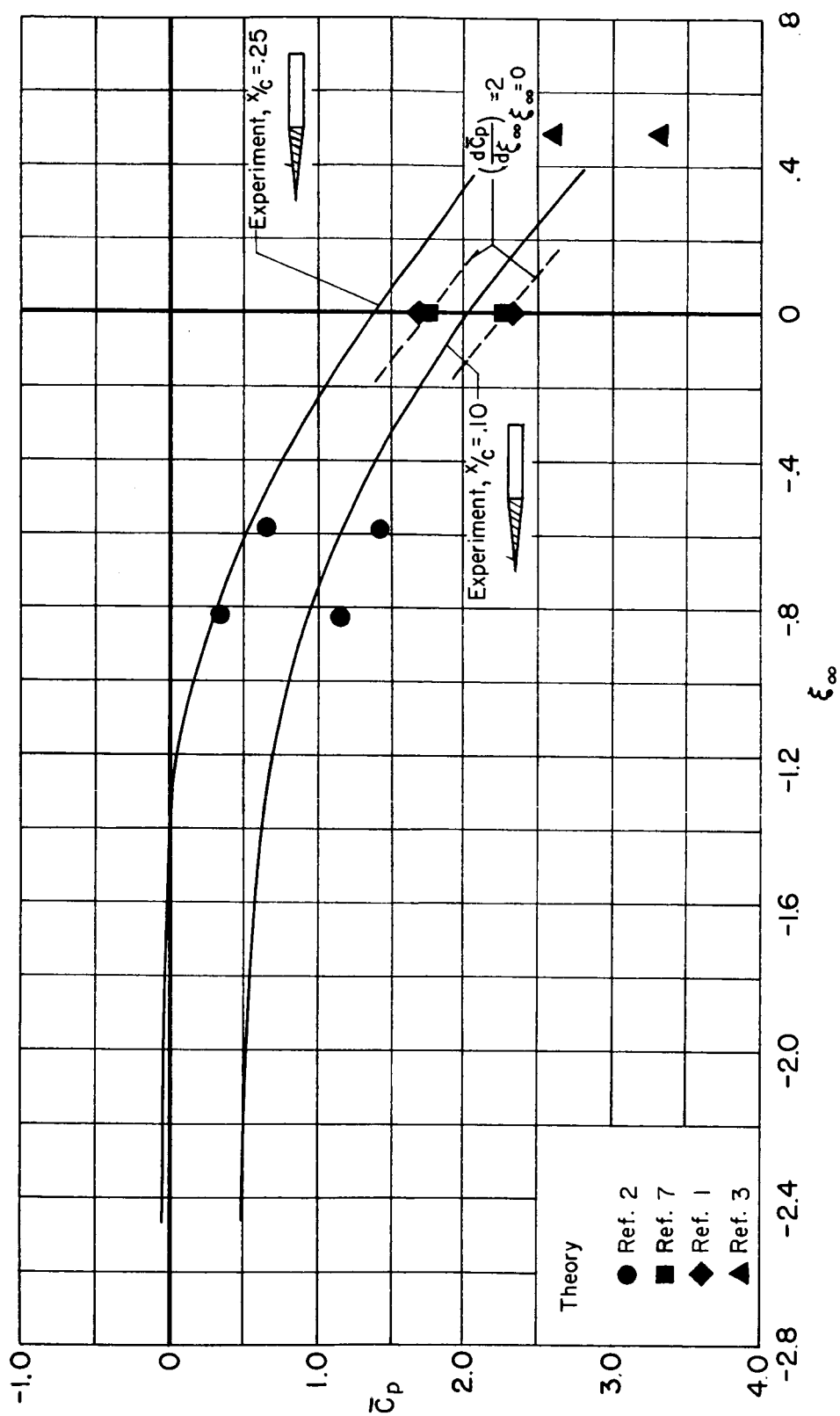


Figure 18.- Variation with  $\xi_\infty$  of  $\bar{C}_p$  for 2-l/2-inch single wedge at two chordwise stations.

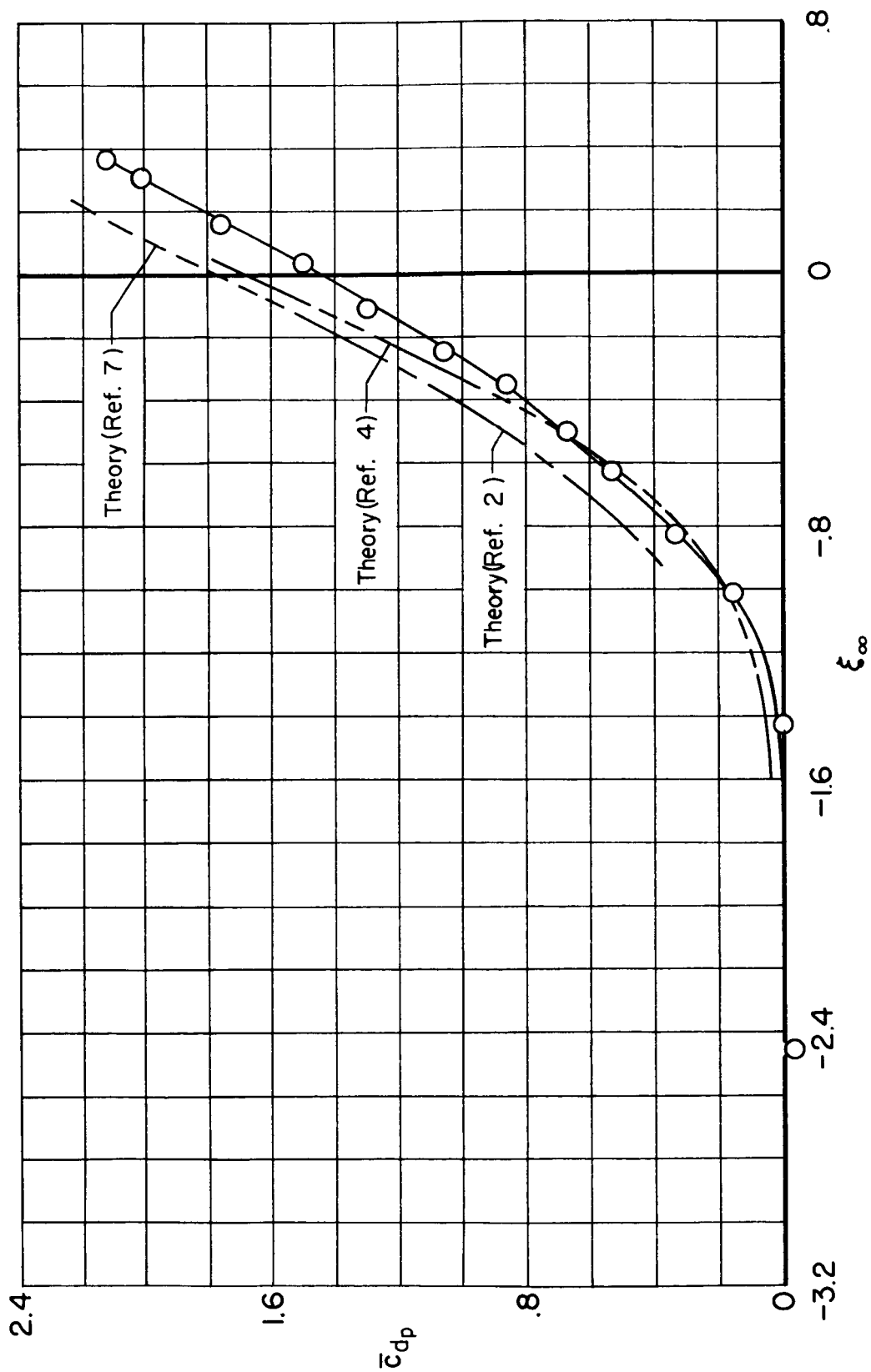
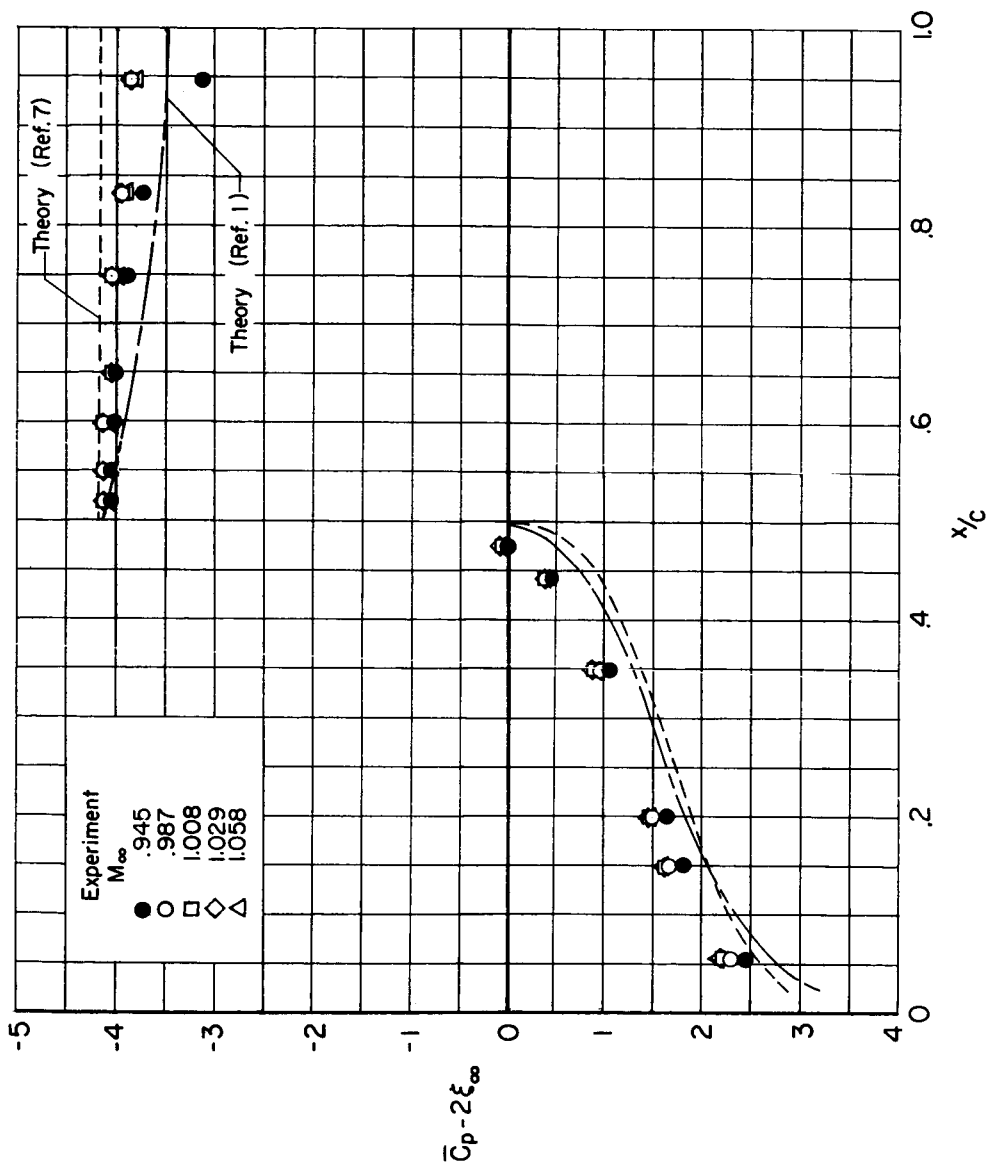
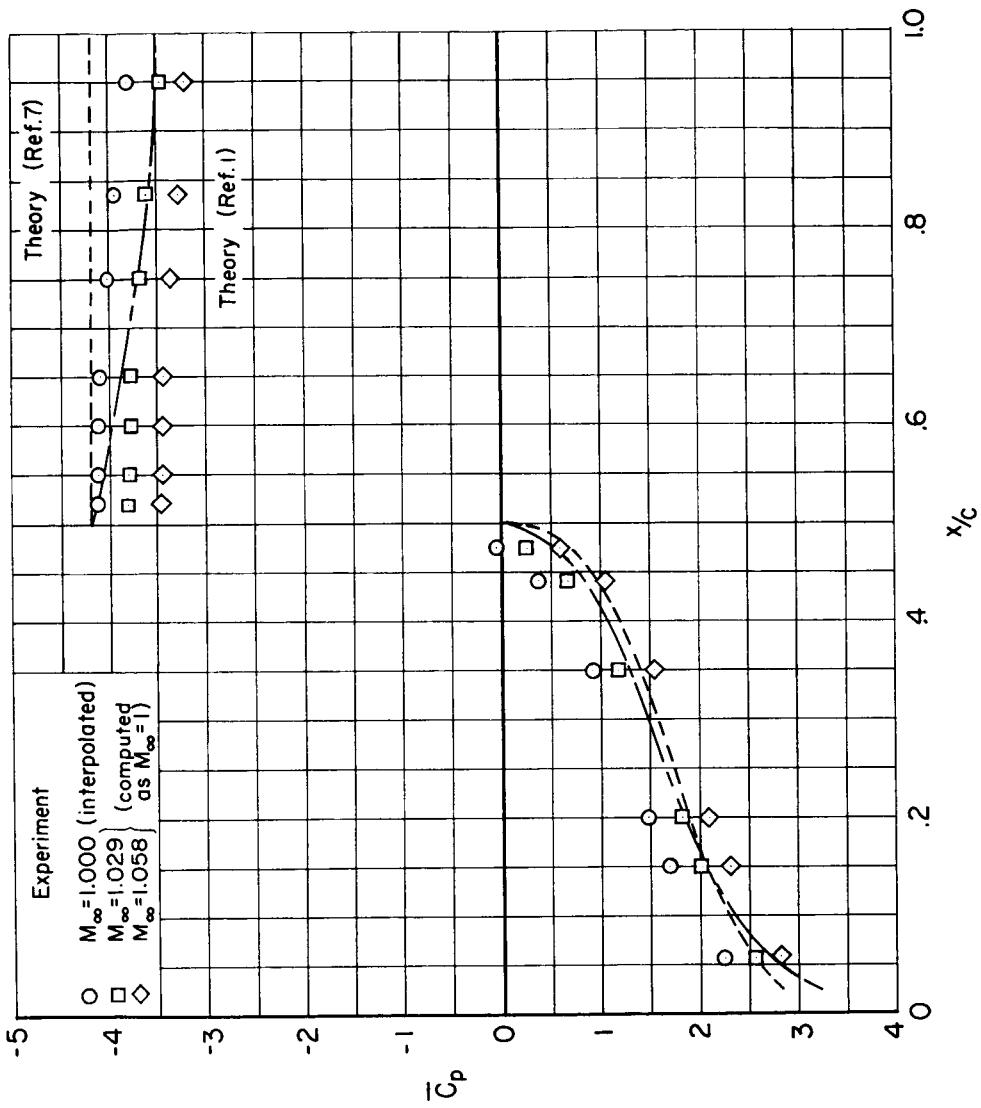


Figure 19.— Variation with  $\xi_\infty$  of  $\bar{c}_{dp}$  for 2-l/2-inch single wedge at  $\alpha_0 = 0^\circ$ .



(a) Effect of free stream speed.

Figure 20.- Transonic similarity pressure distributions for double-wedge airfoil at  $\alpha_0 = 0^\circ$ .



(b) Effect of Mach number shifts.

Figure 20.- Concluded.

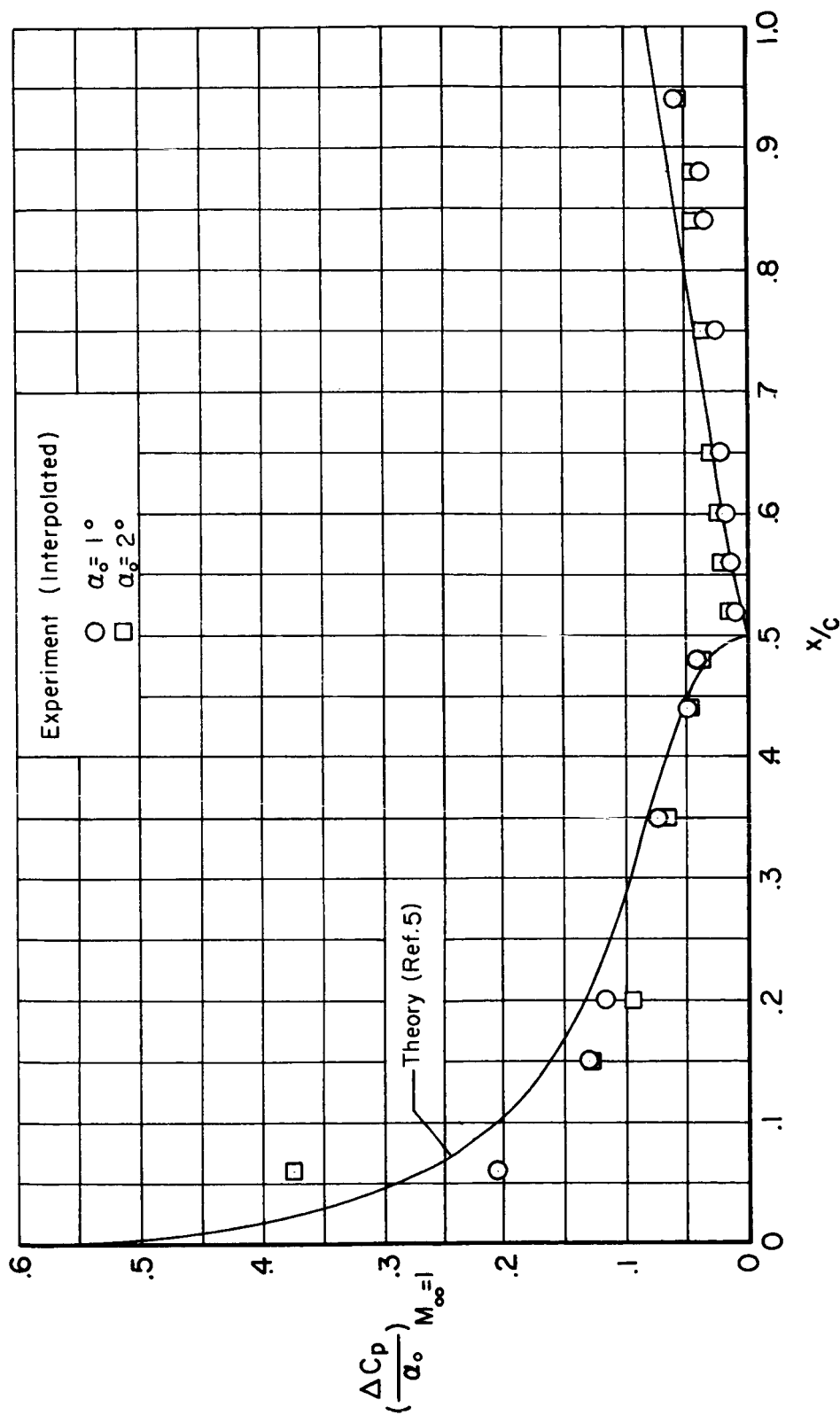


Figure 21.-- Variation of lift loading over the double-wedge airfoil at sonic speed.

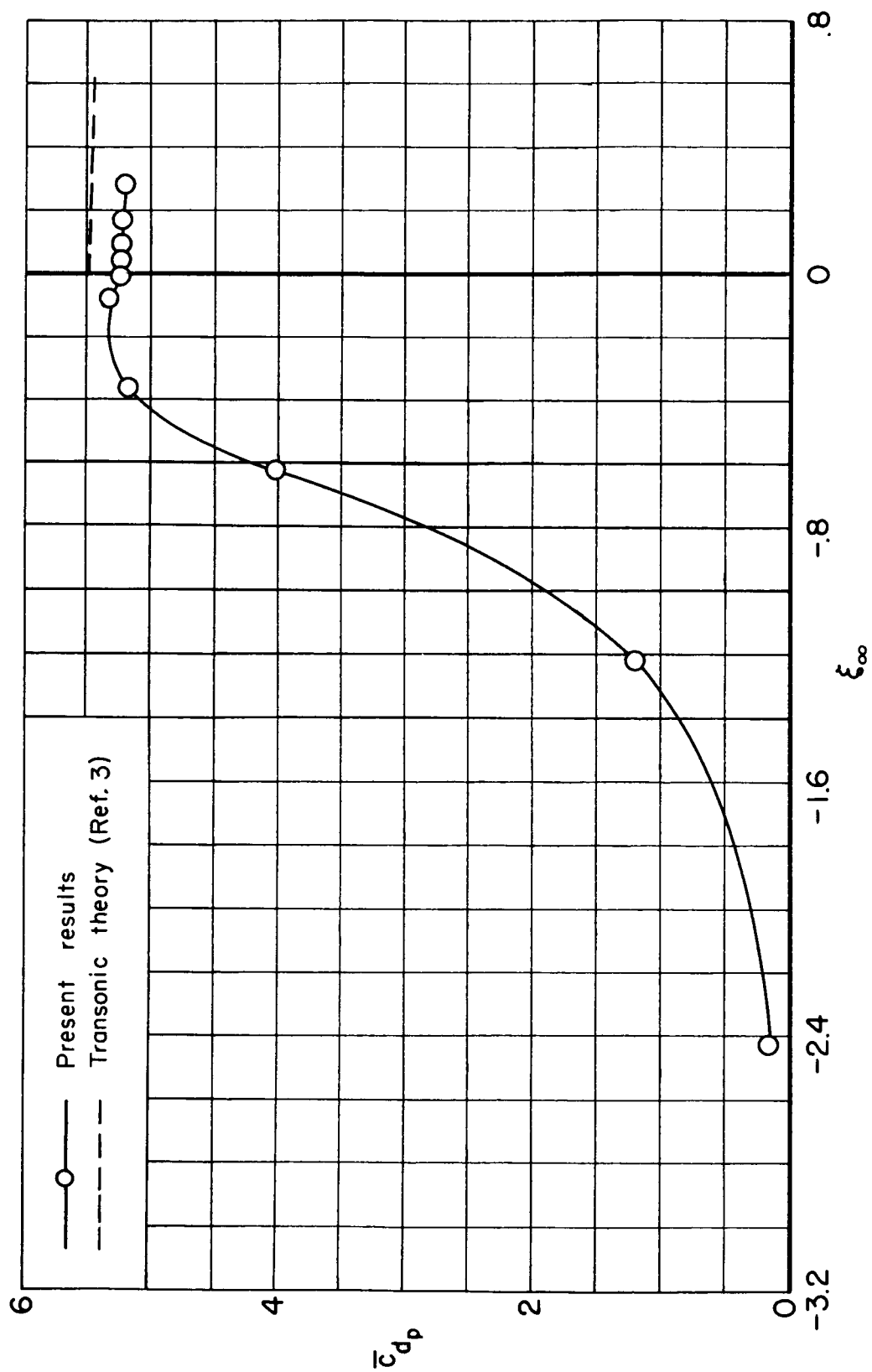
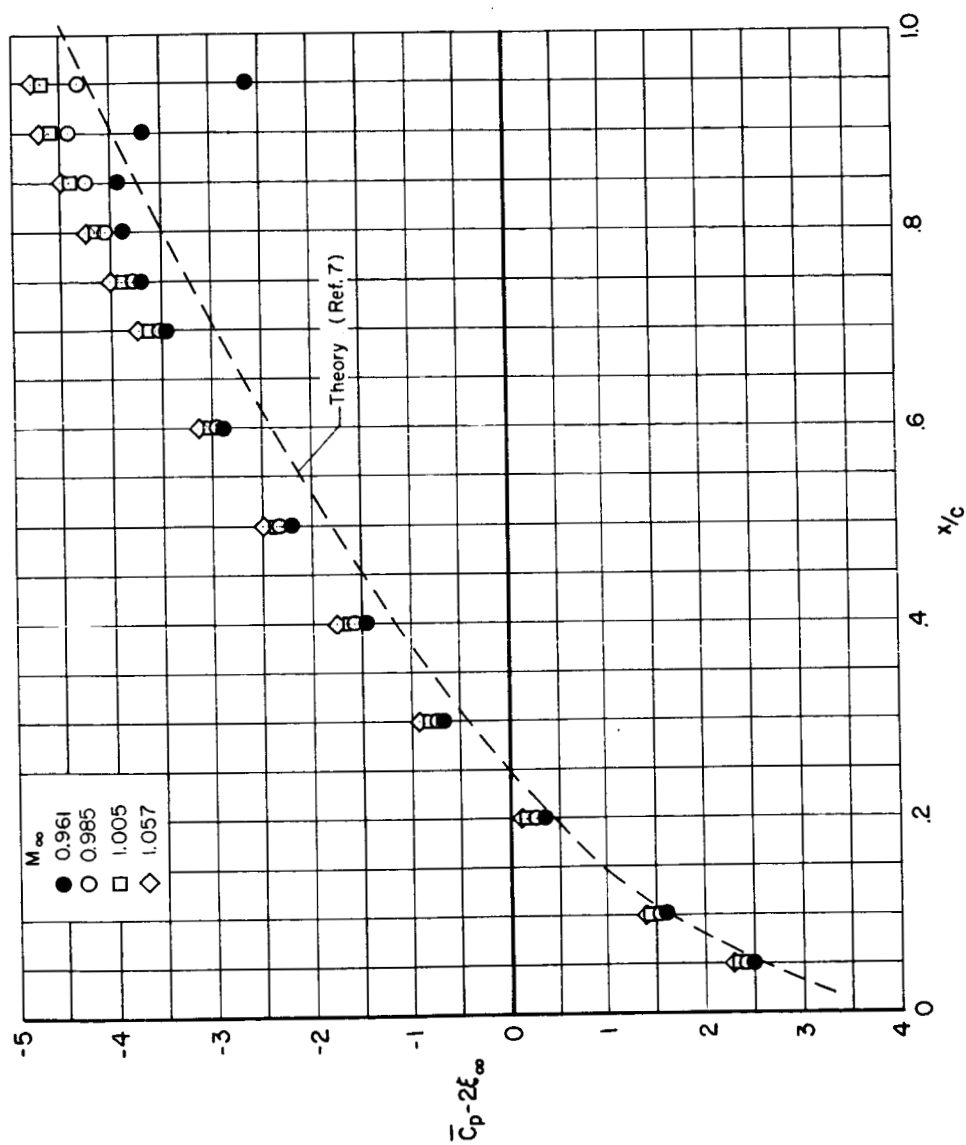
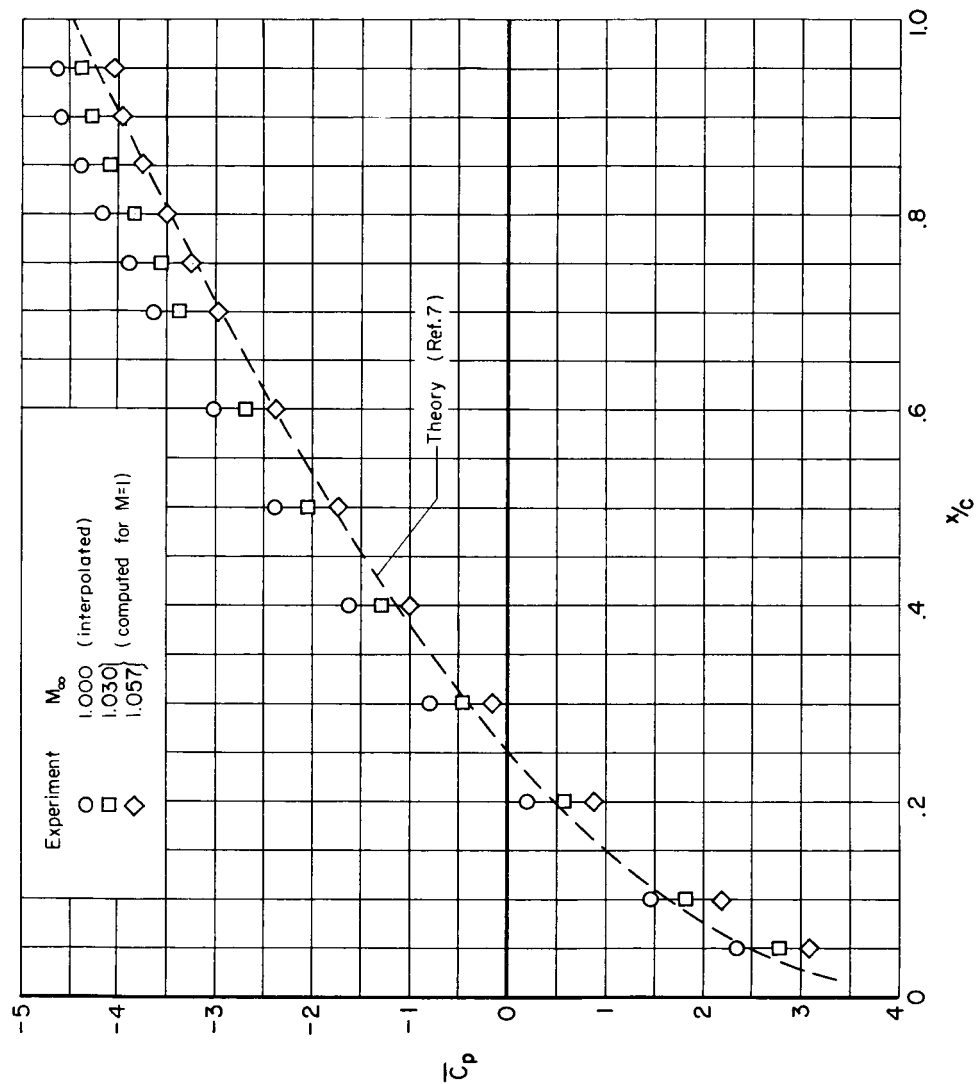


Figure 22.- Variation with  $\xi_\infty$  of  $\bar{c}_{dp}$  for double-wedge airfoil at  $\alpha_0 = 0^\circ$ .



(a) Effect of free stream near sonic speed.

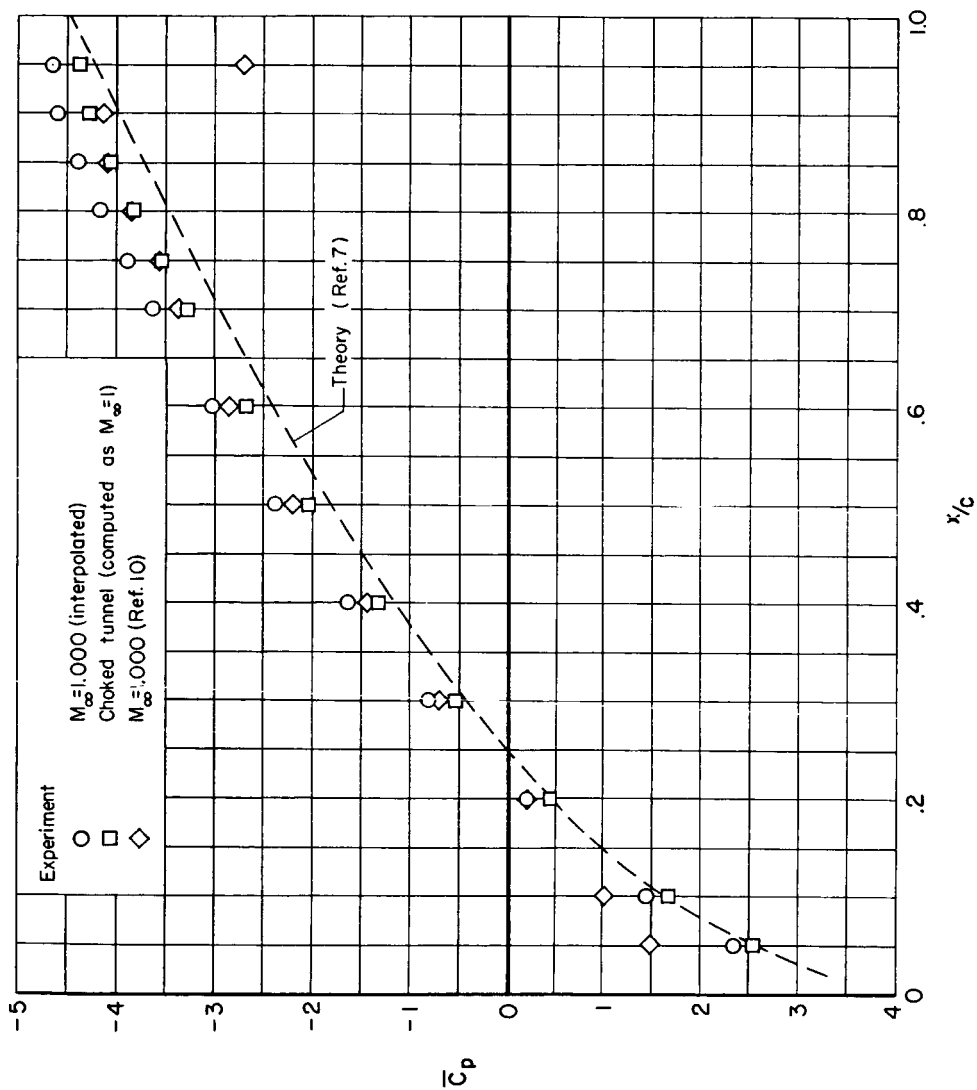
Figure 23.- Transonic similarity pressure distributions for circular-arc airfoil at  $\alpha_0 = 0^\circ$ .



(b) Effect of Mach number shifts.

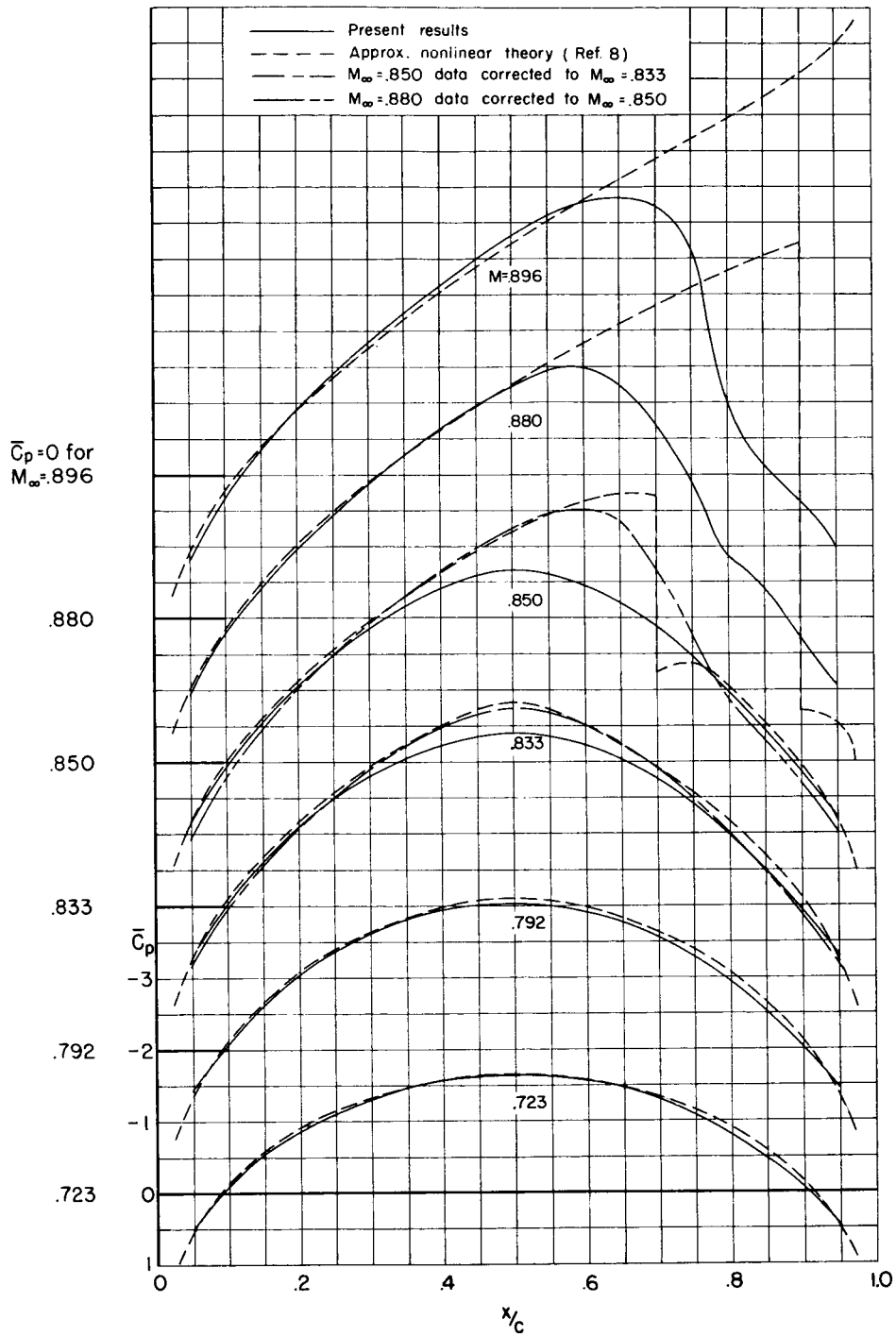
Figure 23.- Continued.





(c) Comparisons with other results at sonic conditions.

Figure 23.- Continued.



(d) Comparison with theory at subsonic speeds.

Figure 23.- Concluded.

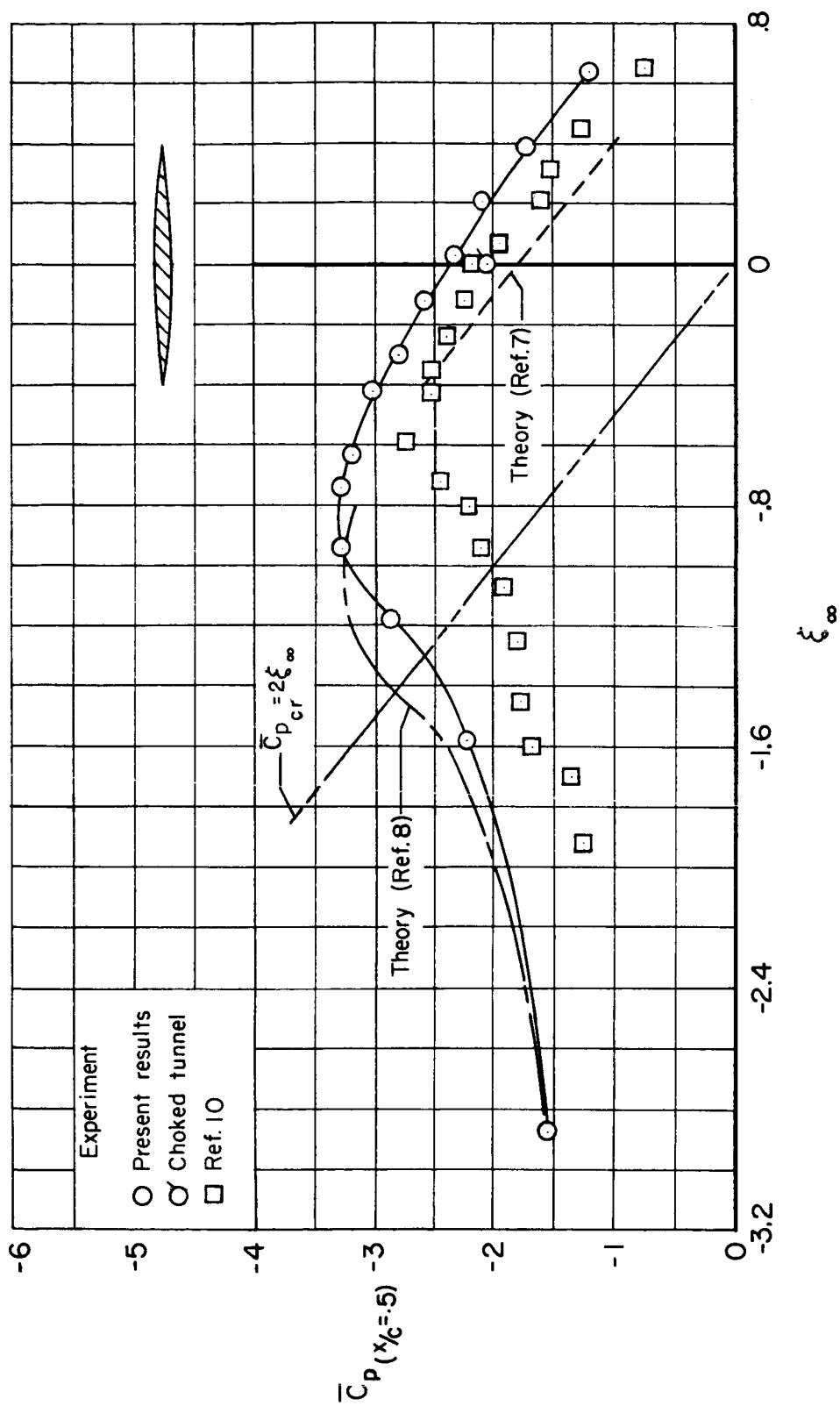


Figure 24.- Variation with  $\xi_\infty$  of  $\bar{C}_p$  at midchord of circular-arc airfoil at  $\alpha_0 = 0^\circ$ .

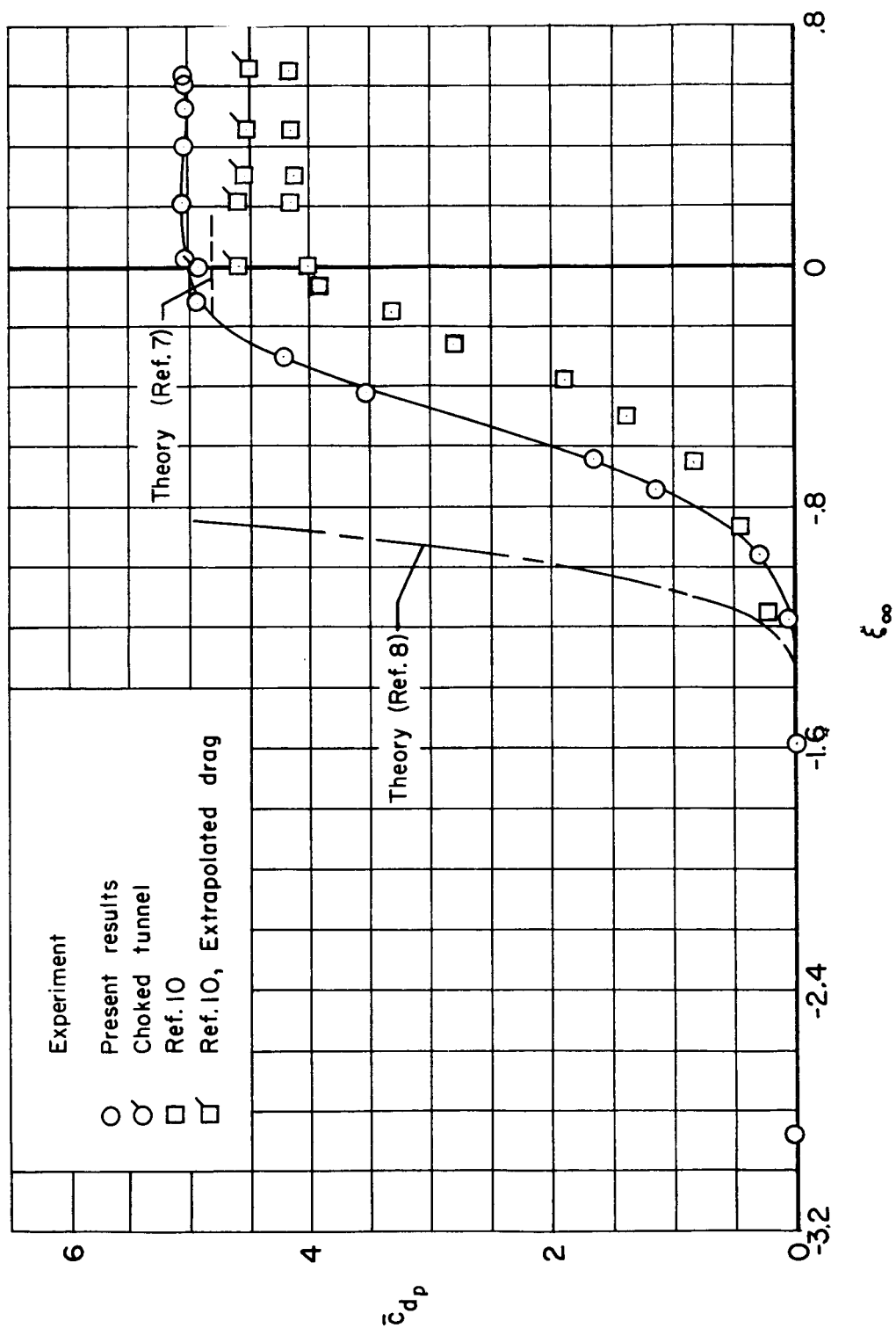


Figure 25.- Variation with  $\xi_\infty$  of  $\bar{c}_{d_p}$  for circular-arc airfoil at  $\alpha_0 = 0^\circ$ .